Andreas Ramsauer, BSc

Development of an Operation Strategy for a Hybrid Electric Vehicle incorporating Driveability Aspects and a Predictive Charging Strategy

Master's Thesis

to achieve the university degree of
Master of Science
Master's degree program: Mechanical Engineering

submitted to

Graz University of Technology

Faculty of Mechanical Engineering

Institute of Automotive Engineering
Member of [**FSI**]

Supervisors:
Dipl.-Ing. Dr.techn. Jürgen Fabian
Dipl.-Ing. Dr.techn. Harald Kraus

Graz, August 2016

Acknowledgements

Finishing a master thesis is a turning point in life. Herewith I would like to thank everybody who has supported and encouraged me and thus enabled this personal success.

Firstly, I would like to express my sincere gratitude to my supervisor Dr. Harald Kraus for the ongoing support, motivation and immense knowledge. His feedback and guidance was an enormous help during the whole period.

I would also like to thank Dr. Jürgen Fabian and Dipl.-Ing. Martin Ackerl for their assistance. I could always rely on their know-how in terms of troubleshooting and also the completion process of the thesis was supported by them.

Sincere thanks also goes to my family. Besides enabling my education they have helped me with unceasing support.

My time at university was enriched by my friends and fellow students who therefore should not be left unmentioned.

Statutory Declaration

I declare that I have authored this thesis independently, that I have not used other than the declared sources / resources, and that I have explicitly marked all material which has been quoted either literally or by content from the used sources.

....
(date) (signature)

Abstract

Hybrid electric vehicles (HEVs) captivate with low emissions, good fuel economy and a wide driving range which are the result of the combination of different power sources. In contrast, the coordination of these energy sources and converters and the power flow control for both the mechanical and the electrical path also imposes the major challenge for the development of HEVs. The potential of hybrid propulsion units therefore is highly influenced by the choice of the operation strategy. Whereas initially rule-based control algorithms found application, current research is being done towards optimization methods combined with adaptive and predictive control strategies.
As current research is mainly focusing on the energy management, hardly any predictive and adaptive operation strategies take driveability aspects into account. This leads to an unrealistic depiction of the fuel saving potential which cannot be achieved in a mass production vehicle. Therefore, the goal of this research project is to enhance the driveability of HEVs using the input of advanced prediction and adaptation algorithms. Serial and parallel-serial hybrid architectures allow the engine speed to be decoupled from the vehicle speed, making it possible to operate the engine with maximum fuel efficiency. This property can be regarded as a continuously variable transmission and is therefore called electro-mechanical CVT (eCVT). While the eCVT offers great fuel saving potential, it also needs to be considered that it disconnects the driver input (accelerator pedal) from the engine speed, resulting in an undesirable feeling of being disconnected with the powertrain.
This project aims to deliver a reconnected HEV performance by having the engine rpm be a function of accelerator pedal input and vehicle speed. Further, a driving type classifier allows to adjust the engine speed behavior according to the driver's needs, giving the vehicle a specific character while simultaneously ensuring that driving comfort, driving safety and driving pleasure are held at a very high level. The application of a predictive charging strategy based on a dynamic programming approach allows to anticipate the future power demand, assuring a highly intuitive vehicle behavior while preserving outstanding fuel efficiency.

Kurzfassung

Hybridfahrzeuge bestechen durch niedrige Emissionen, geringen Kraftstoffverbrauch und große Reichweite. Dies wird durch Kombination unterschiedlicher Energiespeicher und Energiequellen erreicht, was zugleich aber die größte Entwicklungsherausforderung darstellt. Das Potential hybrider Antriebskonzepte ist daher stark von der Betriebsstrategie abhängig. Während früher regelbasierte Strategien angewendet wurden, sind adaptive und prädiktive Ansätze in Kombination mit Optimierungsstrategien Gegenstand der aktuellen Forschung.
Da die derzeitige Entwicklung vorwiegend auf das Energiemanagement abzielt, wird in den meisten adaptiven und prädiktiven Strategien der Aspekt der Fahrbarkeit meist ausgeklammert. Dies führt zu einer unrealistischen Darstellung des Kraftstoffeinsparungspotentials, welche in Serienfahrzeugen nicht erreicht werden kann. Dieses Forschungsprojekt zielt daher darauf ab, die Fahrbarkeit von Hybridfahrzeugen mittels der Informationen adaptiver und prädiktiver Strategien zu verbessern.
Serielle und parallel-serielle Hybridfahrzeuge erlauben es, die Verbrennungskraftmaschine im verbrauchsoptimalen Punkt zu betreiben, da sie eine Entkoppelung zwischen Motordrehzahl und Fahrgeschwindigkeit ermöglichen. Diese Eigenschaft gleicht einem kontinuierlich variablen Getriebe (CVT) und wird daher als elektro-mechanisches CVT (eCVT) bezeichnet. Während dadurch großes Kraftstoffeinsparungspotential erzielt wird, muss berücksichtigt werden, dass es somit zu einer als störend empfundenen Abkoppelung des Fahrerwunsches (Fahrpedalstellung) von der Motordrehzahl kommt.
Diese Arbeit zielt darauf ab, den Fahrer wieder mit dem Antriebsstrang zu koppeln, indem die Motordrehzahl durch einen Funktionszusammenhang zwischen Fahrpedalstellung und Fahrzeuggeschwindigkeit festgelegt wird. Eine Fahrertypklassifizierung erlaubt es des Weiteren, das Drehzahlverhalten nach den Bedürfnissen des Fahrers einzustellen. Dadurch erhält das Fahrzeug einen spezifischen Charakter während Fahrkomfort, Fahrsicherheit und Fahrfreude auf höchstem Niveau gehalten werden. Die Anwendung einer auf der dynamischen Programmierung basierenden prädiktiven Ladestrategie erlaubt es, zukünftige Leistungsanforderungen vorauszuberechnen, was zu intuitivem Fahrverhalten und hervorragender Kraftstoffeffizienz führt.

Contents

Abbreviations

AC	Alternating Current
ANN	Artificial Neural Network
BMS	Battery Monitoring System
CCU	Component Controller Unit
CL	Clutch
COG	Center Of Gravity
DC	Direct Current
DFCO	Deceleration Fuel Cut-Off
DOF	Degree Of Freedom
DP	Dynamic Programming
DPM	Dynamic Programming Method
ECMS	Equivalent Consumption Minimization Strategy
ECU	Engine Control Unit
eCVT	electro-mechanical Continuous Variable Transmission
EG	Electric Generator
EMG	Electric Motor/Generator
EM	Electric Motor
ESS	Energy Storage System
EV	Electric Vehicle
FD	Final Drive
GBX	Gearbox
HCU	Hybrid Control Unit
HEV	Hybrid Electric Vehicle
ICE	Internal Combustion Engine
MPC	Model Predictive Control
ODE	Ordinary Differential Equations
OS	Operating Strategy
PCS	Predictive Charging Strategy
PID	Proportional Integral Differential
PGS	Planetary Gear System
PHEV	Plug-In Hybrid Electric Vehicle
PM	Particulate Matter
SOC	State Of Charge
TC	Transition Conditions
VDV	Vibration Dose Value

Symbols

Latin Symbols

a	Acceleration
$\hat{a}$	Acceleration in the frequency domain
a_0	Coefficient for the determination of the fuzzy output
a_1	Coefficient for TMsimple tire model
a_2	Coefficient for TMsimple tire model
a_i	Coefficient for the determination of the fuzzy output
a_k	Discretized acceleration
a_R	Rolling resistance coefficient
a_w	Frequency weighted acceleration
$\hat{a}_w$	Frequency weighted acceleration in the frequency domain
a_{wF}	Fast moving root mean square of the frequency weighted acceleration
a_{wS}	Slow moving root mean square of the frequency weighted acceleration
$a_{w\tau}$	Moving root mean square of the frequency weighted acceleration
$a_{w\mathcal{T}}$	Root mean square of the frequency weighted acceleration
a_{wv}	Value of the vibration in all three directions
a_{wx}	Frequency weighted acceleration x direction
a_{wy}	Frequency weighted acceleration y direction
a_{wz}	Frequency weighted acceleration z direction
A	Coefficient for TMsimple tire model
A_f	Front view surface
b	Neural network bias
b_1	Coefficient for TMsimple tire model
b_2	Coefficient for TMsimple tire model
$bsfc$	ICE brake specific fuel consumption
B	Coefficient for TMsimple tire model
c	Constraint of the optimal control problem
c_1	Coefficient for TMsimple tire model
c_2	Coefficient for TMsimple tire model
$c_{f/r,0}$	Initial value of the spring stiffness at the front or rear
$c_{f/r,Tire}$	Vertical tire stiffness front or rear

c_w	Air resistance coefficient
C	Capacitive effects of the charge accumulation-/separation occurring at the interface between the electrodes and electrolyte
C_v	Closed set
C_w	Closed set
d	Bound of the state variable
$d_{f/r,0}$	Damper coefficient for low velocities at the front or rear
dF_{x0}	Longitudinal tire stiffness
e	Bound of the control variable
f	Functional to be optimized
F	Functional that describes the alternation of the SOC χ for a specified timestamp
F_a	Translational acceleration force
F_d	Air resistance force
$F_{d,f/r}$	Damper force front or rear
$F_{d,real}$	Damper force real vehicle
$F_{d,sim}$	Damper force simulation model
F_g	Climbing resistance force
F_k	Discretized functional F
F_r	Rolling resistance force
$F_{s,f/r}$	Spring force front or rear
F_t	Propulsion force acting on the tire
F_x	Longitudinal tire force
$F_{x,CL}$	Axial CL force
$F_{x,f/r}$	Transferable tire force at the front or rear wheels
$F_{x,inf}$	Saturation value of the longitudinal tire force
$F_{x,max}$	Maximum longitudinal tire force
F_z	Vertical tire load
$F_{z,f/r}$	Resulting axle load
$F^0_{z,f/r}$	Static proportion of the axle load
$F^d_{z,f/r}$	Dynamic proportion of the axle load
$F_{z,f/r,Tire}$	Vertical tire force
$F^0_{z,f/r,Tire}$	Static proportion of the tire force
$F^d_{z,f/r,Tire}$	Dynamic proportion of the tire force
$F_{z,nom}$	Nominal vertical load
g	Gravity constant
g_N	Assessment of the final state of the optimal control problem
G	Weighting term of the final state
G_d	Transfer function dead-time element
G_l	Transfer function first-order lag element
h_{COG}	COG height
h_k	Assessment of the final state of the optimal control problem
H	Infinitesimal cost functional

H_u	Lower heating value of the fuel
i	Current state of the optimal control problem
$i_{1/2}$	GBX gear ratio
$i_{d,f/r}$	Spring damper conversion at the front or rear
i_{FD}	FD gear ratio
i_p	Neural network input
i_{SGR}	Summation gear ratio
I_{Bat}	Battery current
I_c	Constrained current
I_{EG}	EG current
I_{EM}	EM current
I_{EMG}	EMG current
I_{req}	Required EM current
$I_{lim,chg}$	Maximum battery charging current
$I_{lim,dchg}$	Maximum battery discharging current
J	Cost-to-go function
J_k	Discretized cost-to-go function
J_N	Cost for the final state
k	Current timestep of the optimal control problem
k_x	Correction factor x axis
k_y	Correction factor y axis
k_z	Correction factor z axis
K	Coefficient for TMsimple tire model
K_p	Proportional constant EG controller
l	Wheelbase
$l_{f/r}$	Horizontal distance between COG and front or rear axle
l_s	Horizontal distance between COG and seat
m	Vehicle mass
m_c	Chassis mass
$m_{f/r}$	Undamped mass front or rear
$\dot{m}_f$	ICE fuel consumption
n_w	Neural network weighting term
N_{plates}	Number of friction plates
N_χ	Grid resolution control variable
N_ζ	Grid resolution state variable
o	Neural network output
p_c	Degression at compression
p_{EG}	EG pedal position
p_{EM}	EM pedal position
p_p	Accelerator pedal position
p_r	Degression at rebound
P_{Bat}	Battery power
P_c	Constrained power

P_{el}	Electrical power
$P_{EG,el}$	Electrical power produced by the generator
P_{EM}	EM power
$P_{EM,el}$	Electrical EM power
P_{ICE}	ICE power
$P_{ICE,current}$	Current ICE power
$P_{ICE,proposed}$	Proposed ICE power
$P_{lim,chg}$	Maximum battery charging power
$P_{lim,dchg}$	Maximum battery discharging power
P_{mech}	Mechanical power
Q_{nom}	Nominal battery capacity
r_{dyn}	Dynamic tire radius
r_m	Mean friction radius
r_x	Rotation along the x axis
r_y	Rotation along the y axis
r_z	Rotation along the z axis
R_{ct}	Charge-transfer resistance
R_d	Diffusion resistance
R_i	Inner resistance of the battery
R_o	Ohmic resistance
s	s-domain
s^*	Longitudinal tire slip
SOC_0	Initial battery SOC
SOC_{min}	Minimum SOC
SOC_{max}	Maximum SOC
t	Time
t_f	Final timestamp of the optimal control problem
T	Torque
T_1	Torque resulting from the power constraint
T_2	Torque resulting from the current constraint
T_a	Required momentum for acceleration
$T_{acc,ICE}$	ICE acceleration torque
T_c	Allowed torque given by constraints
T_{CL}	CL torque
$T_{CL,in}$	CL input shaft torque
$T_{CL,out}$	CL output shaft torque
T_{EM}	Torque at the EM under consideration of the powertrain losses
$T_{EM,max}$	Maximum EM torque
$T_{EM,raw}$	Torque at the EM without powertrain losses
T_{EMG}	EMG torque
$T_{EMG,out}$	EMG torque at the output shaft
$T_{FD,in}$	FD input torque
$T_{FD,out,l/r}$	FD output torque

T_{ICE}	ICE torque
$T_{ICE,drag}$	ICE drag torque
$T_{ICE,max}$	ICE full load curve
$T_{ICE,out}$	ICE torque at the crankshaft
$T_{in,1/2}$	Torque at both GBX input shafts
T_{out}	Output torque of the GBX
T_T	Tire torque
T_f	Propulsion or brake torque at the front
T_r	Propulsion or brake torque at the rear
T_{recup}	Recuperation torque
T_{req}	Required torque at the EM
T_{res}	Necessary torque at the wheels to overcome the resistance forces
$T_{res,EM}$	EM resistance torque
$T_{res,ICE}$	ICE resistance torque
$T_{T,f}$	Tire torque acting at the front
$T_{T,r}$	Tire torque acting at the rear
u	Power-split value between ICE and EMG
U_{Bat}	Battery voltage
U_{OC}	Open circuit voltage
U_{RC}	Voltage drop in the RC-branch
v	Vehicle speed
v_c	Predefined driving cycle speed
v_k	Discretized vehicle speed
v_x	Vehicle speed in x direction
v_s	Slip velocity
w	Frequency (time domain)
$\bar{w}$	Frequency (frequency domain)
W	Frequency weighting function
W_c	Frequency weighting function for the assessment of well-being in seated position with vibration transferred via the seat back along the x axis
W_d	Frequency weighting function for the horizontal axes x and y
W_e	Frequency weighting function for rotational vibrations about three axes x, y and z, for the seated position and for the assessment of well-being
W_f	Frequency weighting function for the assessment of low-frequency vertical vibrations possibly resulting in kinetosis
W_j	Frequency weighting function for vibration measurements beneath the head of the individual in a recumbent position, for assessment of the well-being in the case of vertical vibrations
W_k	Frequency weighting function for the vertical axis z
W_m	Frequency weighting function for the assessment of the well-being with undefined body posture

x	Longitudinal direction
x_i	Fuzzy input variable
y	Lateral direction
y_F	Fuzzy output variable
z	Vertical direction
z_1	Main CL dynamics
z_2	Relative CL dynamics
z_{am}	Starting point of the progressive spring characteristic for negative z_c
z_{ap}	Starting point of the progressive spring characteristic for positive z_c
z_c	Chassis translation in vertical direction
z_{dm}	Point for which the spring constant equals twice the intial value for negative $\dot{z}_{f/r,c}$
z_{dp}	Point for which the spring constant equals twice the intial value for positive $\dot{z}_{f/r,c}$
$z_{f/r,c}$	Chassis movement at the position of the spring/damper fixing point
$\dot{z}_{f/r,c}$	Chassis velocity at the position of the spring/damper fixing point

Greek Symbols

β	Inclination angle
δ_c	Driving cycle distance
δ_m	Distance computed in the model
$\Delta\delta$	Model accuracy measure
Δt	Time step
$\Delta z_{f/r}$	Difference between the movement of the undamped masses at the front or rear and the chassis
$\Delta\dot{z}_{f/r}$	Difference between the velocity of the undamped masses at the front or rear and the chassis
$\Delta\zeta$	Alternation of the state variable ζ in the current timestep
$\Delta\omega_{CL}$	CL slip
$\Delta\omega_{ICE}$	Difference between actual engine speed and target engine speed
ζ	Control variable of the optimal control problem
ζ_k	Discretized control variable of the optimal control problem
$\eta_{c,d}$	Charging or discharging efficiency
η_{EM}	EM efficiency
η_{EMG}	EMG efficiency
η_{FD}	FD efficiency
η_{ICE}	ICE efficiency
η_{SGR}	Summation gear efficiency

ϑ_{Bat}	Battery temperature
Θ	Inertia
$\Theta_{CL,in}$	CL input shaft inertia
$\Theta_{CL,out}$	CL output shaft inertia
$\Theta_{CL,\Pi}$	Product of CL input and output shaft inertia
$\Theta_{CL,\Sigma}$	Sum of CL input and output shaft inertia
Θ_{EMG}	EMG rotor inertia
Θ_{ICE}	ICE inertia
$\Theta_{in,1/2}$	Inertia of the GBX input shafts
Θ_{out}	Inertia of the GBX output shaft
Θ_T	Tire inertia
μ	Friction coefficient
μ_0	Static friction coefficient
μ_{sl}	Sliding friction coefficient
ξ	Integration variable when calculating $a_{w\mathcal{T}}$; equal to time t
$\mathcal{O}$	State of the optimal control problem
π	Amount of CO_2 generated in the complete combustion process
Π	State of the optimal control problem
ρ	Amount of H_2O generated in the complete combustion process
ρ_A	Air density
$\mathcal{P}$	State of the optimal control problem
σ	Coefficient for the determination of the oxygen amount needed for complete combustion
τ	Moving average time constant
$\mathcal{T}$	Measurement duration
φ_c	Chassis rotation along y axis
Φ_a	Power spectral density
Φ_k	Penalty for infeasible combinations of χ^i and ζ_k
Φ_N	Penalty for infeasible regions of the final state
χ	State variable of the optimal control problem (SOC)
χ_0	Initial state (SOC)
χ_f	Final state (SOC)
χ_k	Discretized state variable of the optimal control problem
χ_k^i	Discretized state variable for a specific timestamp k and state i
χ_N^i	Discretized final state
ω_{CL}	CL angular velocity
$\omega_{CL,in}$	CL input shaft angular velocity
$\omega_{CL,out}$	CL output shaft angular velocity
ω_{EM}	EM angular velocity
ω_{EMG}	EMG angular velocity
$\omega_{FD,in}$	FD input shaft angular velocity
$\omega_{FD,out,l}$	FD left output shaft angular velocity
$\omega_{FD,out,r}$	FD right output shaft angular velocity

ω_{ICE}	ICE angular velocity
ω_{idle}	ICE idle speed
$\omega_{in,1/2}$	Angular velocity of the GBX input shafts
ω_{out}	Angular velocity of the GBX output shaft
ω_T	Tire angular velocity
ω_{tow}	Angular velocity at which the ICE starts to produce torque when tow starting
$\dot{\omega}$	Angular acceleration
$\dot{\omega}_{CL,in}$	CL input shaft angular velocity
$\dot{\omega}_{CL,out}$	CL output shaft angular velocity
$\dot{\omega}_{ICE}$	ICE angular acceleration
$\dot{\omega}_{out}$	Angular acceleration of the GBX output shaft
$\dot{\omega}_T$	Tire angular acceleration

Vectors

$\mathbf{d}$	Coefficient vector
$\boldsymbol{\omega}$	CL angular velocity vector
$\dot{\boldsymbol{\omega}}$	CL angular acceleration vector
$\mathbf{z}$	Generalised speed vector

Matrices

$\mathbf{K}$	Transformation matrix
$\mathbf{M}$	CL mass matrix

1 Introduction

1.1 Motivation

Ongoing energy conservation concerns have led to numerous discussions on the optimal propulsion technology for future ground vehicles. Since fossil fuels are a non-renewable resource, the conventional internal combustion engine layout for vehicle propulsion needs to be adapted. This can either be done by turning away from conventional fuels or by combination of the internal combustion engine with an electric propulsion system, which can be summarized under the catchphrase "hybridization". Another approach is to completely leave internal combustion engines behind and to focus on hydrogen powered fuel cells or full electric vehicles. Whereas these approaches face the challenge of effective production and storage methods, hybrid electric vehicles have gained the highest market share for alternative powertrains (compare Figure 1.1) as they offer the advantages of a wide driving range and high flexibility [26], [44].
The use of different propulsion units also results in an additional degree of freedom (DOF) for the torque supply which needs to be addressed in the operating strategy (OS). In Figure 1.2 the control problem is presented. The energy management controller determines the optimal power distribution of both propulsion units by using intelligent prediction and adaptation algorithms. Whereas the resulting power distribution is optimal regarding fuel consumption, it does not comprise any driveability aspects. To achieve the desired driving characteristics, the driveability controller alters the input of the energy management controller. The component controller units (CCUs) assure that the drivetrain components operate within their mechanical, thermal or electrical limits, and control the powertrain actuators.

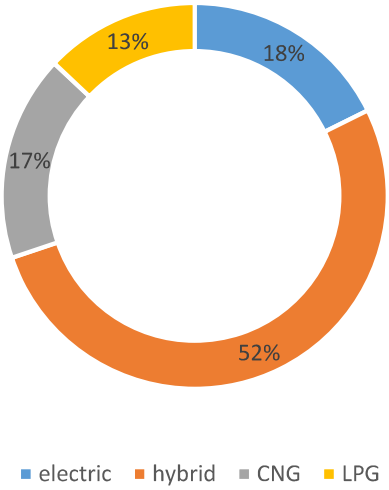

Figure 1.1: Market share for newly registered alternative powertrains in Germany 2014 [44]

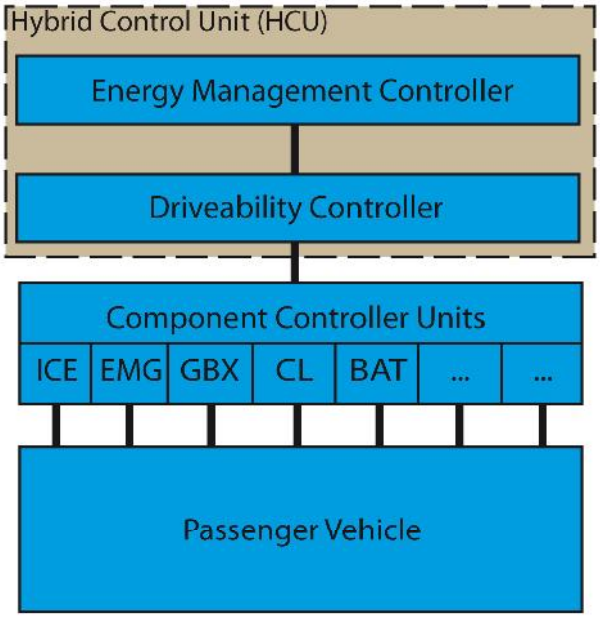

Figure 1.2: Vehicle controller levels, compare [32]

1.2 Objectives

The first objective of this project was to implement a dynamic combined HEV model into Matlab-Simulink with close to real vehicle behavior. To achieve this, extensive measurements of an existing vehicle have been performed. The needed parameters were then extracted by using sophisticated parameter identification algorithms.
Many studies have been done on the fuel saving potential of different predictive OS. Mostly, driveability is insufficiently considered. Therefore, this thesis aims to improve driveability while still enhancing the fuel saving potential compared to conventional HEVs. This is done by using crafty prediction and adaptation algorithms to simultaneously enhance fuel efficiency, driveability and vehicle performance, which is a unique aspect of this work.
In order to maximize fuel efficiency, an intelligent operation strategy using past and future driving information was developed as a replacement for the rule-based operating strategy implemented in the investigated HEV. This operation strategy is based on a dynamic programming method (DPM) in combination with a quasistatic vehicle model, and is real-time capable due to its smart execution. The fuel saving potential is significant and can be achieved while simultaneously enhancing driveability. As the used driving cycle has an impact on the performance of the OS, all algorithms are developed and tested with real-world driving cycles. This clearly underlines the request of providing real-driving fuel saving potential.
To improve driveability, the aforementioned eCVT behavior is cancelled by the HCU leading to a reconnection of the driver with the drivetrain. Moreover, the implemented operation strategy adapts to different driving styles by tailoring the vehicle's characteristics according to the driver's needs, which improves customer acceptance. For example, sporty drivers will be supported by sportive driving characteristics such as improved vehicle response. Further, the developed operation strategy is compatible with all parallel and power-split hybrid drivetrain topologies, and can therefore be implemented in a wide range of hybrid vehicles.
The hardware of the vehicles can be left unchanged, which contributes to the potential for application in the near future. The presented approach only affects the hybrid control unit consisting of the energy management controller and the driveability controller and is designed to be implemented in future mass production HEVs. Consequently, the additional costs are held at a minimum while increasing the customers' acceptance. Using prediction and adaptation algorithms for both the energy management controller and the driveability controller enhances driving pleasure and the fuel econonmy of HEVs. By designing the proposed controller to be used in early development, the effort required in adapting to prototypes and later mass-production vehicles is reduced. Consequently, the costs of implementation are diminished and even higher sophisticated hybrid technology can be offered at affordable prices.
Conclusively, the presented approach allows to improve the driving characteristics of hybrid electric vehicles while concurrently reducing fuel consumption without considerably increasing production costs.

2

State of the Art

2.1 Hybrid Electric Vehicles (HEVs)

Hybrid electric vehicles have always been considered as propulsion systems throughout history. Due to strict emission and fuel consumption regulations HEVs are becoming more and more popular nowadays. The word "hybrid" originates from the latin noun "hybrida" which can be translated as crossbreed. HEVs are defined by the UN as follows: *"A vehicle with at least two different energy converters and two different energy storage systems (on vehicle) for the purpose of vehicle propulsion"* [2].

Chemical, electrical or mechanical systems can be used as energy storage. Conventional chemical energy storage (petrol or diesel) in combination with electro-chemical (battery) or chemical energy storage systems have already proved their practicability, whereas pneumatic energy storage systems are only used in niche applications [26], [46].

According to a study by McKinsey (see [52]) the global market share of HEVs, plug-in electric vehicles (PHEVs) and electric vehicles (EV) is estimated to be about 33% by 2020. This can be explained by the advantages of hybrid propulsion systems listed in the following.

2.1.1 Advantages of Hybrid Electric Vehicles

Incorporating additional components in a vehicle's drivetrain leads to higher complexity and costs. Therefore, this effort needs to be compensated with an increase in the product value. For HEVs the resulting benefits can be summarised as follows (compare [46]):

Reduction of CO_2 emissions: The greenhouse gas CO_2 is a product of complete combustion of fossil fuels such as petrol or diesel and is suspected to have impact on global warming. Legislative regulations therefore aim to achieve an average emission of 95g/km by 2020. Whereas a conventional internal combustion engine (ICE) drivetrain layout leads to a highly fluctuating power demand at the ICE, HEV drivetrain layouts reduce the power fluctuations at the ICE by absorbing them with the electrical energy storage system.

Enhanced vehicle dynamics and driving pleasure: The responsiveness of the vehicle can be improved by adding the power provided by the secondary energy storage to the power delivery of the primary propulsion system.

HEVs can be regarded the bridge technology to electric and fuel cell vehicles: HEVs allow a slower electrification process of the drivetrain which is easier to handle than an abrupt switch to fully electric vehicles.

Possibility of pure electric driving: If the drivetrain layout allows the ICE to be decoupled from the drivetrain, the vehicle can be propelled fully electrically for low speeds. Further, start-stop functions can be implemented.

Brake energy recuperation: Conventional drivetrain layouts convert kinetic energy into thermal energy during a braking manoeuvre, whereas a HEV layout allows to transfer the kinetic energy to the battery via a generator.

The aforementioned benefits, legal regulations, customer demands and OEM strategies are the biggest motivation for turning away from conventional propulsion systems, but also other influence factors need to be considered when designing a specific drivetrain layout (compare [26]):

- Costs
- Competitiveness
- Image enhancement
- Innovation scope
- Strategic factors
- Market analysis
- Well to wheel emissions

2.1.2 Operation Modes of HEVs

HEVs allow the combination of different systems for propulsion, which results in a greater variety of operation modes respect to conventional drivetrain layouts. Depending on the HEV architecture, not all of the modes listed in the following adaption of [26] can be used in practice.

Start-stop: The ICE is turned of at standstill. This reduces fuel consumption in comparison to idling.

Coasting: As well as start-stop coasting is not specific for HEVs. The term describes the deceleration of the vehicle without providing propulsion torque. The ICE is disengaged from the drivetrain as it would produce drag losses otherwise. When coasting with engaged clutch, the ICE is put in DFCO (deceleration fuel cut-off) mode.

Recuperation: The electric traction motor is operated in generator mode which produces a braking torque used for the deceleration of the vehicle. This allows to transform the kinetic energy of the vehicle into electrical power which is then forwarded to the battery.

Torque supply: Due to the presence of different propulsion units, the torque to propel the vehicle can either be provided by the electric motor/generator (EMG), the ICE or both units.

- **Pure electric drive:** The vehicle is only propelled by the EMG. The clutch is disengaged and the ICE is shut off. Locally, emission free driving is possible.
- **Boosting:** The HEV is propelled by the EMG and the ICE. In this mode, the maximum power of both propulsion units allows dynamic driving performance.
- **ICE only:** The traction power provided in the same way as for conventional vehicle layouts. This operating mode also occurs with discharged battery.
- **Load point shifting:** The ICE is operated at a higher load point than necessary for providing the demanded power which results in better efficiency. The excessive power is transferred to the EMG where it is converted into electrical energy and then stored in the battery.

2.1.3 Hybrid Drivetrain Structures

This section illustrates the bacis drivetrain layouts of hybrid electric vehicles and their properties (compare [26], [46]). As a result of ongoing research in this area, more sophisticated drivetrain layouts have been developed which can be summarized as *Combined Hybrid Drivetrain Structures*. For further information see [46].

2.1.3.1 Serial Hybrid

For serial hybrid layouts the ICE delivers the power to a electric motor/generator (EMG_I), which converts the mechanical energy into electrical energy. After the conversion from alternating current (AC) to direct current (DC), the energy is stored in the battery (BAT). The traction power is delivered by the EMG_{II} and forwarded to the wheels by gearbox (GBX) and final drive (FD), meaning that for this layout the ICE is disconnected from the drivetrain. The pros and cons of this drivetrain layout are shown in Table 2.1 and Figure 2.1 depicts the serial HEV architecture.

Table 2.1: Advantages and disadvantages of serial HEVs

Advantages	Disadvantages
ICE operates at best efficiency	Decoupled engine speed behavior
No emission increasing dynamic loads for the ICE	Multiple energy conversion
Full electric drive possible	Necessity of 3 energy converters leads to high weight
Wheel hub drive possible	

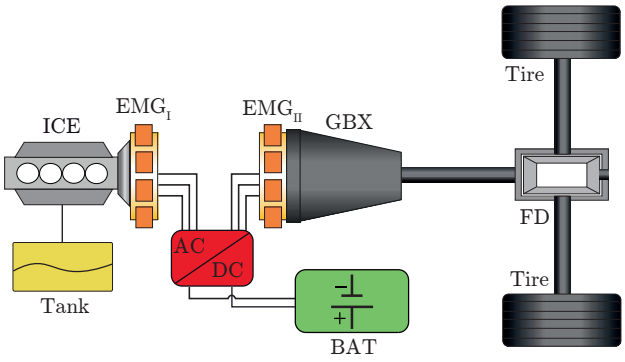

Figure 2.1: Serial HEV layout [32]

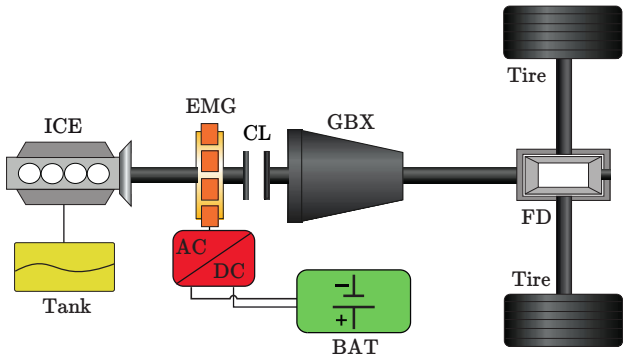

Figure 2.2: Parallel HEV layout [32]

2.1.3.2 Parallel Hybrid

By engaging the clutch (CL), parallel hybrid drivetrain layouts allow a coupling of the ICE with the wheels, to which the electrical path can be connected independently. This allows the vehicle to be propelled by the ICE, the EM or both units, compare Table 2.2 and Figure 2.2.

Table 2.2: Advantages and disadvantages of parallel HEVs

Advantages	Disadvantages
Only 1 EM necessary	Coupling of ICE to the wheels reduces ICE efficiency
Easy integration into conventional drivetrain layout	
Load point shifting possible	
ICE power is delivered directly to the wheels without energy conversion	

2.1.3.3 Power-split Hybrid

Power-split HEVs divide the mechanical power provided by the ICE into an electrical and a mechanical path. The power-split property (which is mostly realized with a planetary gear system (PGS)) can also be regarded as a transmission and is therefore referred to as eCVT. The drivetrain layout of power-split HEVs is depicted in Figure 2.3, whereas the pros and cons are stated in Table 2.3. Figure 2.3 shows, that the electrical path is realized by the coupled generator whereas the mechanical path is established by the PGS connecting the ICE directly to the driveshaft. As the mechanical efficiency is higher than

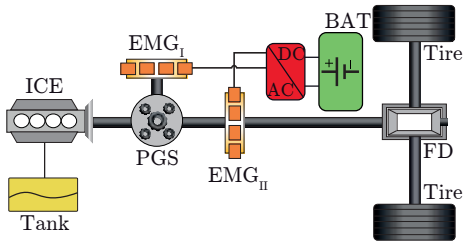

Figure 2.3: Power-Split HEV layout [32]

the electrical, the electrical HEV components should be designed to achieve maximum efficiency. This can also be realized by reducing the electrical power flow. A reduction of the electrical power also results in smaller electrical components which is useful for this drivetrain layout as it makes 2 EMGs necessary.
A special form of the power-split drivetrain layout establishes the mechanical path by using a clutch instead of the planetary gear system. This topology is then referred to as *combined power-split* HEV [26].

Table 2.3: Advantages and disadvantages of power-split HEVs

Advantages	**Disadvantages**
Every HEV operation mode possible	High complexity
Shifting without interruption of traction	Elaborated software needed for component coordination
Load point shifting possible	High weight
ICE power is delivered directly to the wheels without energy conversion	Transmission needed for power-splitting
	2 EMs needed

2.2 Operating Strategy (OS)

2.2.1 Purpose

Whereas conventional drivetrain layouts only comprise the ICE as energy source, hybrid electric vehicles offer an additional degree of freedom due to two propulsion systems. The task of the operating strategy is to coordinate these power sources in order to fulfil the driver's demand and to ensure that all drivetrain components operate within their mechanical, thermal and electrical limits. The OS has an immense impact on the marketability of HEVs as it controls fuel efficiency which is the main reason for the introduction of HEVs [34]. Previously rule-based OS found application, whereas nowadays the trend is going towards adaptive and predictive operating strategies. A detailed classification of operating strategies can be found in the following section.

2.2.2 Classification

2.2.2.1 Heuristic (Rule-based) OS

Heuristic control strategies are based on rules defined by different vehicle variables. Most commonly, the torque demand and the vehicle speed are used for the derivation of rules [19], compare Figure 2.4. In this example, the vehicle velocity v and the torque demand T are used for the calculation of the power-split value u between ICE and EMG. The key control parameters in this OS type are the thresholds defining the transitions between the different states. Besides torque thresholds also acceleration or power thresholds and combinations can be used. Power based formulations have the advantage of the correlation with the components' power limits which can be useful when designing the OS [19].

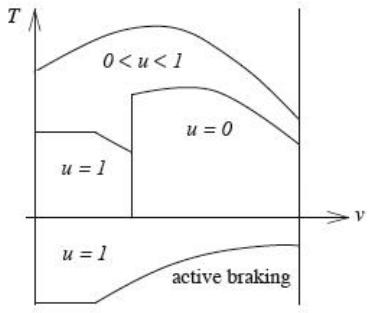

Figure 2.4: Heuristic OS using the vehicle speed v and torque demand T for the determination of the power-split value u between ICE and EMG [19]

Heuristic controllers are easy to implement and rather intuitive but their utility is strongly dependent on the choice of the threshold values. As the thresholds differ de-

pending on the driving conditions, a high tuning effort is required to achieve robustness which motivates the optimization model based controllers described in the following [19].

2.2.2.2 Optimal and Suboptimal OS

Optimal and suboptimal approaches are model based strategies which aim to minimize a cost functional. A typical cost functional is the fuel consumption m_f, whereas also other influences such as emissions can be considered in the cost functional [19]. This type of OS was derived from so-called model predictive control (MPC) approaches which try to predict the future system behavior and deducting optimal control variables with the help of a model of the investigated system [6].
Depending on the length of the prediction horizon, optimization based strategies can be divided according to *local* and *global* optimization strategies.

Local Optimization
These strategies relinquish global optimization and therefore deliver suboptimal results. Nevertheless, reducing the size of the problem to be optimized also decreases computation time which comes useful in real time control applications [11], [12].
Special local optimization algorithms compare the energy consumption of the ICE and the EM. This is done by converting the electrical energy consumed by the electric motor into an equivalent fuel consumption. These strategies allow a unified representation of the fuel consumption and the energy used by the battery and are therefore called *equivalent consumption minimization strategies* (ECMS) [42].
Charge sustaining strategies (which can be found in autarcik HEVs) require the SOC of the battery to be the same at the beginning and at the end of a trip. This request can be regarded as the boundary condition for each prediction horizon and therefore defines the local control problem. As the battery is not fully exhausted at the end of the journey, the fuel saving potential is not fully exploited which is especially compromising for PHEVs. Therefore, efforts were made to estimate the power demand along the entire journey and perform global optimization to calculate the boundary values for the local problem [45], [64].

Global Optimization
Global approaches consider the entire remaining journey in the cost functional. This allows to fully exhaust the fuel saving potential but also increases computation time. The main influence on the accuracy and on the computational effort is given by the future velocity profile which determines the power demand. In [27] an effort was made to determine the influence of the length of the prediction horizon on the global fuel saving potential. It was assumed, that within the prediction horizon the velocity profile is exactly known whereas outside the velocity is equal to the legislative speed limits.

2.3 Driveability

2.3.1 Definition

The assessment of driveability began with the introduction of the automobile itself. Whereas initially only a handling assessment was performed for different driving situations, the increasing velocity and traffic density made it inevitable to assess the vehicle behavior under consideration of the interaction between driver, vehicle and environment. Improved vehicle handling not only helps in terms of accident prevention, it also increases a vehicle's marketability [7], [51].
Throughout history the term "driveability" has been given different meanings. Often driveability is used in context with driving comfort which is defined as the absence of discomfort and distracting influences according to [4]. This implies a subjective evaluation as every driver experiences comfort in a different way. [38] states that driveability is an objective evaluation process with the help of characteristic parameters such as chassis acceleration and response time. In this thesis the term "driveability" will be referred to as the driver's subjective perception of the interactions between vehicle and driver which can be assessed subjectively or by using objective evaluation criteria based on correlation methods [51].

2.3.2 Subjective Evaluation

In the past, driveability was evaluated subjectively by test drivers and form sheets. These assessments lack of repeatability and reproducibility and are time and cost intensive. In [37] it is stated that subjective driving comfort is influenced by all senses: hearing, sight, chemical senses (smell, taste), somatic system (touch, body position) and vestibular system (balance). The scope of comfort criteria is defined by [51] according to Figure 2.5. It depicts a comfort assessment for 3 different vehicle models based on a rating from 0-10 for the different criteria. It can be seen that depending on the comfort criteria, model 3 may outcome the other 2 opponents in terms of handling, whereas it only scores the lowest points in terms of vibration, for example. Figure 2.6 shows the main influence factors for driving comfort and driveability for gear shifting according to [33]. Acceleration shows the highest influence, which correlates with the use of acceleration metrics for objective driveability evaluation. Acoustics are also important as they provide feedback to the driver. Subjective assessments can either be done using *direct* or *indirect* methods which are both influenced by the evaluator.

Direct methods: Here the evaluator describes the perceptions of the investigated phenomenon and an assessment is performed with the help of an evaluation scale. The main disadvantage of this approach lies in the necessity of the conversion of the subjective perception into a corresponding scale value [4]. Figure 2.7 depicts a ten-tier rating scale used for evaluating NVH-phenomena. It can be seen that the perception threshold varies for different costumer types which is attributable to the fact that different costumer types

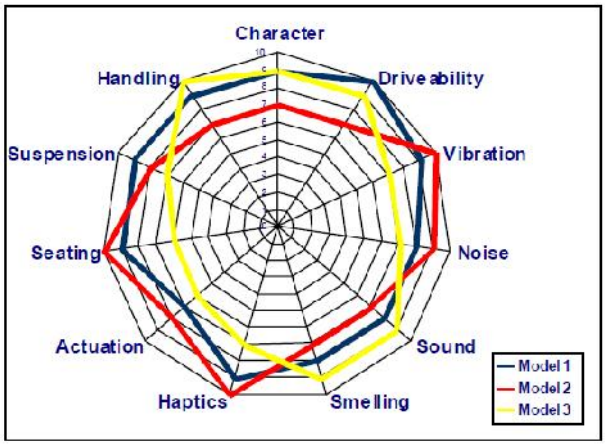

Figure 2.5: Comfort criteria [51]

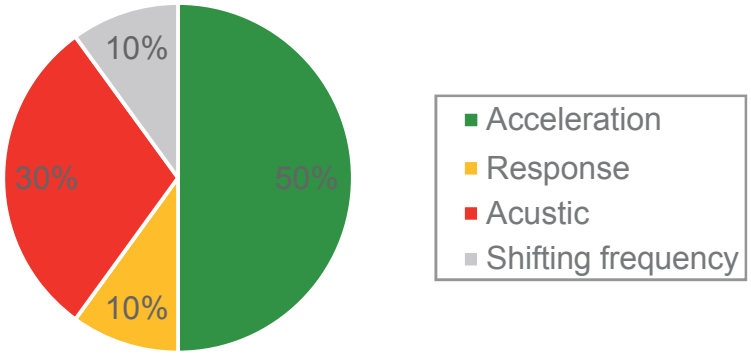

Figure 2.6: Main influence factors of driving comfort for gear shifting [33]

have difficulties in differentiating certain phenomena [4]. Further, it needs to be stated that the depicted scale undergoes slight variations to comply with the brand's marketing strategies.

Indirect methods: These assessment procedures try to capture changes of the evaluator caused by the disturbances correlating with the investigated effect. By having the evaluator perform extra tasks (e.g. calculations) the influence on the well-being caused by the absence of comfort is evaluated. These methods have the advantage of being resistant in terms of manipulation, but require high effort and impose a distraction on the evaluator [4].

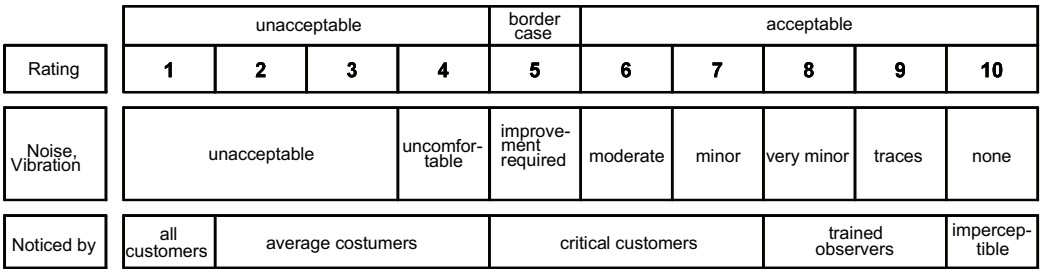

Figure 2.7: Ten-tier rating scale according to [3]

2.3.3 Objective Evaluation

Due to the rapid development of mobile measurement technology, huge efforts were made to incorporate measurement data into the subjective evaluation process in order to obtain objective criteria. With the use of correlation criteria, it becomes possible to predict manifestations of different subjective criteria by investigating measurement data. The prediction accuracy improves for higher correlation between the comfort assessment and the objective variable. Objectivization can be performed using multiple linear regression or artificial neural networks (ANNs). Whereas regression methods have the advantage of being established, ANNs captivate with the nonnecessity of a mathematical model [4]. Before performing objectivization, objective measures for the description of the system behavior have to be defined which will be performed in the following.

The exposure of the human body to vibration can be categorized according to the effect on the health (safety at work) and on the well-being (riding comfort). Thresholds for the human sensation of vibration depend on the vibration mode, the transmitting point and the direction of oscillation and can be found in the VDI 2057 standards [59]. The assessment of oscillations is performed in the frequency domain as their interaction with the human body is frequency dependent. This dependency can be expressed by performing a frequency weighting of the physical data measured at the entry point of the vibration exposure into the human body. The most common frequency weighting functions (W_k, W_d, W_f, W_m, W_c, W_e and W_j) are given in Figure 2.8 and Figure 2.9. The frequency weighting plays an important part in terms of objective evaluation as the human body shows a different perception of vibration depending on the frequency region. Vibrations in the domain of the human body's eigenfrequencies are perceived as extremely disturbing which needs to be considered in the frequency weighting functions. The eigenfrequency of the stomach for example, lies in the domain of approximately 5 Hz [14], which is a reason for the high frequency weighting in the domain of 1-10 Hz in Figures 2.8 and 2.9.

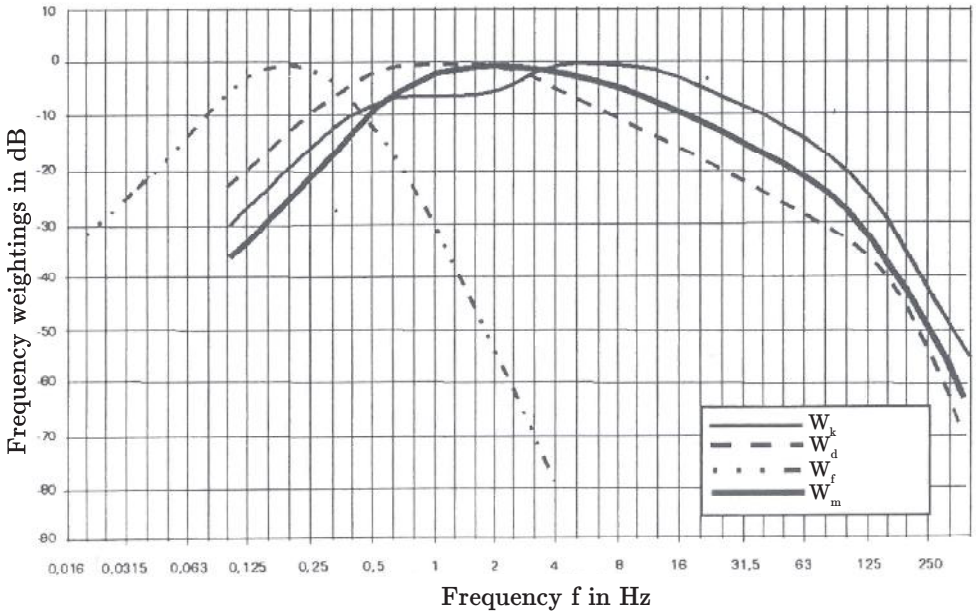

Figure 2.8: Frequency-weighting function W according to VDI standards [59]

According to [59], the use-cases of this weightings are as follows:

- Assessment of the health risk connected with vibration exposure in seated and standing position
  - for the vertical axis z (W_k)
  - for the horizontal axes x and y (W_d)
- Assessment of the well-being with vibration exposure beneath the back while in recumbent position
  - for the vertical axis z (W_k)
  - for the horizontal axes x and y (W_d)
- Assessment of the well-being while sitting or standing
  - for the vertical axis z (W_k)
  - for the horizontal axes x and y (W_d)
- Assessment of the well-being with undefined body posture (W_m)
- Assessment of low-frequency vertical vibrations possibly resulting in kinetosis (W_f)

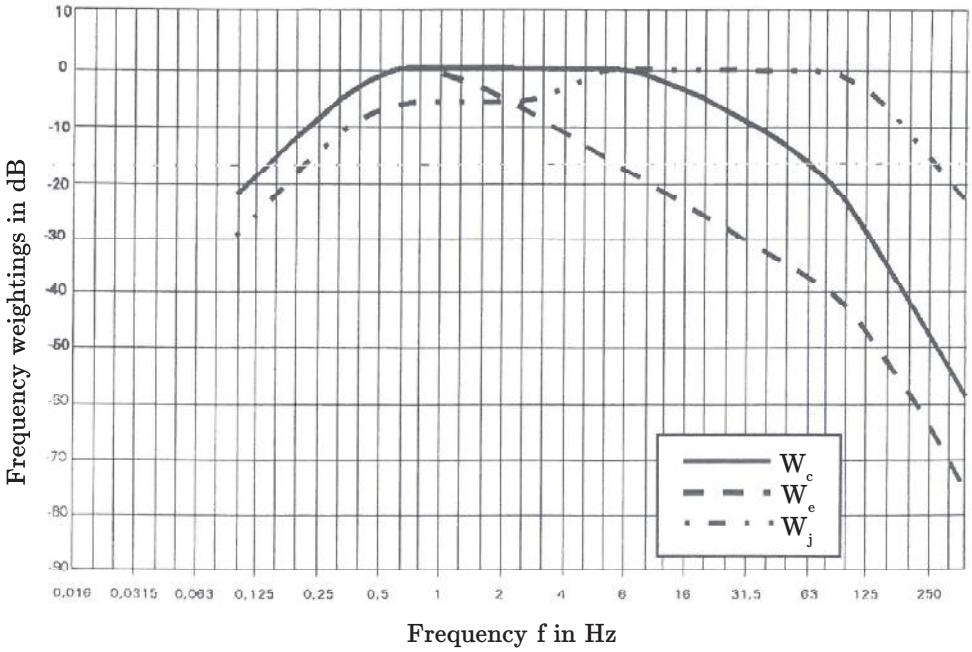

Figure 2.9: Frequency-weighting function W according to VDI standards [59]

The following cases require additional weighting functions [59]:

- Seated position with vibration transferred via the seat back along the x axis (horizontal direction) for the assessment of well-being (W_c)
- Rotational vibrations about three axes x, y and z, for the seated position and for the assessment of well-being (W_e)
- Vibration measurements beneath the head of the individual in a recumbent position, for assessment of the well-being in the case of vertical vibrations (W_j)

The strain on the human body caused by vibration exposure is also influenced by the subjective perception. As the perception and pain thresholds vary from human to human, these thresholds depend on the age, sex, state of health, attentiveness and the kind of activity being engaged in [4]. Table 2.5 depicts the correlation values between human perception and the root-mean-square $a_{w\mathcal{T}}$ of the frequency-weighted acceleration $a_w(t)$.

The root-mean-square $a_{w\mathcal{T}}$ of the frequency-weighted acceleration $a_w(t)$ is used for assessing the strain on a human being caused by the effects of vibration. The frequency-weighted acceleration $a_w(t)$ obtained by applying a frequency weighting function (compare Figures 2.8 - 2.9 and Table 2.4) to the acceleration signal $a(t)$. The root-mean-square $a_{w\mathcal{T}}$ of the frequency-weighted acceleration $a_w(t)$ describes the strain of the human body

Table 2.4: Summary of application of frequency weighting curves [59]

Body posture	Measuring point	Direction of vibration	Frequency weighting
Strain criterion: Health			
Sitting	on the seat	z	W_k
		x, y	W_d
Strain criterion: Well-being			
Sitting	on the seat	z	W_k
		x, y	W_d
	foot platform	x, y, z	W_k
	seat back	x	W_c
	rotation on the seat	r_x, r_y, r_z	W_e
Standing	foot platform	z	W_k
		x, y	W_d
Recumbency	beneath the back	x (vertical)	W_k
		y, z (horizontal)	W_d
	under the head (without cushion)	x (vertical)	W_j
Undefined body posture	in buildings on the floor	x, y, z	W_m
Strain criterion: Kinetosis			
Sitting or Standing		z	W_f

Table 2.5: Relationship between the root-mean-square of the frequency-weighted acceleration $a_w(t)$ and subjective perception in the case of sinusoidal vibration [59]

Root-mean-square $a_{w\mathcal{T}}$ of frequency-weighted acceleration $a_w(t)$ in m/s^2	Description of perception
<0.01	not perceptible
0.015	threshold of perception
0.02	barely perceptible
0.08	easily perceptible
0.315	strongly perceptible
>0.315	extremely perceptible

for a specified time period and is calculated as follows:

$$a_{w\mathcal{T}} = \sqrt{\frac{1}{\mathcal{T}} \int_0^T a_w^2(t) \mathrm{d}t}. \tag{2.1}$$

The variable $\mathcal{T}$ denotes the duration of the measurement whereas $a_w(t)$ is the current acceleration under consideration of the frequency weighting.

[59] also introduces a moving root-mean-square $a_{w\tau}(t)$:

$$a_{w\tau}(t) = \sqrt{\frac{1}{\tau} \int_{\xi=0}^{t} a_w^2(\xi) \mathrm{e}^{\left[\frac{\xi - t}{\tau}\right]} \mathrm{d}\xi}, \tag{2.2}$$

The time is equal to the integration variable ξ and τ is the time constant for the moving average. Depending on the value used for τ, the notation is slightly changed: For $\tau = 1\,\mathrm{s}$, $a_{w\tau}(t)$ becomes $a_{wS}(t)$ where the index S denotes "slow". When setting $\tau = 0.125\,\mathrm{s}$ the index F for "fast" is used: $a_{wF}(t)$. The value of $\tau = 0.125\,\mathrm{s}$ is recommended by [59] to prevent health endangerment due to effects of exposure to whole-body vibration. The frequency weighted acceleration $\hat{a}_w(\bar{w})$ is obtained by multiplying the acceleration in the frequency domain $\hat{a}(\bar{w})$ with the associated frequency rating $W(w)$. Thereby, the variable $W(w)$ denotes one of the aforementioned frequency ratings W_c, W_d, W_e, W_f, W_j, W_k or W_m, depending on the investigated effect:

$$\hat{a}_w(\bar{w}) = W(w) \cdot \hat{a}(\bar{w}) \tag{2.3}$$

The energy content of the vibration is given by the power spectral density which is calculated according to Equation (2.4).

$$\Phi_a(w) = \lim_{\mathcal{T} \to \infty} \frac{1}{\mathcal{T}} (\hat{a}(w))^2 \tag{2.4}$$

The total value of the vibration in all three directions of the frequency-weighted acceleration is given by

$$a_{wv} = \sqrt{k_x^2 a_{wx}^2 + k_y^2 a_{wy}^2 + k_z^2 a_{wz}^2} \tag{2.5}$$

where a_{wx}, a_{wy} and a_{wz} denote the frequency-weighted acceleration along the x, y and z axis. The correction factors k need to be adapted depending on the investigated effect. For vibration exposure while transporting people k_x=1, k_y=1 and k_z=1 holds. Thus, Equation (2.5) simplifies to

$$a_{wv} = \sqrt{a_{wx}^2 + a_{wy}^2 + a_{wz}^2}. \tag{2.6}$$

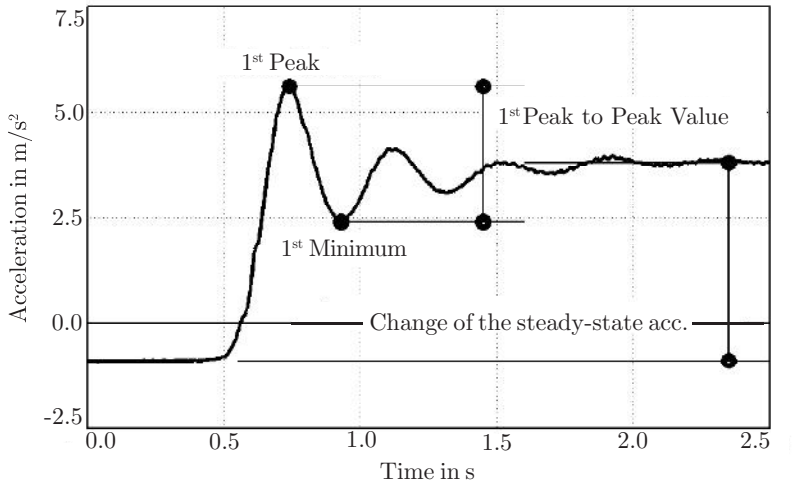

Figure 2.10: Different assessment criteria for drivability on a time domain basis [28]

The vibration dose value (VDV) is another criterion for assessing the load caused by vibration [18]. It is calculated using the "4$^{\text{th}}$ power law" shown in Equation (2.7).

$$\text{VDV} = \sqrt[4]{\int_0^T a_w^4(t)\,\mathrm{d}t} \tag{2.7}$$

Further methods of driveability assessment include measurements in the time domain as suggested by [28]. Investigated parameters are are the first peak acceleration, the first minimum, the first peak-to-peak value and the change of steady-state acceleration as shown in Figure 2.10.

In [60] the author presents measurements performed to assess driveability during a tip-in manoeuvre, which is shown in Figure 2.11. As the vehicle acceleration does not immediately follow the driver input (full throttle), a sag in the acceleration occurs deteriorating vehicle driveability. This is experienced as rather unpleasant, because the driver expects the vehicle to immediately follow his input without any hesitation. Vehicles with automatic transmissions for example, switch to a lower gear when the kickdown is triggered, resulting in an acceleration delay. Besides the tip-in manoeuvre several other driving manoeuvres have been developed for assessing driveability. Table 2.6 gives an overview based on [41].
Driver induced load variations occurring during a tip-in manoeuvre or by engaging the clutch for example, cause oscillations of the drivetrain. These comfort reducing phenomena can be categorized according to their frequency range.
Shunt phenomena (also referred to as "Bonanza-effect") are caused by poorly damped vehicle oscillations. The vibrations can be divided into a rotatory part acting in the drivetrain and a longitudinal proportion occuring in the vehicle body. Both fractions can be

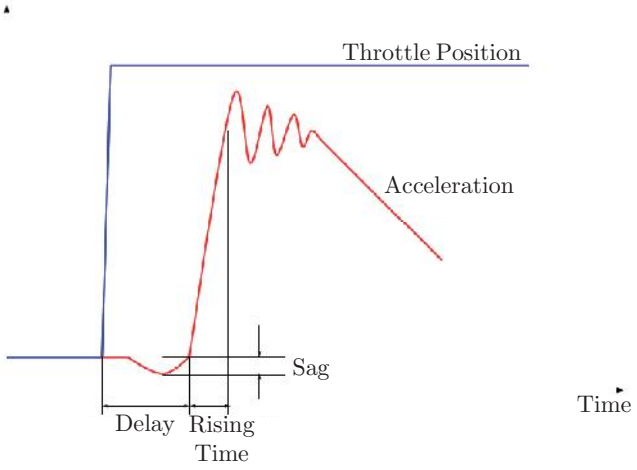

Figure 2.11: Different assessment criteria for drivability on a time domain basis for a tip-in manoeuvre [60]

measured at the driver's seat and have an eigenfrequency of 2-10 Hz. The actual value depends on the drivetrain layout, the stiffness, inertia and current gear ratio. Whereas this phenomenon does not deteriorate acoustics, it hugely affects driving comfort as humans are extremely perceptive for oscillations in this frequency range [4].
Load change shocks occur at higher revolutions and result in an alternation of the torque bracing. Due to the eigenfrequency of 15-200 Hz, this phenomenon affects the vibration comfort and the acoustics [53].
Clonk phenomena can be witnessed with lower gears and at a low revolution range. The alternation of the drivetrain load causes oscillations of the components fitting with clearances. The collisions of the parts result in a high frequency metallic sound in the frequency range of 300-6000 Hz [4].
When investigating the aforementioned effects (compare Section 3.1 and 4.1), the sampling frequency has to be chosen according to the Nyquist-Shannon sampling theorem: *The sampling frequency should be at least twice the highest frequency contained in the signal.* In practice, the sampling frequency is 8-10 times the signal frequency in order to allow a reconstruction of the original signal out of the time-discrete signal without information loss. [14]

The main task when performing objective driveability evaluation lies in the determination of rating quantities (such as the acceleration peak of a tip-in manoeuvre) based on vehicle measurement data (e.g longitudinal acceleration). Further it needs to be investigated which quantities are representative for a phenomenon and therefore need to be considered in the evaluation process. [28] suggests that the correlation between rating quantities and investigated phenomena can be categorized into the following 3 methods:

Table 2.6: Different driving manoeurves for evaluation of the driveablity of a vehicle [41]

Manoeuvre	Criteria	Additional information
Acceleration	Acceleration gradient, elasticity, full load, 0-100 km/h, steady torque, torque increase, torque response	
Constant speed	Speed fluctuation, noise	
Drive away	Acceleration peak, acceleration performance	Creep, hill climbing, launch, vehicle stop
Engine shut off/on		
Motoring	Expected deceleration	DFCO on/off
Noise	Constant speed, engine start, full load acceleration, motoring, normal driving, tip-in	A-weighted filter with averaging time of 125 ms to focus on frequencies around 3-6 kHz
Tip-in	Jerk, peak-to-peak, response delay, sag	After constant speed, during acceleration, short tip-in after constant speed, ...
Tip-out	Jerk, peak-to-peak, response delay	

- Each phenomenon is rated with exactly 1 quantity, meaning that rating quantity and evaluation index are identical
- Several quantities are used for rating one phenomenon without combining them to one single assessment value
- Each phenomenon is rated with several quantities which are transformed into 1 single evaluation index by considering the correlations between the measured quantities and subjective assessments

Whereas the first method lacks of descriptive quantities for the investigated phenomena, the second one makes it difficult to perform an objective assessment as the consideration of several numeric values is necessary. The third approach is the most sophisticated one and also used in AVL-Drive. AVL-Drive is a commercially available tool for the objective evaluation of driveability introduced in 1998. This tool can be applicated in real

Table 2.7: AVL driveability ratings and description [35]

Rating	Subjective Rating	
10	excellent	Not noticeable even by experienced test drivers
9	very good	Disturbing for experienced test drivers
8	good	Disturbing for critical customers
7	satisfying	Disturbing for several customers
6	even satisfying	Disturbing for all customers
5	adequate	Very disturbing for all customers
4	defective	Felt to be deficient by all customers
3	insufficient	Reclaimed as deficient by all customers
2	bad	Limited vehicle operating only
1	very bad	Vehicle not operating

vehicle measurements as well as in simulation, therefore enabling objective driveability evalutaion during the complete vehicle development process. [35]
AVL-Drive uses 270 driveability criteria and differs 75 driving modes. After performing the detection of the driving mode (e.g. idling) via fuzzy logic, the driveability calculation unit evaluates driveability online by using ANNs. The result is a rating from 1-10 shown in Table 2.7 [35].

3 Methodology

3.1 HEV Drivetrain Modelling

To investigate driveability issues at an early stage of development, a detailed model of the hybrid drivetrain is required. Figure 3.1 depicts the implemented combined HEV drivetrain layout. By using merely the EMG_{II} as propulsion unit the HEV operates all-electric. The electric energy is either supplied by the battery or by the EMG_{I} operating as an electric generator (EG), which converts the power delivered by the internal combustion engine. In this mode the vehicle behaves like a serial HEV. Parallel mode is activated when engaging the clutch (CL) and directly powering the wheels by the ICE.

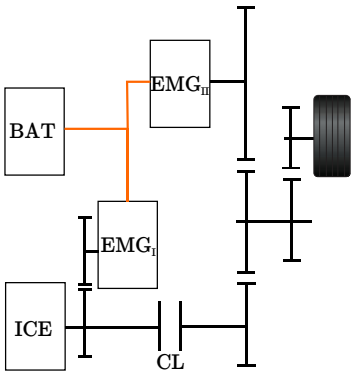

Figure 3.1: Implemented drivetrain layout

3.1.1 Modeling Approaches

Due to the complexity of HEVs and the necessity of frontloading during the development process, the simulation of HEVs has become indispensable. There are two main types of simulation models which will be described in the following.

3.1.1.1 Dynamic Models

Dynamic models describe the vehicle behavior by using algebraic and differential equations. This results in higher physical accuracy and also allows the investigation of dynamic effects and driveability assessments [26].
Figure 3.2 shows that dynamic models have the benefit of a physically correct power flow: The pedal input of the driver is used to determine the ICE torque which is then used to calculate the resulting forces at the wheels under consideration of the gearbox and other powertrain components such as the final drive for example [1].

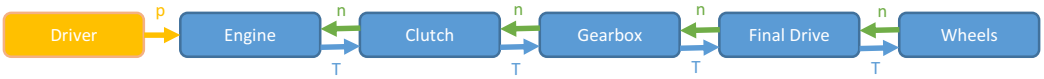

Figure 3.2: Dynamic vehicle model

3.1.1.2 Quasistatic Models

Quasistatic models use velocity, acceleration and road inclination as input variables. The driving cycle is discretized into steps (typically 1 s [19]), for which the inputs are assumed to be constant. Due to the consideration of acceleration forces, the approach can be regarded as quasistatic. The resistance forces (compare Section 3.1.2) are then used to determine the force acting on the wheels. From the tire forces the operating point of the motor can be calculated under consideration of the drivetrain losses as shown in Figure 3.3.
As most of the influence factors on fuel consumption are relatively slow [19], a quasistatic model will be used for the determination of the fuel saving potential given by the predictive charging strategy described in Section 3.4.

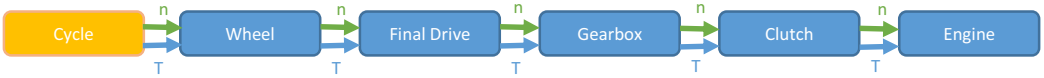

Figure 3.3: Quasistatic vehicle model

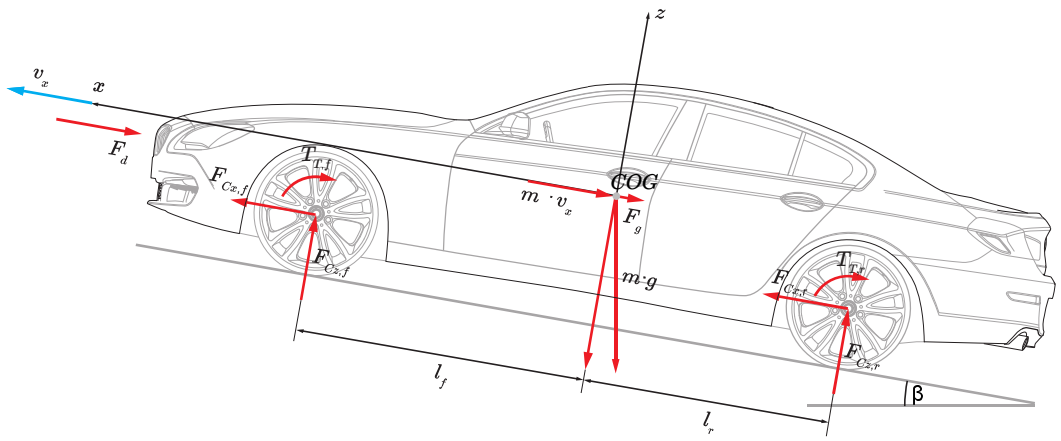

Figure 3.4: Resistance forces [32]

3.1.2 Longitudinal Vehicle Dynamics

Longitudinal vehicle dynamics describe vehicle movements in driving direction (longitudinal direction). Driving and braking performance as well as fuel efficiency and noise emissions are mainly evaluated [25].

Resistance Forces

The driving resistance forces comprise rolling resistance, air resistance, climbing resistance and acceleration resistance [25] and are illustrated in Figure 3.4.

The variables used in Equations 3.1 - 3.4 refer to the following physical quantities:

- v_x ... velocity in longitudinal direction
- a ... acceleration in longitudinal direction
- g ... gravity constant
- m ... vehicle mass
- β ... inclination angle

Rolling resistance

The rolling resistance F_r is a result of the viscoelastic deformation of the tire [25]. The material pairing between tire and ground and the tire pressure are the main influence factors on the rolling resistance. Higher tire pressure results in a lower rolling resistance coefficient a_R and vice versa if other parameters are kept constant.

$$F_r = a_R \cdot m \cdot g \cdot \cos(\beta) \tag{3.1}$$

Air resistance

The longitudinal air resistance force (air drag) F_d shows a quadratic dependence on the velocity and can be approximated by Equation (3.2) which contains the resistance coefficient c_W, the air density ρ_A and the front view surface A_f.

$$F_d = \frac{1}{2} c_W \cdot \rho_A \cdot A_f \cdot v_x \cdot |v_x| \tag{3.2}$$

Climbing resistance

The climbing resistance F_g needs to be taken into account when the inclination β towards the horizontal is unequal to zero.

$$F_g = m \cdot g \cdot \sin(\beta) \tag{3.3}$$

Acceleration resistance

a) Translational

According to Newton's second law of motion, acceleration forces F_a are necessary for the alternation of motion (acceleration).

$$F_a = m \cdot a \tag{3.4}$$

b) Rotational

For rotating components such as axles, wheels, the rotational acceleration resistance has to be considered. The required momentum for acceleration T_a is a function of the inertia Θ and the angular acceleration $\dot{\omega}$:

$$T_a = \Theta \cdot \dot{\omega} \tag{3.5}$$

Equation of motion solved in the dynamic model

The longitudinal vehicle motion is described in Equation (3.6).

$$m \cdot a = F_t - F_d + F_g + F_r \tag{3.6}$$

The propulsion force F_t acting on the tires is calculated within the tire model described later in this section and therefore also considers tire slip.

3.1.3 Internal Combustion Engine (ICE)

Throughout history a great variety of internal combustion engines have developed. The layouts range from the most commonly used piston engine over rotary engines up to radial engines. The powertrain of the HEV described in this thesis comprises an Otto piston engine, working according to the four-stroke principle: After intake and compression the air-fuel mixture is ignited by a spark plug. The generated heat causes high pressure in the combustion chamber which is then converted into mechanical energy during the expansion phase. The complete combustion of fossil fuels $C_\pi H_\rho O_\sigma$ according to [39] can be expressed as follows:

$$C_\pi H_\rho O_\sigma \left(\pi + \frac{\rho}{4} - \frac{\sigma}{2}\right) O_2 \rightarrow \pi CO_2 + \frac{\rho}{2} H_2O \tag{3.7}$$

As Equation (3.7) is not applicable for incomplete combustion, besides CO_2 other emission components such as CO and HC are produced. The amount of NOx emission rises with temperature and particulate matter (PM) is a result of small mixture formation time [21]. Since no data is available, emissions are not considered in this work.

Mean Value Model

The demanded ICE torque T_{ICE} is characterised by the angular velocity ω_{ICE} and the accelerator pedal postion p_p:

$$T_{ICE} = f(\omega_{ICE}, p_p) \tag{3.8}$$

Sophisticated engine models such as *en-DYNA* are not taken into consideration here, as the described approach is sufficient for vehicle handling and ride analysis [49]. The described engine map is usually measured on a dynamometer, but unfortunatley not available for this thesis. It was therefore assumed, that $p_p = 0$ represents the engine's drag torque $T_{ICE,drag}$, whereas $p_p = 1$ results in the full load curve $T_{ICE,max}$. Inbetween these values linear interpolation is performed [32], compare Equation (3.9). The resulting ICE map is shown in Figure 3.5.

$$T_{ICE}(\omega_{ICE}) = T_{ICE,drag}(\omega_{ICE}) + p_p \left[-T_{ICE,drag}(\omega_{ICE}) + T_{ICE,max}(\omega_{ICE})\right]. \tag{3.9}$$

As the drag torque summarises the internal engine friction and other losses, such as the compression of the air, it is less than zero and increases linearly with the engine speed ω_{ICE} [38].

The ICE dynamics are formulated with the principle of angular momentum:

$$\Theta_{ICE} \cdot \dot{\omega}_{ICE} = T_{ICE} - T_{ICE,out}. \tag{3.10}$$

The variable Θ_{ICE} represents the inertia of the engine and $T_{ICE,out}$ is the momentum at the crankshaft. As it is necessary to consider the combustion delay and the intake

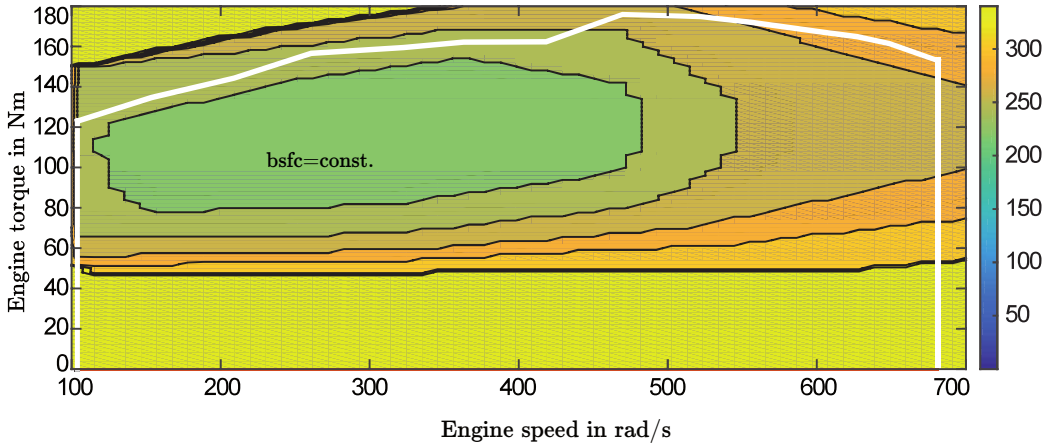

Figure 3.5: Implemeted ICE map with its brake specific fuel consumption in g/kWh

process, a first-order lag element in combination with a dead-time element according to [30] found application to model the system response time. The transfer function G_l of a first-order lag element in the s-domain is a function of the amplification factor $K_{l,ICE}$ and the time constant $T_{l,ICE}$:

$$G_l(s) = \frac{K_{l,ICE}}{1 + sT_{l,ICE}}. \tag{3.11}$$

The transfer function G_d of the dead-time element depends on the time constant $T_{d,ICE}$:

$$G_d(s) = e^{-sT_{d,ICE}}. \tag{3.12}$$

The ICE's fuel consumption $\dot{m}_f(t)$ shows a dependency on the ICE speed ω_{ICE} and the required load T_{ICE} and is therefore modelled likewise:

$$\dot{m}_f(t) = f(\omega_{ICE}(t), T_{ICE}(t)). \tag{3.13}$$

To account for the fuel efficiency of the engine a brake specific fuel consumption $bsfc$ [15] map was implemented. The correlation between engine efficiency η_{ICE} and $bsfc$ is shown in Equation (3.14). The variable $\dot{m}_f$ stands for the fuel mass flow, H_u represents the fuel's lower heating value and P_{ICE} is the effective engine power.

$$bsfc = \frac{\dot{m}_f}{P_{ICE}} = \frac{1}{\eta_{ICE} \cdot H_u} \tag{3.14}$$

Engine control unit (ECU)

Modern engines are controlled by numerous electronic control units, for example mixture- and idle speed control [15], which have a main influence on the engine characteristic. Therefore, modeling ICE behavior always includes control algorithms [38]. ECUs have the aim of improving fuel consumption, emissions and driveability. The implemented controllers in this thesis comprise the engine speed limiter, the idle speed controller, the deceleration fuel cut-off and an automatic start-/stop function. The engine speed limiter is integrated into the engine map, by having the engine provide zero torque at maximum engine speed. Idle speed control is performed using a proportional-integral-differential (PID) controller. DFCO is a way of increasing fuel efficiency by stopping fuel injection during tow phases. The automatic start-/stop function stops the ICE at stop for conventional vehicles. For HEVs the start-/stop function also controls electric driving.

3.1.4 Battery

Lead-acid batteries are a common element in conventional drivetrains. But when talking about batteries in combination of HEVs, this term refers to the energy storage device (ESS). In general an ESS can rely on mechanical, chemical or electrical storage principles, whereas the most common is the electrical storage system in the form of a lithium-ion battery [31]. Batteries convert chemical into electrical energy by performing a redox reaction. The electrode at which the oxidation occurs is called anode whereas the electrode where the reduction takes place is called cathode. To account for the ion transport, an electrolyte is necessary. For automotive applications many of these galvanic cells are combined to battery packs by serial and/or parallel arrangement. When designing a battery system for HEVs the following aspects should be considered: high specific power, high specific energy, long calendar and cycle life, low initial and replacement costs, high reliability, and high robustness [19].

With respect to the model requirements battery models can be categorized as follows [29]:

- Mathematical black-box models,
- Physical-chemical models,
- Equivalent-circuit models.

Equivalent-circuit models describe the battery characteristics by the use of resistances, inductances and capacitances. As this model type reproduces the basic dynamic effects with appropriate accuracy without long computation times, this type was chosen for the implemented battery model which is depicted in Figure 3.6. Being a simplification of the Randles model, the following effects are considered: self-discharging, the SOC dependency of the open-circuit voltage U_{oc} and thermal effects. While retaining good

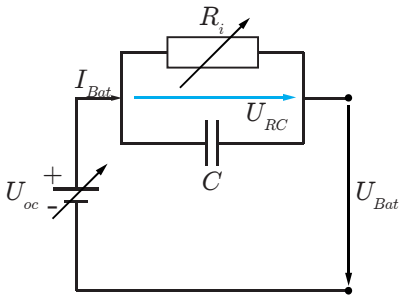

Figure 3.6: Equivalent-circuit model of the implemented battery model [32]

accuracy, the parametrization is facilitated in comparsion to the Randles model due to the simplifications [62].

An ideal voltage-source provides the open-circuit voltage U_{oc}, which is a function of the battery temperature ϑ_{Bat} and the SOC. To account for the dynamic behavior, a RC-element was implemented. The internal resistance $R_i(SOC, \vartheta_{Bat})$ is comprised as follows:

$$R_i = R_d + R_{ct} + R_o. \tag{3.15}$$

The diffusion resistance R_d models the diffusion of ions in the electrolyte, whereas R_{ct} denotes the "charge-transfer" resistance caused by the electron movement [19]. The variable R_o is the ohmic resistance.

The capacitive effects of the charge accumulation-/ separation occurring at the interface between the electrodes and electrolyte are depicted by the capacitance C [19]. The dynamic behavior is described by Kirchhoff's laws:

$$C\frac{\mathrm{d}}{\mathrm{d}t}U_{RC} = I_{Bat} - \frac{U_{RC}}{R_i}, \tag{3.16}$$

$$U_{Bat} = U_{oc} - U_{RC}, \tag{3.17}$$

The voltage drop in the RC-branch is accounted by U_{RC}, the battery voltage is denoted by U_{Bat} and the battery current by I_{Bat}. Given the initial SOC of the battery SOC_0 and its nominal capacity Q_{nom}, the current state of charge $SOC(t)$ reads

$$SOC(t) = SOC_0 - \int_0^t \frac{I_{Bat}}{Q_{nom}}\,\mathrm{d}\tau. \tag{3.18}$$

Battery management system (BMS)

The battery monitoring unit accounts for the battery's health throughout its lifetime by permanently supervising the battery voltage U_{Bat} and current I_{Bat} as well as the SOC. To prevent lithium plating, the current and power need to be limited, which is described in Section 3.2.3. As severe discharging results in capacitance loss and higher self-discharging effects and over-voltage causes spontaneous ignition [31], the cell voltage is also monitored.

3.1.5 Electric Motor/Generator (EMG)

The electric motor/generator is a key component of HEVs [19]. Whereas in purely ICE propelled vehicles the EMG is only used as a starter/alternator, the EMG is an active part of the drivetrain in HEVs, which can operate in the following modes (compare [19]):

1. Conversion of electrical power into mechanical power used for propulsion
2. Conversion of mechanical power from the ICE into electrical power in order to charge the battery
3. Recuperation of mechanical power to charge the battery (regenerative braking)

The number of EMGs varies depending on the drivetrain layout [26], the HEV investigated in this thesis consists of two EMG units. The stronger one ($\mathrm{EMG_I}$) is used as a traction motor, whereas the $\mathrm{EMG_{II}}$ provides additional electrical power for the battery and/or $\mathrm{EMG_I}$. According to the type of current used, EMGs can be categorized into direct current (DC) and alternating current (AC) machines. Nevertheless, the general layout always stays the same, consisting of a stator and a rotor.

Phenomenological EMG model

The mechanical behavior of the EMG can be described with the following Equation:

$$\Theta_{EMG} \cdot \dot{\omega}_{EMG} = T_{EMG} - T_{EMG,out}. \tag{3.19}$$

The variable Θ_{EMG} denotes the EMG's rotor inertia, T_{EMG} the demanded torque, ω_{EMG} the rotational speed and $T_{EMG,out}$ the momentum at the output shaft, respectively. The EMG's response time is modeled using a first-order lag element [36].

The current required for the demanded output torque $T_{EMG,out}$ can be calculated by transforming the mechanical energy demanded into the corresponding electrical energy under consideration of the EMG efficiency η_{EMG}. The EMG efficiency map and rotational speed-torque characteristic is shown in Figure 3.7. Using the principle of energy conservation, the required current I_{EMG} reads:

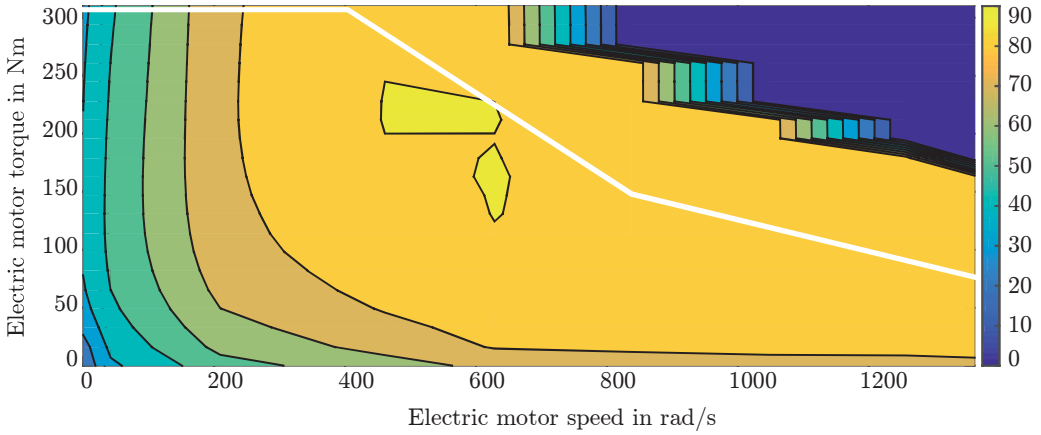

Figure 3.7: EMG characteristics of the implemented models with its mechanical efficiency

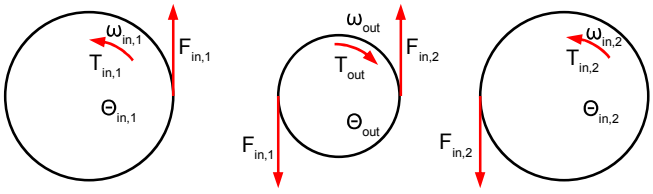

Figure 3.8: Schematic representation of the implemented gearbox model

$$I_{EMG} = \frac{T_{EMG} \cdot \omega_{EMG}}{U_{Bat}} \cdot \eta_{EMG}^{-\text{sgn}(T_{EMG})}. \tag{3.20}$$

The signum function accounts for the direction of power conversion: In motor mode ($T_{EMG} >= 0$) provokes a division of the efficiency, whereas in generator mode T_{EMG} is less than zero, leading to a multiplication of η_{EMG}. The voltage of the battery is denoted by U_{Bat}.

3.1.6 Gearbox (GBX)

Gearboxes or transmissions are a crucial part in conventional drivetrain layouts as well as in hybrid electric vehicles. They are essential in terms of fuel efficiency and also allow to adapt the angular speed and momentum provided by the traction motor to be converted into the measures requested at the wheels. The investigated HEV drivetrain consists of two gearbox modules: One connecting the ICE and the EMG_I, the other acting as a summation gear between the ICE and EMG_II, see Figure 3.8. The two modules are

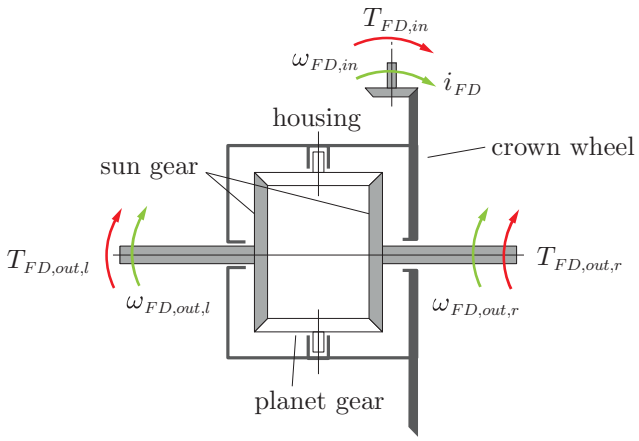

Figure 3.9: Schematic representation of a final drive [32]

implemented considering the inertias of the input shafts ($\Theta_{in,1/2}$) and the output shaft (Θ_{out}):

$$T_{out} = T_{in,1} \cdot i_1 + T_{in,2} \cdot i_2 - \dot{\omega}_{out}(\Theta_{in,1} \cdot i_1^2 + \Theta_{in,2} \cdot i_2^2 + \Theta_{out}), \tag{3.21}$$

$$\omega_{in,1} = \omega_{out} \cdot i_1, \tag{3.22}$$

$$\omega_{in,2} = \omega_{out} \cdot i_2. \tag{3.23}$$

The variable T_{out} denotes the torque at the output-shaft, $i_{1/2}$ the gear ratio, $T_{in,1/2}$ the torque at both input shafts and $\dot{\omega}_{out}$ the angular acceleration of the output-shaft, respectively. The rotational speeds of the output-shaft and both input shafts are given by ω_{out} and $\omega_{in,1/2}$.

3.1.7 Final Drive (FD)

The final drive allows the wheels to rotate at different speeds while retaining equal torque distribution. If the driven wheels rotate at the same speed, the pinion gears are not moving (see Figure 3.9). In case of a speed difference of the wheels (e.g caused by cornering or μ-split surfaces) the pinion gears start moving and mechanical power is dissipated [17]. To prevent high traction losses, locked differentials are used which can provide a degree of lock up to 100% .

As no wheel speed balancing is considered in the longitudinal simulation model, the FD is modelled as a rigid axle without considering any inertia. The torque $T_{FD,out,l/r}$ and the angular speed $\omega_{FD,in}$ are calculated under consideration of the FD gear ratio i_{FD}, the torque at the input shaft $T_{FD,in}$, the efficiency η_{FD} and the rotational speeds of the left and right output shafts $\omega_{FD,out,l}$ and $\omega_{FD,out,r}$:

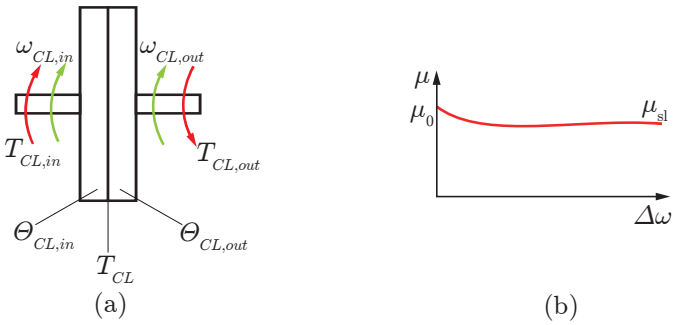

Figure 3.10: Dynamics of the clutch and a charactertistic curve. In (a) the clutch dynamics are depicted, in (b) a specific friction characteristics for a specific friction pad is represented. [32]

$$T_{FD,out,l/r} = \frac{1}{2} i_{FD} \cdot T_{FD,in} \cdot \eta_{FD}, \tag{3.24}$$

$$\omega_{FD,in} = \frac{1}{2} \cdot i_{FD} \left(\omega_{FD,out,l} + \omega_{FD,out,r} \right). \tag{3.25}$$

The final drive efficiency η_{FD} is assumed to be a bit lower than the transmission efficiency η_{GBX} which is caused by the bevel gear used. The efficiency reads:

$$\eta_{FD} = \begin{cases} \leq 1 & T_{FD,out,l/r} \geq 0, \\ > 1 & T_{FD,out,l/r} < 0. \end{cases} \tag{3.26}$$

3.1.8 Clutch (CL)

The task of the clutch is to disengage the traction unit from the remainder drivetrain, to provide a comfortable start-up process and to adapt the angular speeds of the input and output shafts [9]. The momentum transferred by the clutch is given by T_{CL}, which is a function of the number of friction plates N_{plates}, the mean friction radius r_m, the friction coefficient μ and the axial force $F_{x,CL}$:

$$T_{CL} = N_{plates} \cdot r_m \cdot \mu \cdot F_{x,CL}. \tag{3.27}$$

As depicted in 3.10, μ is a function of the slip $\Delta\omega_{CL}$. Without slip, μ is equal to the static friction coefficient μ_0. If the slip increases, μ reduces to the sliding friction coefficient μ_{sl}.

Modelling the clutch behavior is quite complex, as the two inertias $\Theta_{CL,in}$ and $\Theta_{CL,out}$ move independently during slipping [63]. The formulation in [63] has the benefit of

good stability and was therefore chosen for this thesis. The relations for a fully engaged clutch (reduced order) are shown in Equation (3.28), whereas the system equations for the slipping clutch ($\omega_{CL,out} \neq \omega_{CL,in}$) are depicted in Equation (3.29).

$$(\Theta_{CL,in} + \Theta_{CL,out}) \cdot \dot{\omega}_{CL} = T_{CL,in} - T_{CL,out} \qquad \omega_{CL,in} = \omega_{CL,out} = \omega_{CL} \tag{3.28}$$

$$\underbrace{\begin{bmatrix} \Theta_{CL,in} & 0 \\ 0 & \Theta_{CL,out} \end{bmatrix}}_{\mathbf{M}} \cdot \underbrace{\begin{bmatrix} \dot{\omega}_{CL,in} \\ \dot{\omega}_{CL,out} \end{bmatrix}}_{\dot{\boldsymbol{\omega}}} = \underbrace{\begin{bmatrix} T_{CL,in} \\ -T_{CL,out} \end{bmatrix}}_{\mathbf{T}} - \underbrace{\begin{bmatrix} 1 \\ -1 \end{bmatrix}}_{\mathbf{d}^T} \cdot T_{CL} \cdot \operatorname{sgn}\left(\underbrace{\begin{bmatrix} 1 & -1 \end{bmatrix}}_{\mathbf{d}} \cdot \underbrace{\begin{bmatrix} \omega_{CL,in} \\ \omega_{CL,out} \end{bmatrix}}_{\boldsymbol{\omega}} \right) \tag{3.29}$$

The mass matrix is denoted by $\mathbf{M}$, the angular acceleration vector by $\dot{\boldsymbol{\omega}}$, the vector containing the coefficients by $\mathbf{d}$ and the angular speed vector by $\boldsymbol{\omega}$, respectively.

[63] suggests a state space transformation which decouples the main dynamics from the relative dynamics. This is performed by introducing the transformation matrix $\mathbf{K}$ and using $\Theta_{CL,\Sigma} = \Theta_{CL,in} + \Theta_{CL,out}$:

$$\mathbf{K} = \begin{bmatrix} 1 & \frac{\Theta_{CL,out}}{\Theta_{CL,\Sigma}} \\ 1 & -\frac{\Theta_{CL,in}}{\Theta_{CL,\Sigma}} \end{bmatrix} \tag{3.30}$$

The transformation of the angular speed vector $\boldsymbol{\omega}$ into the generalised speed vector $\mathbf{z}$ is given by:

$$\boldsymbol{\omega} = \mathbf{K}\mathbf{z} \tag{3.31}$$

After introducing $\Theta_{CL,\Pi} = \Theta_{CL,in} \cdot \Theta_{CL,out}$, the system dynamics read

$$\begin{bmatrix} \dot{z}_1 \\ \dot{z}_2 \end{bmatrix} = \begin{bmatrix} \frac{1}{\Theta_{CL,\Sigma}} & \frac{1}{\Theta_{CL,\Sigma}} \\ \frac{\Theta_{CL,out}}{\Theta_{CL,\Pi}} & -\frac{\Theta_{CL,in}}{\Theta_{CL,\Pi}} \end{bmatrix} \begin{bmatrix} T_{CL,in} \\ -T_{CL,out} \end{bmatrix} - T_{CL} \begin{bmatrix} 0 \\ \frac{\Theta_{CL,\Sigma}}{\Theta_{CL,\Pi}} \end{bmatrix} \operatorname{sgn}\left(\begin{bmatrix} 0 \\ 1 \end{bmatrix}^T \begin{bmatrix} z_1 \\ z_2 \end{bmatrix} \right) \tag{3.32}$$

The variable $\dot{z}_1$ denotes the main dynamics, whereas $\dot{z}_2$ accounts for the relative dynamics. By inverting Equation (3.30), the angular accelerations of the input and output shaft can be obtained. The system described in Equation (3.32) is solved by applying sliding mode theory and using the torque T_{CL} as input variable [63]. If $z_2 = 0$, the transferable momentum switches at a finite frequency between $\pm T_{CL}$. As this frequency is required to be rather high, a small simulation time step needs to be applied, which rises computation time [63].

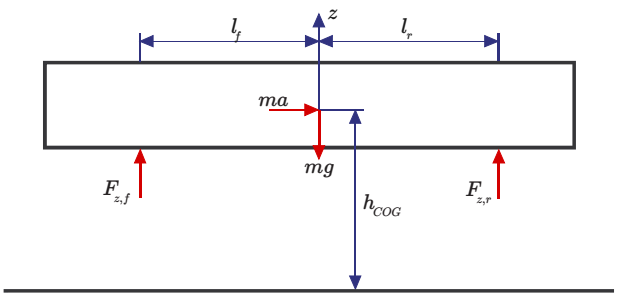

Figure 3.11: Dynamic axle load shifting due to vehicle acceleration, adapted from [25]

3.1.9 Chassis Model

In order to describe the vehicle motion in longitudinal direction a tire model and a hub-pitching model are implemented. Vehicle acceleration or deceleration results in axle load shifts and causes an oscillation of the bodies.

Figure 3.11 shows the axle loads which can be calculated as follows:

$$F_{z,f/r} = F^0_{z,f/r} + F^d_{z,f/r} \tag{3.33}$$

$$F^0_{z,f} = mg \cdot \frac{l_r \cdot \cos\beta - h_{COG} \cdot \sin\beta}{l} \tag{3.34}$$

$$F^d_{z,f} = -ma \cdot \frac{h_{COG}}{l} \tag{3.35}$$

$$F^0_{z,r} = mg \cdot \frac{l_f \cdot \cos\beta + h_{COG} \sin\beta}{l} \tag{3.36}$$

$$F^d_{z,r} = ma \cdot \frac{h_{COG}}{l} \tag{3.37}$$

The static portion of the front and rear axle load is given by $F^0_{z,f/r}$, the dynamic portion by $F^d_{z,f/r}$. The variable h_{COG} represents the height of the center of gravity (COG) and $l_{f/r}$ the distance between the COG and the front and rear axle. The wheelbase l is calculated by l_f+l_r. The road inclination is given by β and the vehicle mass by m.

Equation (3.38) allows to determine the longitudinal vehicle acceleration a:

$$m \cdot a = 2 \cdot (F_{x,f} + F_{x,r}) - F_d - F_g \tag{3.38}$$

The transferable longitudinal tire force at the front or rear wheels is denoted by $F_{x,f/r}$, compare Equation (3.42). The aerodynamic drag F_d, (compare Equation (3.2)), and the resistance force due to the road grade F_g, (compare Equation (3.3)), also need to be taken into account.

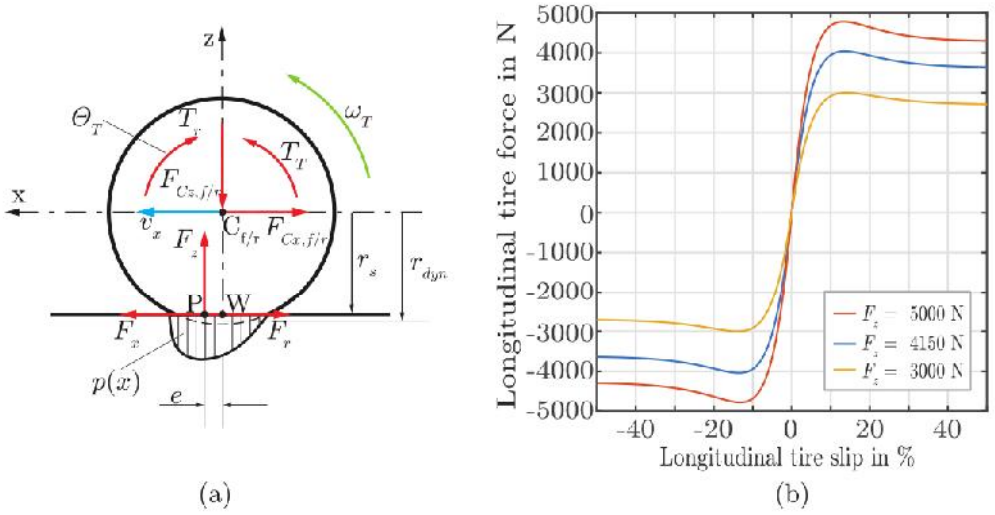

Figure 3.12: Dynamics of the tire and charactertistic curves. In (a) the tire dynamics are depicted, in (b) the tire characteristics for a specific tire are represented. [32]

Tire

The tires are the only interaction point between vehicle and road and transmit all forces. Therefore, an adequate description of the interaction between tires and road is crucial in vehicle dynamics modelling [23].

Semi-physical tire models have the benefits of short simulation time in combination with a physical meaning of the parameters. A well-known representative of this type of simulation models is TMsimple [22], which will be used in this project. The tire dynamics shown in Figure 3.12 read:

$$\Theta_T \cdot \dot{\omega}_T = T_T - F_x \cdot r_{dyn} - F_z \cdot a_R \cdot r_{dyn} \tag{3.39}$$

The inertia of the tire is given by Θ_T, the longitudinal tire force by F_x, the vertical tire load by F_z, the torque acting on the tire by T_T, the dynamic tire radius by r_{dyn} and the rolling resistance coefficient by a_R.

The slip velocity is calculated as follows:

$$v_s = \omega_T \cdot r_{dyn} - v_x \tag{3.40}$$

The longitudinal tire slip s^* reads:

$$s^* = \begin{cases} \frac{v_s}{\omega_T \cdot r_{dyn}} & T_T \geq 0, \\ \frac{v_s}{v_x} & T_T < 0. \end{cases} \tag{3.41}$$

The available longitudinal grip potential F_x can only be affected by the vertical tire load F_z and the longitudinal tire slip s^* if other influences (road surface, temperature ...) are kept constant [24]. The available longitudinal grip potential in the TMsimple approach is calculated by:

$$F_x = K \cdot \sin\left[B\left(1 - e^{\frac{-|s^*|}{A}}\right)\operatorname{sign}(s^*)\right]. \tag{3.42}$$

The coefficients are determined as follows:

$$K = F_{x,max}, \tag{3.43}$$

$$B = \pi - \arcsin\frac{F_{x,inf}}{F_{x,max}}, \tag{3.44}$$

$$A = \frac{1}{dF_{x0}} K \cdot B. \tag{3.45}$$

The parameter $F_{x,max}$ stands for the maximum longitudinal tire force, the saturation value is given by $F_{x,inf}$ and dF_{x0} represents the initial longitudinal tire stiffness. All of these parameters need to be evaluated for a given vertical load F_z. The following approach accounts for the degressive influence of the vertical tire load:

$$F_{x,max}(F_z) = a_1 \frac{F_z}{F_{z,nom}} + a_2 (\frac{F_z}{F_{z,nom}})^2, \tag{3.46}$$

$$F_{x,inf}(F_z) = b_1 \frac{F_z}{F_{z,nom}} + b_2 (\frac{F_z}{F_{z,nom}})^2 \tag{3.47}$$

$$dF_{x0}(F_z) = c_1 \frac{F_z}{F_{z,nom}} + c_2 (\frac{F_z}{F_{z,nom}})^2. \tag{3.48}$$

The coefficients read:

$$a_1 = 2 \cdot F_{x,max}^{F_{z,nom}} - 0.5 \cdot F_{x,max}^{2F_{z,nom}}, \tag{3.49}$$

$$a_2 = 0.5 \cdot F_{x,max}^{2F_{z,nom}} - F_{x,max}^{F_{z,nom}}. \tag{3.50}$$

The coefficients b_1, b_2 and c_1, c_2 are evaluated in the same way, but instead of using $F_{x,max}^{F_{z,nom}}, F_{x,max}^{2F_{z,nom}}$ the saturation value $F_{x,inf}$ and the initial tire stiffness dF_{x0} at the nominal load $F_{z,nom}$ and twice the nominal load $2F_{z,nom}$ have to be used [22].

Hub-Pitching model

For driveability investigations the vertical vehicle dynamics also have to be considered. This is done by a hub-pitching model which is shown in Figure 3.13.

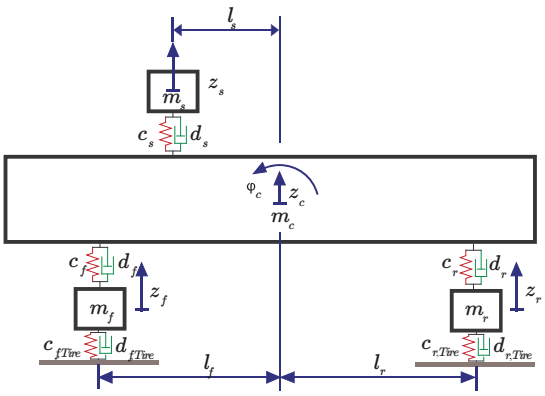

Figure 3.13: Hub-Pitch Model, adapted from [25]

Four rigid bodies are included in the model: The chassis m_c, the seat m_s and the undamped axle masses at front and rear $m_{f/r}$. The horizontal distance between the chassis center of gravity and the axles is given by $l_{f/r}$ whereas the horizontal distance between the COG and the seat is denoted by l_s.

The equation of motion including all undamped masses in vertical direction at the front yields:

$$m_f \cdot \ddot{z}_f = 2 \cdot F_{z,f,Tire} - m_f g - 2 \cdot (F_{s,f} + F_{d,f})\,. \tag{3.51}$$

The linear momentum at the rear including all undamped masses in vertical direction can be written as follows:

$$m_r \cdot \ddot{z}_r = 2 \cdot F_{z,r,Tire} - m_r g - 2 \cdot (F_{s,r} + F_{d,r})\,. \tag{3.52}$$

A multiplication factor of two is necessary, as the tire force $F_{z,f/r,Tire}$ and the spring-/damper forces $F_{s,f/r}$ and $F_{d,f/r}$ are only calculated for one side of the axle. The variables m_f and m_r stand for the undamped masses at the front and rear axle, respectively. The vertical acceleration is denoted by $\ddot{z}_{f/r}$ and the vertical tire force for one tire by $F_{z,f/r,Tire}$.

For the chassis two degrees of freedom are modelled: the translation z_c in vertical direction and the rotation φ_c along the y-axis. The chassis equation of motion (compare Figure 3.14) can be written as:

$$m_c \cdot \ddot{z}_c = 2 \cdot (F_{s,f} + F_{d,f}) + 2 \cdot (F_{s,r} + F_{d,r}) - m_c g. \tag{3.53}$$

Whereas the rotational DOF can be expressed in the following form:

$$\Theta_c \cdot \ddot{\varphi}_c = 2 \cdot l_r \cdot (F_{s,r} + F_{d,r}) - 2 \cdot l_f \cdot (F_{s,f} + F_{d,f}) - (T_f + T_r), \tag{3.54}$$

The variable l_f stands for the horizontal distance between the COG and the front axle, whereas l_r is used for the rear axle. The propulsion or brake torques are considered by T_f and T_r.

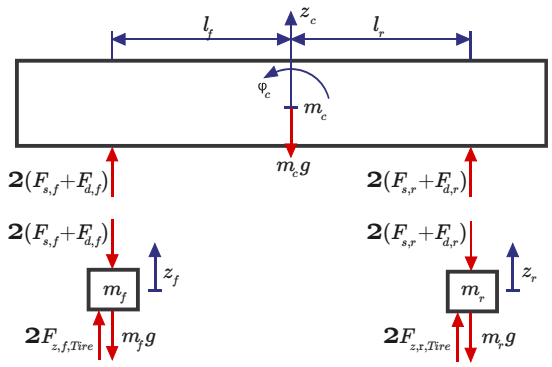

Figure 3.14: Free body diagram of the hub-pitch model, adapted from [25]

The tire force $F_{z,f/r,Tire}$ can be expressed as

$$F_{z,f/r,Tire} = \frac{1}{2} \cdot F^0_{z,f/r,Tire} - F^d_{z,f/r,Tire}. \tag{3.55}$$

For better handling, the tire force is split into two parts: a static $\frac{1}{2}F^0_{z,f/r,Tire}$ and a dynamic $F^d_{z,f/r,Tire}$ load proportion. The dynamic part (under assumption of constant vertical tire stiffness $c_{f/r,Tire}$) is calculated as follows:

$$F^d_{z,f/r,Tire} = c_{f/r,Tire} \cdot (z_{f/r} - z_{Road}). \tag{3.56}$$

As the influence of the tire damping force is negligible, it is not considered here [49]. The variable $F_{s,f/r}$ denotes the force of one suspension

$$F_{s,f/r} = \underbrace{(z_{f/r} - z_{f/r,c})}_{\Delta z_{f/r}} \cdot c_{s,f/r} + \frac{1}{2} \cdot (F^0_{z,f/r} - m_{f,r} g). \tag{3.57}$$

The damper force $F_{d,f/r}$ is determined by

$$F_{d,f/r} = \underbrace{(\dot{z}_{f/r} - \dot{z}_{f/r,c})}_{\Delta \dot{z}_{f/r}} \cdot d_{f/r} \cdot i_{d,f/r}. \tag{3.58}$$

For $\varphi_c << 1$ the chassis movement in z-direction at the position of the spring/damper fixing point $z_{f/r,c}$ and the corresponding vertical velocities $\dot{z}_{f/r,c}$ can be written as

$$z_{f/r,c} = z_c - l_{f/r} \cdot \varphi_c \tag{3.59}$$

$$\dot{z}_{f/r,c} = \dot{z}_c - l_{f/r} \cdot \dot{\varphi}_c \tag{3.60}$$

The spring damper conversion $i_{d,f/r}$ is the ratio of the absolute speed in direction of the spring-/damper axis and the absolute value of the vertical velocity of the wheel [25].

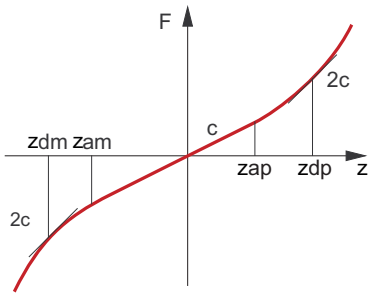

(a) Spring characteristic

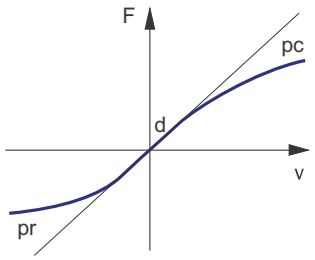

(a) Damper characteristic

Figure 3.15: Spring-Damper characteristics. In (a) the modelled spring characteristics are depicted, in (b) the corresponding damper behavior is shown.

For this thesis, $i_{d,f/r}$ is assumed to be 1. Therefore, when comparing the damper forces between the real vehicle $F_{d,real}$ and the simulation model $F_{d,sim}$, the following relation applies:

$$F_{d,sim} = F_{d,real} \cdot i_{d,f/r}. \tag{3.61}$$

[48] suggests the spring characteristics to be modelled progressive and nonlinear:

$$c_{s,f/r} = \begin{cases} c_{f/r,0} & z_{am} \leqslant \Delta z_{f/r} \leqslant z_{ap}, \\ c_{f/r,0} \cdot \left(1 + \left[\frac{\Delta z_{f/r} - z_{am}}{z_{dm} - z_{am}}\right]^2\right) & \Delta z_{f/r} < z_{am}, \\ c_{f/r,0} \cdot \left(1 + \left[\frac{\Delta z_{f/r} - z_{ap}}{z_{dp} - z_{ap}}\right]^2\right) & \Delta z_{f/r} > z_{ap}. \end{cases} \tag{3.62}$$

If $\Delta z_{f/r} < z_{am}$ or $\Delta z_{f/r} > z_{ap}$ the constant spring rate $c_{f/r,0}$ is extended by a quadratic function, leading to a progressive characteristic when moving past z_{am} or z_{ap}. At z_{dm} and z_{dp} the spring constant $c_{s,f/r}$ is equal to $2 \cdot c_{f/r,0}$. Since symmetric behavior is assumed $z_{am} = -z_{ap}$ and $z_{dm} = -z_{dp}$.

For the damper coefficient $d_{f/r}$ a degressive model was chosen (compare [48]):

$$d_{f/r} = \begin{cases} \frac{d_{f/r,0}}{1 + p_c \cdot \Delta \dot{z}_{f/r}} & \Delta \dot{z}_{f/r} \geqslant 0, \\ \frac{d_{f/r,0}}{1 - p_r \cdot \Delta \dot{z}_{f/r}} & \Delta \dot{z}_{f/r} < 0. \end{cases} \tag{3.63}$$

The degression at compression ($\Delta \dot{z}_{f/r} \geq 0$) and at rebound ($\Delta \dot{z}_{f/r} < 0$) is given by p_c and p_r. Besides the spring characteristics also the damper characteristics are implemented as symmetric ($p_c = p_r$). At low damper velocities ($\Delta \dot{z}_{f/r} \longrightarrow 0$) the damper coefficient is defined by $d_{f/r,0}$. The spring-damper model is shown in Figure 3.15.

3.1.10 Driver

The driver is modelled as a combination of a PI controller and an inverse feedforward vehicle model. The PI controller relies on the difference between the calculated vehicle speed v_x and the predefined driving cycle speed v_c. The controller is split into two branches in order to allow an individual tuning of the controller's parameters for the cases $v_x \geq v_c$ and $v_x < v_c$. Depending on the values of v_x and v_c, the controller then determines the correspondent driver pedal position. Even though the parameters are adapted to the real world driving cycle, the PI controller alone can not sense speed deviations between v_x and v_c with the requested rapidity. Therefore, a feedforward model is included in the calculation of the driver's pedal position. This model takes the vehicle speed v_x and acceleration a as inputs and determines the force acting on the tires under consideration of the rolling resistance force F_r, the air drag F_d, the climbing resistance F_g, the acceleration resistance F_a, the inertias of the drivetrain components (Θ_T, Θ_{EMG}) and the gear ratios of the final drive i_{FD} and summation gear i_{SGR}. The resulting driver pedal position is then forwarded to a rate limiter to account for the finite alteration time of the real vehicle's pedals due to human motion. In Section 4.1 it can be seen that the model reflects the real vehicle's behavior with good accuracy.

3.2 Development of an Operation Strategy

3.2.1 Quasistatic Pedal Map

The HEV investigated in this thesis uses a rulebased OS which was determined by load variation manoeuvres. A static pedal map was generated by driving with constant pedal position. In order to allow a detection of hysteresis between increasing and decreasing pedal positions, the static map was extended to a quasistatic one. Whereas the increasing pedal map is used for positive pedal position rates, the decreasing pedal map is used for negative pedal rates. As sharp borders between the operation modes would cause frequent mode shifts, a hysteresis is included which separates mode shifts with decreasing pedal position from the shifts with increasing pedal position. Figure 3.16 shows the quasistatic pedal map for high SOC and Figure 3.17 for low SOC. The main operation mode is series mode which is denoted by the yellow area. The dark blue and light blue zones stand for electric drive and recuperation mode, respectively. The brown area indicates combined operation, meaning that the ICE and EM contribute to the traction force which is achieved by engaging the clutch.

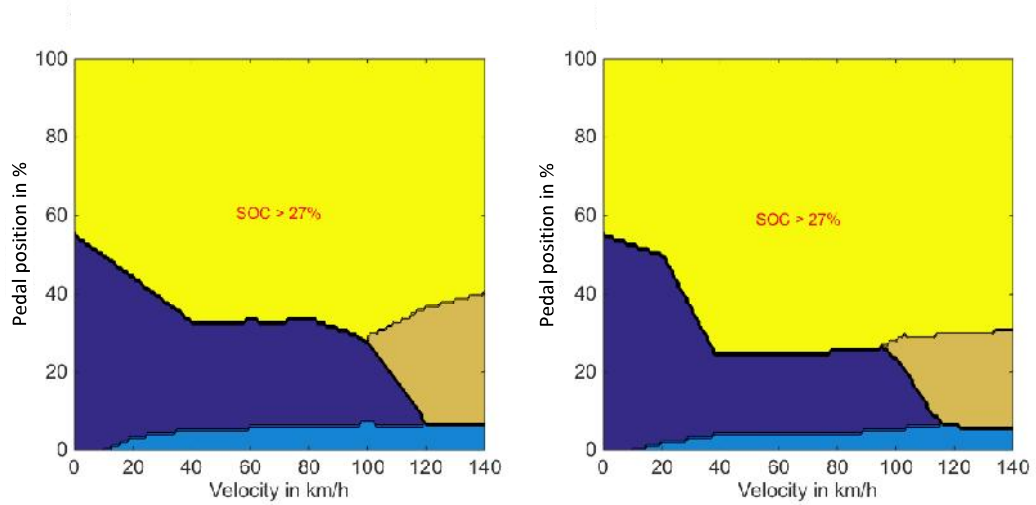

Figure 3.16: Implemented operation strategy with increasing (left) and decreasing (right) pedal position rates at high SOC level [50]

3.2.2 Braking and Recuperation Strategy

Besides the operation modes, the OS also controls the braking behavior. As HEVs have the possiblity of recuperating energy during vehicle deceleration phases, it needs to be determined to which extent the traction motor supports the friction brakes. In order to obtain a map of the recuperation torque, several braking manoeuvres were conducted.

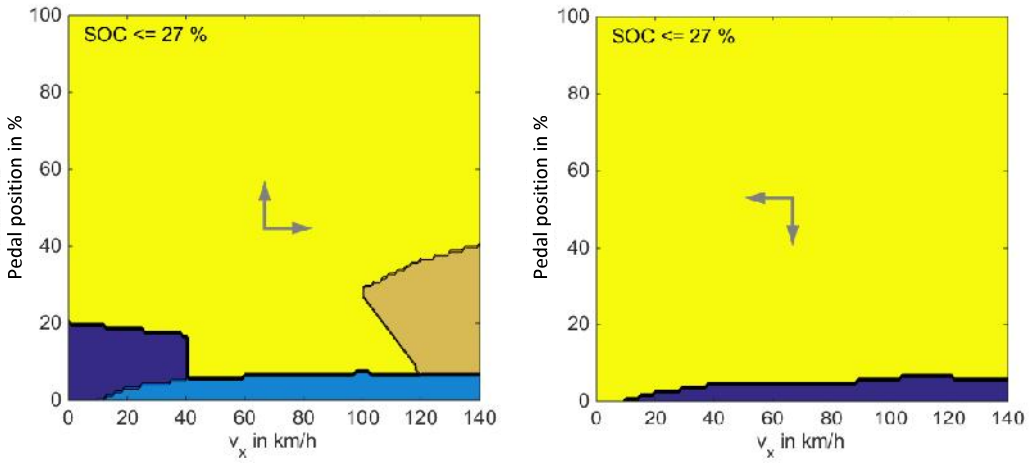

Figure 3.17: Implemented operation strategy with increasing (left) and decreasing (right) pedal positions at low SOC level [50]

The results are shown in Figure 3.18. The braking torque (which is equal to the effective torque at the drive axle) is a function of the engine speed and therefore of the vehicle speed. For speeds lower than 50 km/h the recuperation torque is constant, whereas it is then limited by the maximum recuperation torque. The total requested braking torque is denoted by the cyan lines and the recuperation torque of the EMG is shown in blue. The energy dissipated by the friction brakes can be calculated by subtracting the recuperation torque from the total requested braking torque.

3.2.3 Component Controller Units (CCUs)

The maps described in Sections 3.2.1 and 3.2.2 do not consider the dynamic behavior of the drivetrain components and therefore do not depict the transient real vehicle behavior. The expedient approach therefore is to extend the quasistatic maps with a dynamic OS relying on the behavior of the drivetrain components and their limits by implementing component controller units. The CCUs ensure that every part of the drivetrain operates within its thermal, mechanical and electrical limits. As the battery of a HEV is the most critical component in terms of longevity, the OS needs to ensure that its limits are not exceeded under any circumstances.
Mechanical limits are set by implementing torque maps as a function of the rotational speed and pedal position as described in Section 3.1. From the requested mechanical power the needed electrical power can be calculated for each timestep. In Table 3.1 the power limitations for the battery and the EM are described. It can be seen that the maximum power request cannot be covered solely by the battery which makes it necessary

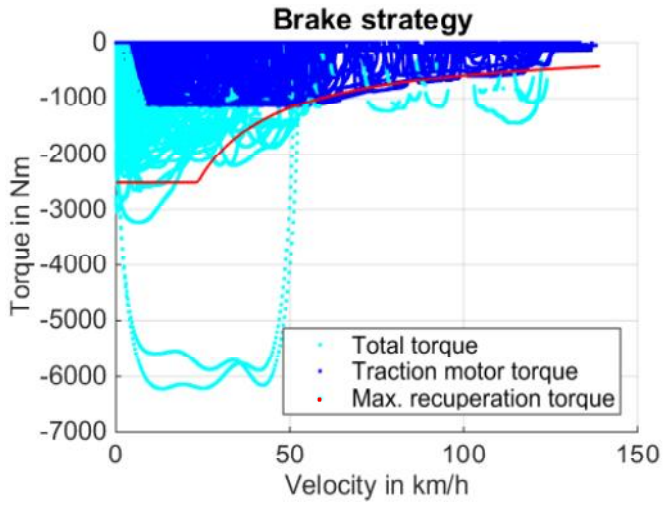

Figure 3.18: Results of the braking strategy evaluation [50]

to have the ICE provide additional power. As the ICE cannot immediately deliver power due to its finite startup time, an engine starting routine has to be implemented to ensure that the maximum power is available without any delay or battery overstrain. This is achieved by using the Simulink stateflow environment. A schematic representation of the states and transition conditions (TC) is given in Figure 3.19. In order to enable a transition from one state to the other, the corresponding transition condition has to be triggered. The TCs are given by the current and power constraints of the battery (which also affect the EM power P_{EM} and current I_{EM}) and the ICE idle speed ω_{idle}. The notation && indicates that if the condition to the left of the operand is false, the one to the right does not have to be evaluated, which reduces computation time. The use of || also decreases the computation effort by evaluating the condition on the right side of the operand only if the condition on the left is false. In Equation (3.64) the implementation of a kickdown switch based on the pedal position p_{EM} is shown. The threshold values used in the transition conditions account for the ICE startup time and the battery's limitations and were determined empirically by investigation of different driving manoeuvres. Whereas the startup of the ICE is triggered, when the EM current and power exceed threshold values related to the discharging constraints of the battery (compare Equation (3.64)), it needs to be ensured that the ICE is not switched off due to dynamic fluctuations caused by the drivetrain controllers. Consequently, a hysteresis for the ICE state is implemented which is entered when the discharging constraints are below a certain threshold (Equation (3.66)) and can only be left, when the discharging of the battery increases (Equation (3.68)), otherwise the ICE is switched off if after 1 second the transition conditions specified in Equation (3.69) are true. Equation (3.67) is triggered, if the ICE would cause an overcharging of the battery. As overcharging harms the longevity of the battery, the transition directly leads to an ICE off state without consideration of any hysteresis.

Table 3.1: Component Restrictions

Component Restriction	**Numeric Value**
Maximum battery charging power $P_{lim,chg}$	-50kW
Maximum battery discharging power $P_{lim,dchg}$	80kW
Maximum battery charging current $I_{lim,chg}$	-148A
Maximum battery discharging current $I_{lim,dchg}$	300A
$\mathrm{SOC}_{\mathrm{min}}$	0.3
$\mathrm{SOC}_{\mathrm{max}}$	0.95
Maximum EM power (traction)	124kW

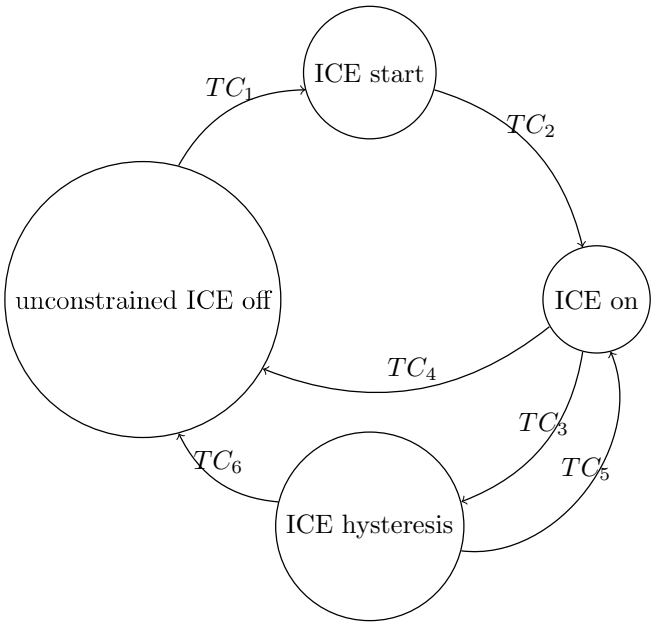

Figure 3.19: ICE startup routine

$$TC_1 = \begin{cases} (P_{EM} > P_{lim,dchg} - 30000 \;\&\&\; P_{Bat} > P_{lim,chg} + 5000 \;\&\&\; I_{Bat} > I_{lim,chg} + 10) \| \\ (I_{EM} > I_{lim,dchg} - 50 \;\&\&\; P_{Bat} > P_{lim,chg} + 5000 \;\&\&\; I_{Bat} > I_{lim,chg} + 10) \| \\ (p_{EM} > p_{kickdown} \;\&\&\; P_{Bat} > P_{lim,chg} + 5000 \;\&\&\; I_{Bat} > I_{lim,chg} + 10) \end{cases} \tag{3.64}$$

$$TC_2 = \omega_{ICE} \geq \omega_{idle} \tag{3.65}$$

$$TC_3 = P_{EM} < P_{lim,dchg} - 30000 \;\&\&\; I_{EM} < I_{lim,dchg} - 50 \tag{3.66}$$

$$TC_4 = P_{Bat} < P_{lim,chg} \;||\; I_{Bat} < I_{lim,chg} \tag{3.67}$$

$$TC_5 = P_{EM} > P_{lim,dchg} - 20000 \;\&\&\; I_{EM} > I_{lim,dchg} - 40 \tag{3.68}$$

$$TC_6 = \begin{cases} ((P_{EM} < P_{lim,dchg} - 30000 \;\&\&\; I_{EM} < I_{lim,dchg} - 50 \\ \&\&\; p_{driver} < 0) \;\&\&\; \text{after(1,sec))}|| \\ (P_{Bat} < P_{lim,chg} + 5000)||(I_{Bat} < I_{lim,chg} + 10) \end{cases} \tag{3.69}$$

To start the ICE, conventional drivetrain layouts use an alternator. HEVs use the EMG coupled to the ICE to perform this task. To achieve this, the EMG works as a motor providing power for the ICE startup. Figure 3.20 depicts the EMG torque for the startup procedure. As soon as the ICE reaches ω_{tow} the fuel injection starts and the ICE produces torque as shown in Figure 3.21. The EMG then works in generator mode and forwards the energy to the battery.

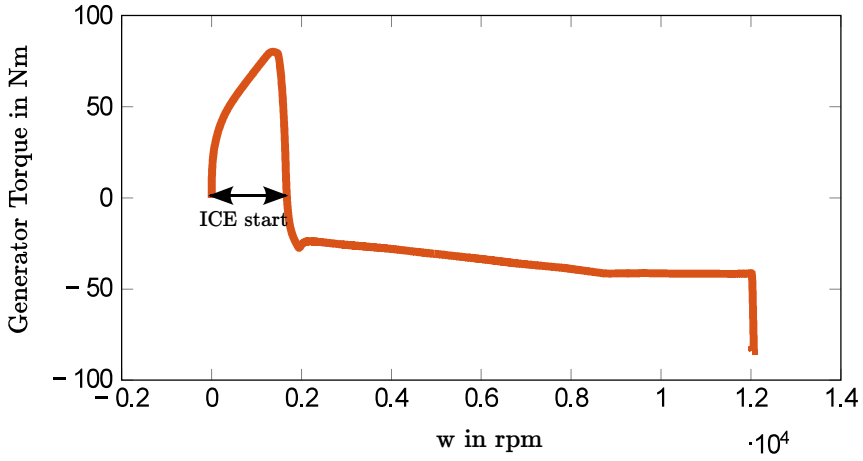

Figure 3.20: EG torque during ICE startup

In the simulation, the torque at ω_{tow} is assumed to be equal to the torque at idle speed. A comparison of the starting behavior of the real vehicle and the simulation model can be found in Section 4.1. In [34] two different types of starting the ICE are explained: For the *slipping* start, the ignition is only activated when the ICE rotational speed is equal to the angular speed of the connected gearbox shaft. A *tear* start is performed when the ignition is triggered as soon as the crankshaft rotates. The start procedure used in the investigated model is not clearly relatable to one of the two types, but similar to the tear start procedure. When turning the ICE off, the EMG recuperates the energy provided by the ICE until it reaches standstill and charges the battery. For high and low SOC states close to the SOC boundaries of SOC_{min} and SOC_{max}, the behavior of the ICE

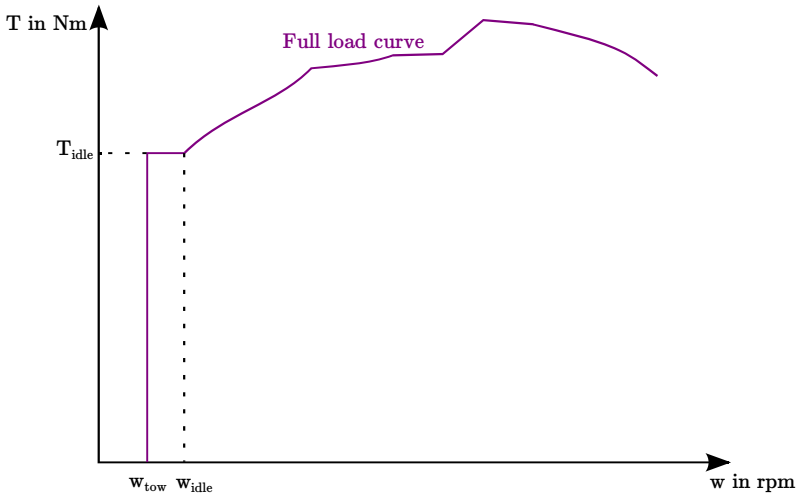

Figure 3.21: ICE torque

needs to be modified. If the battery cannot provide any more propulsion power, the ICE needs to be permanently switched on whereas it cannot be operating if the SOC exceeds the maximum allowed value. These dependencies are modelled with a similar stateflow to the one depicted in Figure 3.19. Thermal constraints are imposed by a temperature dependent battery model which calculates the battery temperature under consideration of the thermal capacity of the body and the thermal resistance of the wall. This results in a temperature dependent inner resistance R_i (compare Equation (3.15)) influencing the battery power output.

3.3 Driveability Controller Development

As mentioned at the beginning, current research is mainly focusing on energy management topics of HEVs. Yet, driveability is not less important as it is a key decisive factor for the marketability of a vehicle. This is because the final decision to buy a car is mostly made after a test drive. Therefore, HEVs need not only focus on reducing emissions but also on improved pedal response and oscillations of the engine speed as these are important driveability criteria (compare Section 2.3). This is especially important for series and parallel-series hybrid architectures as they allow the engine speed to be decoupled from the vehicle speed, making it possible to operate the ICE at maximum fuel efficiency. This property can be regarded as a continuously variable transmission and is called electro-mechanical CVT. While the eCVT offers great fuel saving potential it also needs to be considered that it decouples the driver input (accelerator pedal) from the engine speed, resulting in an undesirable feeling of being disconnected with the powertrain. In order to cope with the possible decoupled engine speed a relationship between vehicle speed and engine speed is introduced, compare Figure 3.22. Such a relation can be expressed in a tabular form. A piecewise linear characteristic was chosen. This is due to the fact that a linear characteristic corresponds with the human assumption of a linear relation between control variable and resulting effect [10]. Figure 3.22 shows that the implemented relation is also a function of the driving style. The methods used for driving style classification will therefore be discussed in the following whereas Figure 3.22 will be further discussed under *Implemented engine speed relation and pedal characteristic*.

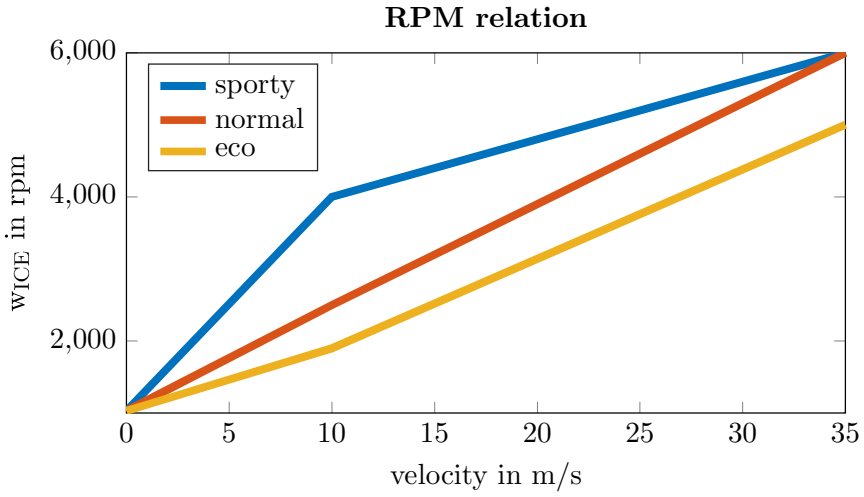

Figure 3.22: Relation between vehicle speed and engine speed

3.3.1 Driving Style Classification

Another important aspect of driveability is the possibility of giving the vehicle a specific character, while simultaneously ensuring that driving comfort, driving safety and driving pleasure are held at a very high level. This methodology leads to a completely new human-vehicle interaction as the vehicle owner is able to form a mass produced vehicle according to his demands. Thus, the loss of identification between owner and product can be avoided [35]. A driving style classifier does not only allow to individually refine the vehicle character, it is also an important input for the parametrization of advanced driver assistance systems. It allows the accelerations chosen by a cruise control system to be adapted to the desired accelerations of the driver [13]. Furthermore, the driving style also plays an important role for the energy management, since greater power demands require an adaptation of the operating strategy in order to maintain optimal SOC level. Due to the aforementioned synergies between adaptive and predictive tasks, it comes useful to take a glance at model predictive control solutions when it comes to the choice of the adaptation strategy. In the following fuzzy logic systems and artificial neural networks will be presented.

Fuzzy Logic
Fuzzy logic allows the representation of complex input-output relations as a synthesis of multiple simple input-output relations, which are called fuzzy rules. The boundaries of these rules are not sharp, but "fuzzy". Whereas boolean logic only allows to determine if a statement is true or false (e.g. driver=sporty=true, driver=normal=false), fuzzy logic is more refined and allows classifications of the type driver=60 % sporty and 40 % normal. According to [5] the following stages are executed in order to process an output of a fuzzy system for a given input:

- Fuzzification: Map any input to a degree of membership in one or more membership functions.
- Fuzzy inference: Fuzzy inference is the calculation of the fuzzy output.
- Defuzzification: Defuzzification converts the fuzzy output to a crisp output.

The aforementioned three stages differ for each type of fuzzy model (compare [57]):

- Mamdani models link a fuzzy variable to a fuzzy number, e.g. y_F=big, y_F=small, which allows rather intuitive description of qualitative knowledge.
- TSK Models (Tagaki, Sugeno, Kang) describe a fuzzy variable as linear combination of weighted input variables: $y_F = a_0 + \sum a_i x_i$, whereas a_i denotes a constant and x_i the input variable. These systems may lack in the transparency of rules, but offer increased system performance.

Artificial Neural Networks
Artificial neural networks can be considered as a biological approach, since they are simple abstractions of biological neurons. A biological neuron consists of a cell body, a dendrite, and an axon (Figure 3.23). The connections between the axons of one cell

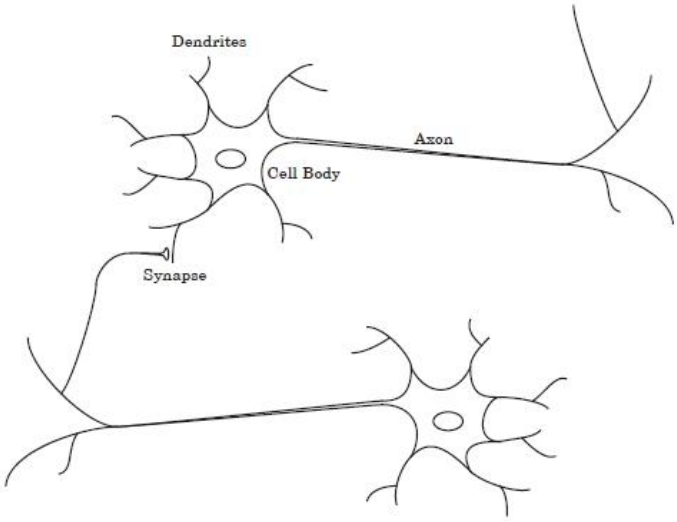

Figure 3.23: Biological neuron [20]

and the dendrite of another cell are called synapses. Electric pulses coming from other neurons are translated into chemical information at each synapse and transferred to the cell body. An electric pulse is generated if the sum of the inputs exceeds a certain threshold [57], [20].

This biological model can be represented by a mathematical approach which is shown in Figure 3.24. The cell body is represented by the summation and the transfer function f_t, the output o is equal to the signal on the axon and n_w can be interpreted as the strength of the synapse. The neuron output o is calculated as follows: at first the input i_p is multiplied with the weight n_w which results in $n_w \cdot i_p$. At the sum $n_w \cdot i_p$ and the bias b are connected and forwarded to the transfer function f_t, which produces the output o. Whereas the transfer function is specified a-priori by the designer of the ANN, the parameters n_w and b are adjustable and can be modified by training the neural network. Training can also be referred to as learning. Depending on the applied learning rule, supervised learning, unsupervised learning and reinforcement learning can be distinguished [20].
In Table 3.2 fuzzy logic systems and neural networks are compared regarding online adaptation, accuracy, repeatability, computation time and the number of input variables. Since neural networks require a lot of training data to ensure proper functionality a fuzzy system will be chosen to perform the classification tasks. The property of fixed rules comes useful in classification, but makes an adaption to modified inputs difficult. In terms of handling multiple input variables, fuzzy logic has drawbacks in comparison to ANNs.

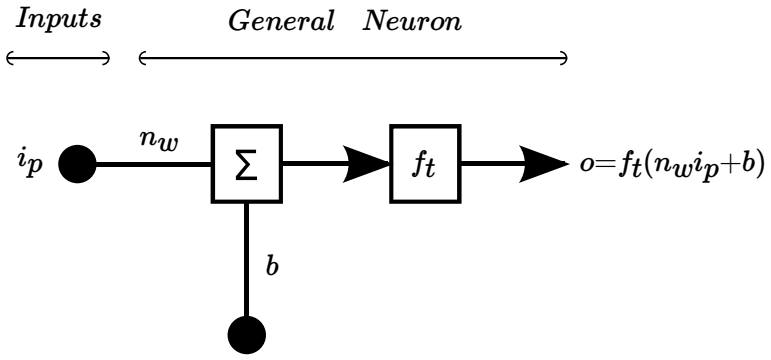

Figure 3.24: Single input neuron [20]

Table 3.2: Comparision fuzzy logic and artificial neuronal networks

	Fuzzy Logic	Neuronal Networks
Online Adaptation	Rigid rules	Continuously updateable
Computation Time	Real time	Longer processing times
Accuracy	Good, but sensitive to data	Good representation of complex behaviours
Repeatability	Yes, fixed rules	If no learning occurs: same output for same input
Number of input variables	$\leq$3 because of complexity	$\leq$5, as training becomes more difficult

3.3.2 Implementation of the Classifier

Before designing the actual classifier a few general conditions need to be defined:

- Since the Simulink model delivers noisy data, a moving average filter with a window length of two seconds needs to be applied to the signals used for classification
- Driving style does not change rapidly, therefore it will be evaluated every 60 seconds, for the first 60 seconds a default value will be used
- For classification a time window of 180 seconds of data is used, since recent data should have higher impact on the driving style, the data used for classification needs to be weighted according to the weight function from [61] depicted in Figure 3.25.

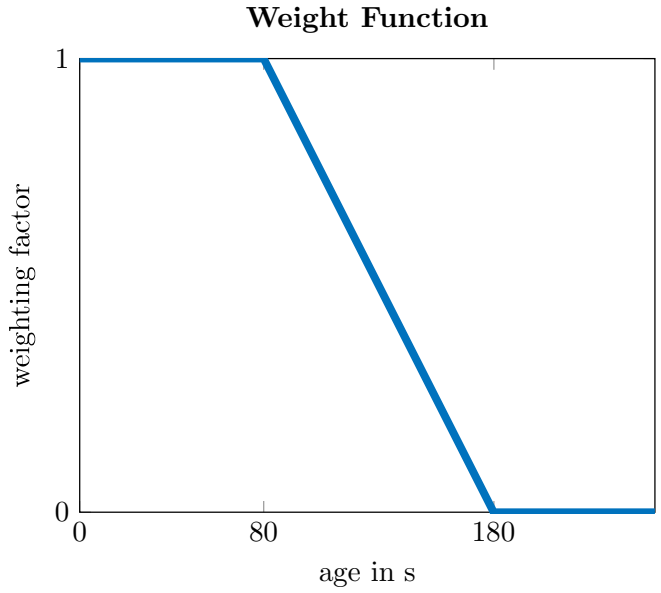

Figure 3.25: Weight function

The classification of the driving behavior can be done in two ways: either by evaluating acceleration and jerk signals ([16], [40]) or via pedal signals [61]. The approach used here was to take acceleration signals as an outline for the classifier design and step by step refining the algorithm by incorporating other signals.

In the following the basic classifier, which considers only the absolute value of the acceleration signals will be presented: After filtering and weighting the absolute value of the acceleration signals with the methods described on top of this page, the maximum value of the acceleration is forwarded to a sugeno type fuzzy logic system. Next, a degree of membership is calculated in compliance with the a-priori defined membership functions shown in Figure 3.26.

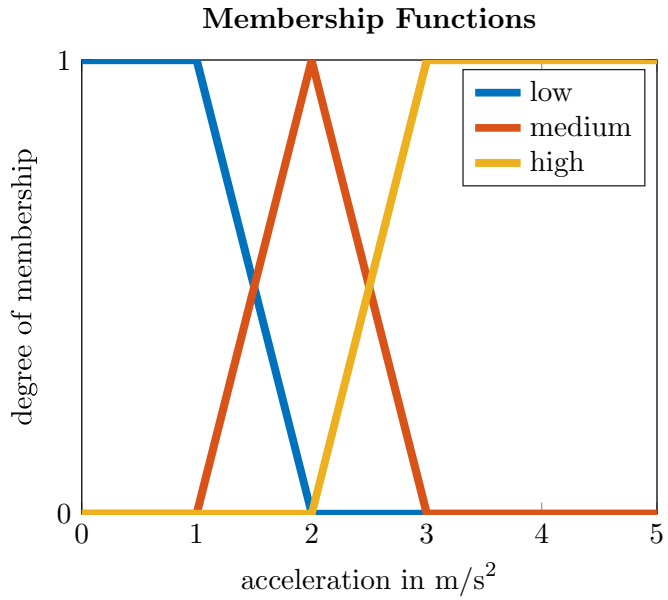

Figure 3.26: Membership functions acceleration

Then, the fuzzy output is calculated using fuzzy rules and later defuzzified. The rules used here are adapted from [5]:

1. If acceleration is low, then driving style is low
2. If acceleration is medium, then driving style is medium
3. If acceleration is high, then driving style is high

All rules are weighted with one, since no acceleration region (low, medium, high) should be favoured. The output of the fuzzy logic system is the driving style which can be interpreted as follows:

- Eco: driving style=0
- Normal: driving style=0.5
- Sporty: driving style=1

As the fuzzy system produces a continuous output between 0 and 1, linear interpolation is performed between the curves depicted in Figure 3.22. This is because deposing only 3 driving styles in the OS would result in abrupt changes in the vehicle behavior when switching between sporty and normal drivers for example. Due to the linear interpolation the vehicle behavior is adapted smoothly.

For a better understanding of the illustrated processes, the output of the fuzzy system for a given input will be depicted.

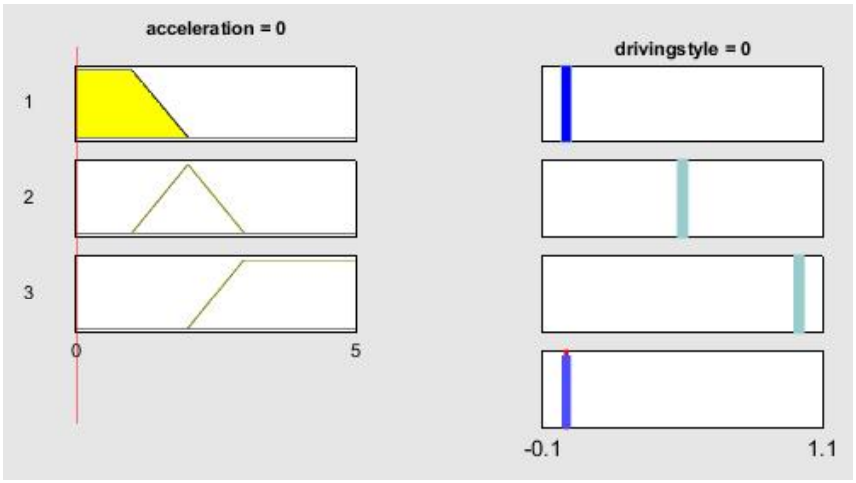

Input-Output Relation for a= 0 m/s²

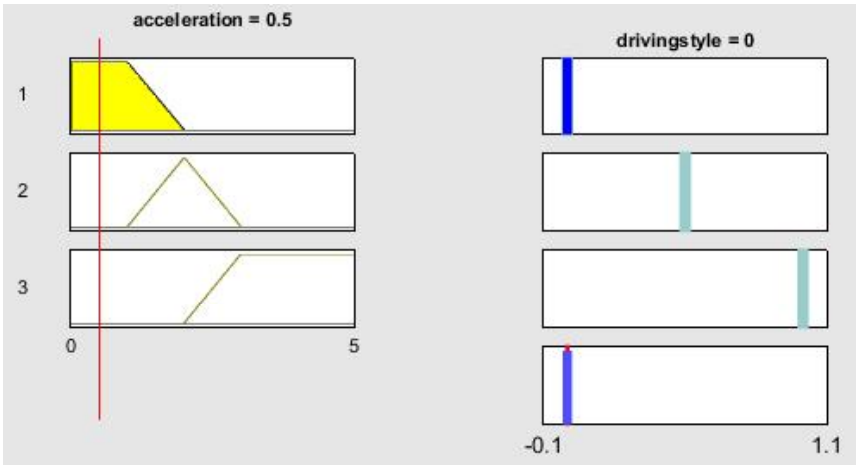

Input-Output Relation for a= 0.5 m/s²

Figure 3.27: Input-output relation for different accelerations

Whereas in Figures 3.27, 3.29(top) and 3.30 only one membership function is triggered, Figures 3.28(bottom) and 3.29(bottom) show cases where the so-called fuzziness comes to play: the border between two membership functions is not sharp, but fuzzy. Figures 3.28(bottom) and 3.29(bottom) also show that different rule weights could cause a favouritism of a specific membership function, which is unwanted in this case.

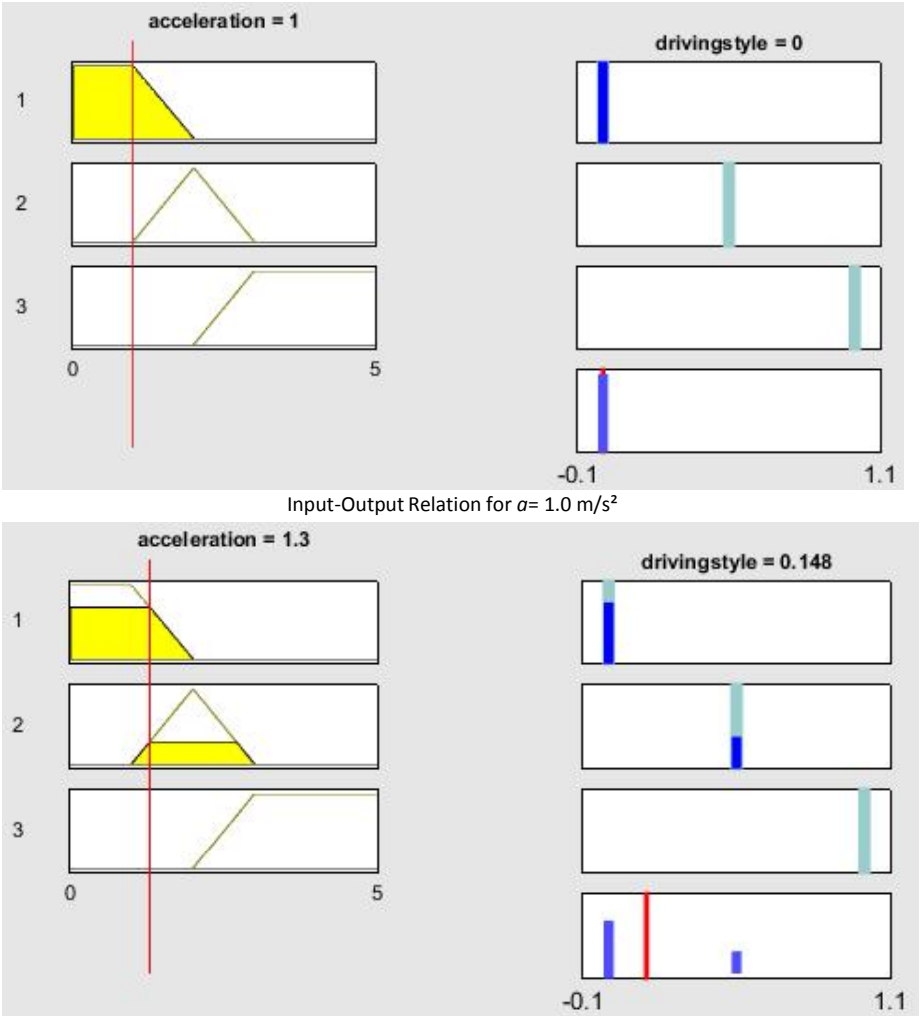

Figure 3.28: Input-output relation for different accelerations

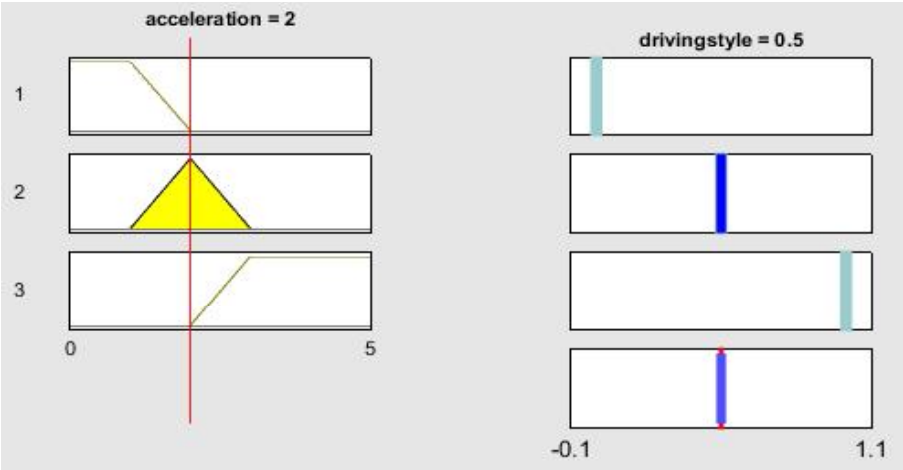

Input-Output Relation for a= 2.0 m/s²

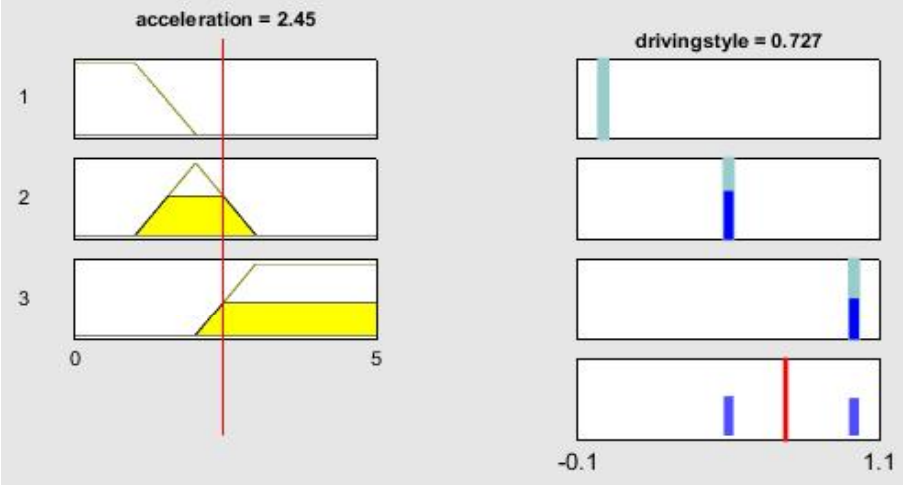

Input-Output Relation for a= 2.45 m/s²

Figure 3.29: Input-output relation for different accelerations

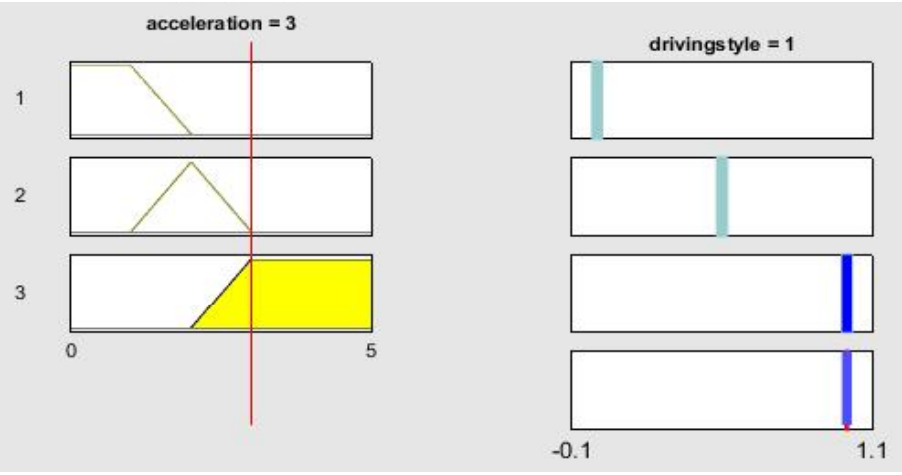

Input-Output Relation for a= 3.0 m/s²

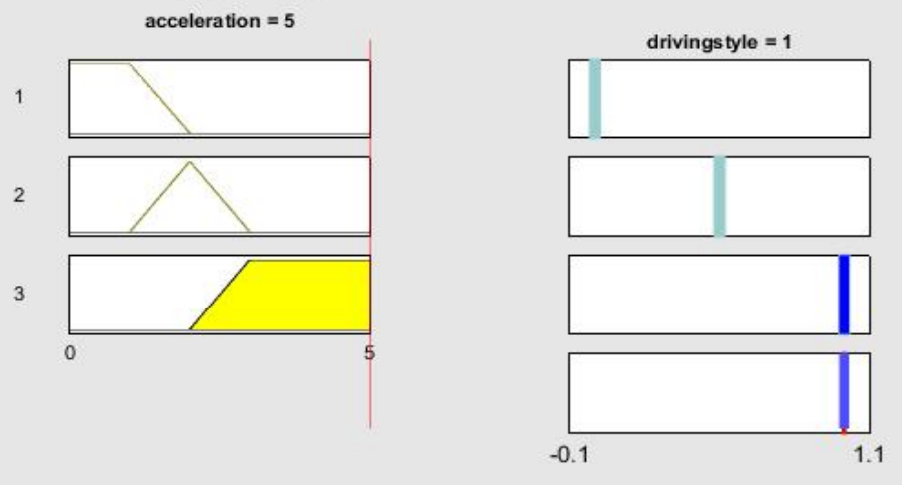

Input-Output Relation for a= 5.0 m/s²

Figure 3.30: Input-output relation for different accelerations

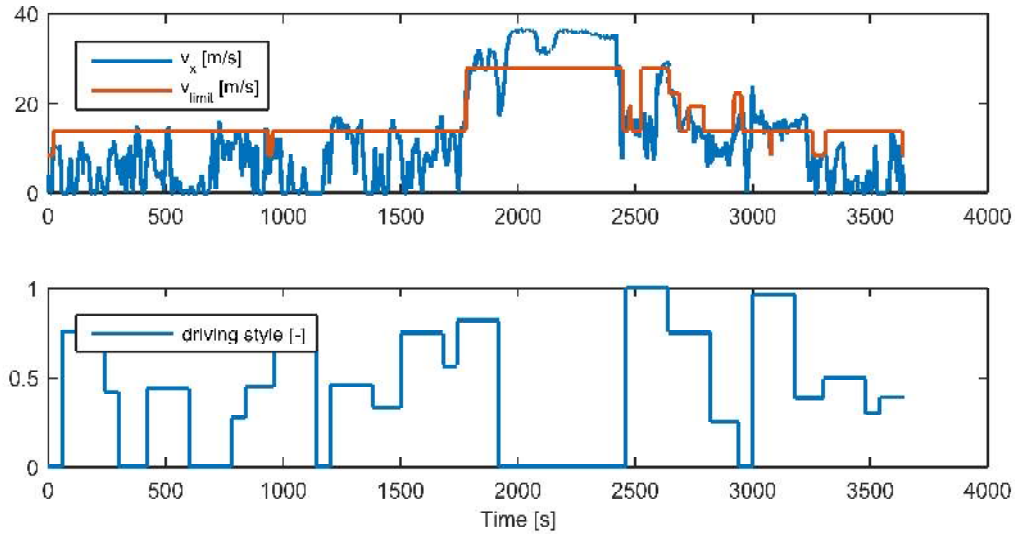

Figure 3.31: Results of the acceleration based classification

Figure 3.31 shows the results obtained by the acceleration based classification. Abrupt changes in driving style can be witnessed which do not correspond with realistic driving behavior. Therefore, a second variable for classification was added, namely the excess of the speed limit defined as follows:

$$v_{excess} = v - v_{limit} \tag{3.70}$$

This equation is only evaluated if $v > 0.3\,\mathrm{m/s}$. For this variable membership functions were defined by using empirical values, which can be learned from Figure 3.32.

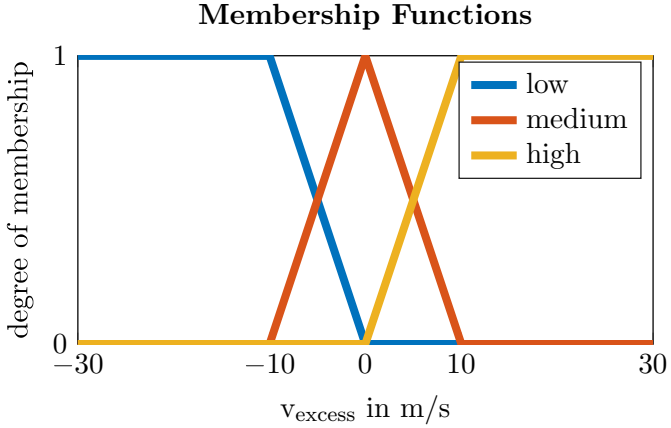

Figure 3.32: Membership functions v_{excess} in m/s

For the combined classification the following distinction was chosen:

- If the maximum of the filtered and weighted acceleration values is equal to $1.5\,\mathrm{m/s^2}$ or exceeds this barrier, an acceleration based classification will be performed
- Otherwise a v_{excess} based classification will be performed

The threshold value of $1.5\,\mathrm{m/s^2}$ was chosen as for driving scenarios which do not include start or stop manoeuvres the acceleration stays about or beyond this level for all driving styles [5]. It needs to be added that no signals are lost when switching between these two types, assuring that for every classification task the full time window of acceleration and v_{excess} related data is available. The consideration of two input variables for classification leads to an increase in accuracy, as the abrupt changes in driving style are reduced. But it needs to be stated that the excess of the speed limit as an absolute deviation does not consider that a speed deviation of $10\,\mathrm{m/s}$ in a rural area is much more critical than on the motorway for example. Therefore, this input is be modified according to Equation (3.71), in order to obtain the relative deviation as an input.

$$v_{excess,rel} = \frac{\Delta v}{v_{limit}} = \frac{v - v_{limit}}{v_{limit}} \tag{3.71}$$

For further improvements it is also necessary to make a distinction between acceleration and deceleration phases. Therefore, the algebraic sign is included in the input variable acceleration and the membership functions for low, medium and high acceleration are extended to negative values for the consideration of deceleration phases. The refined membership function for the vehicle acceleration is depicted in Figure 3.33.

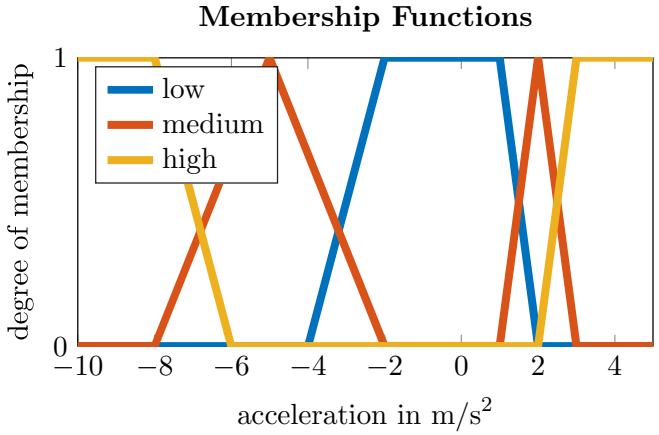

Figure 3.33: Refined membership functions acceleration

It can be seen, that the acceleration value reached in deceleration phases is greater than the value for acceleration. This is a result of the vehicle's braking power being much greater than the EM's traction power. The acceleration boundaries were calculated by transforming the maximum traction and braking torque into a force acting on the

wheels and then calculating the corresponding acceleration by applying the equation of motion. Figure 3.34 shows the membership function for the input variable $v_{excess,rel}$. The threshold values were determined empirically under consideration of the most common speed limits (rural area, country road and highway).

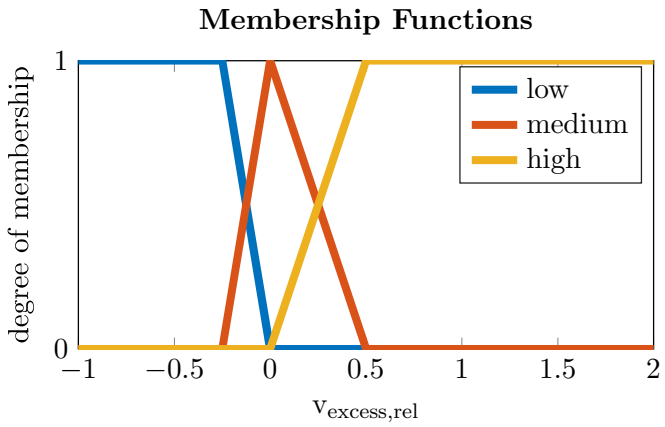

Figure 3.34: Membership functions $v_{excess,rel}$

The results of the combined classification can be seen in Figure 3.35. By using two input variables, the fluctuations of the basic classification depicted in Figure 3.31 could be reduced.

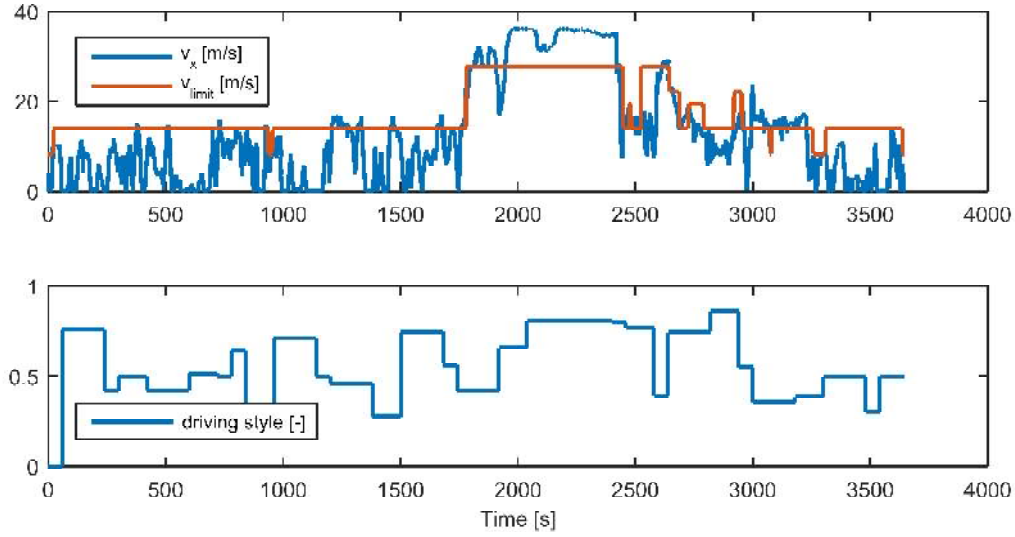

Figure 3.35: Results refined classification

Further improvements could be achieved by incorporating pedal signals such as the brake pedal actuating frequency into the classification process. Also it could be useful implement other acceleration related inputs such as the lateral acceleration a_y for example. However, in this thesis, driving style classification is only performed by using the acceleration a and the relative velocity deviation $v_{excess,rel}$.

Implemented engine speed relation and pedal characteristics

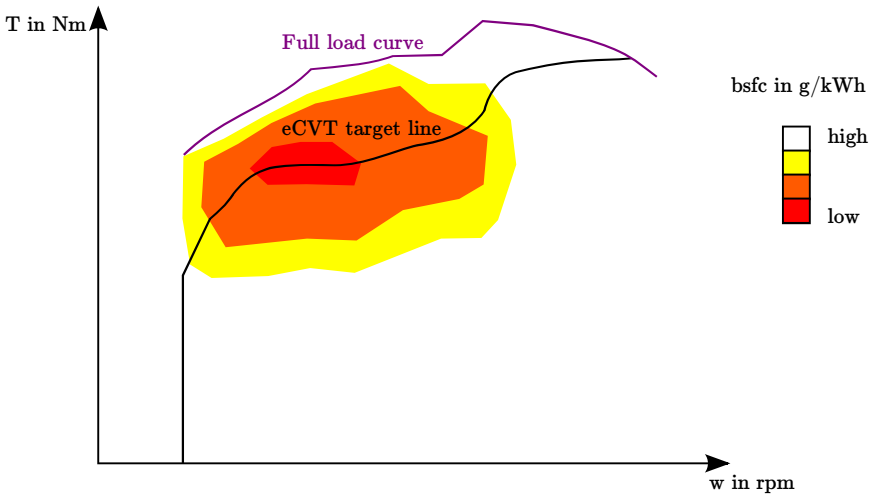

Figure 3.36: ECVT target line

In order to retain good fuel economy, the ICE characteristic is still bound to the eCVT target line which is depicted in Figure 3.36. It can be seen, that along the eCVT target line the ICE's fuel consumption is minimal. The actual reconnection of the driver with the drivetrain is performed via intelligent generator control. A driver dependent engine speed relation (see Figure 3.22) delivers an engine target speed based on the current velocity. The actual engine speed and the target engine speed are subtracted and then forwarded to a proportional generator controller. The output of the controller is the EG pedal position p_{EG} which is proportional to the controller's amplification factor K_p and the speed difference $\Delta\omega_{ICE}$:

$$p_{EG} = K_p \cdot \Delta\omega_{ICE} \tag{3.72}$$

This ensures, that the EG delivers power only if the actual speed is beyond the target speed. This allows the ICE to operate at the best efficiency points while having the engine speed be a function of the vehicle speed.

Comparing Figures 3.36 and 3.22 the following statements can be made for the different driving styles:

- ECO:
  - The engine operates from 1900 to 3000 rpm at speeds of 10 to 20 m/s assuring best fuel economy in rural areas while reconnecting the driver with the drivetrain
  - For the motorway (35 m/s) the engine is set to operate at 5000 rpm, delivering a high amount of power and torque without corrupting fuel efficiency
- NORMAL:
  - Straight linear rpm relation throughout the whole speed range
  - For speeds under 20 m/s the BSFC does not exceed 233 g/kWh
  - Excellent power delivery for high speeds (around 100 kW @6000 rpm)
- SPORTY:
  - Steep inclination of the engine rpm for fast power delivery without exceeding 233 g/kWh at 10 m/s
  - Having reached 4000 rpm the inclination of the engine torque in the eCVT target line can be used for fast acceleration
  - Excellent power delivery for high speeds (around 100 kW @6000 rpm)

For further improvement of the vehicle response, a driver dependent accelerator pedal characteristic was implemented. This approach can be compared to the "pedalbox" strategy used to define the character of a vehicle [9]. While the pedal characteristic is left unchanged for eco drivers, sporty drivers benefit from an amplification factor of 1.2 to 1.5. The rise at 3860 rpm targets on compensating the decreasing EM torque at this speed (see Figures 3.37 and 3.38), whereas the amplification factors were determined empirically by investigating specific driving manoeuvres. The EM characteristic depicted in Figure 3.38 is a piecewise linear approximation of the real EM characteristic.

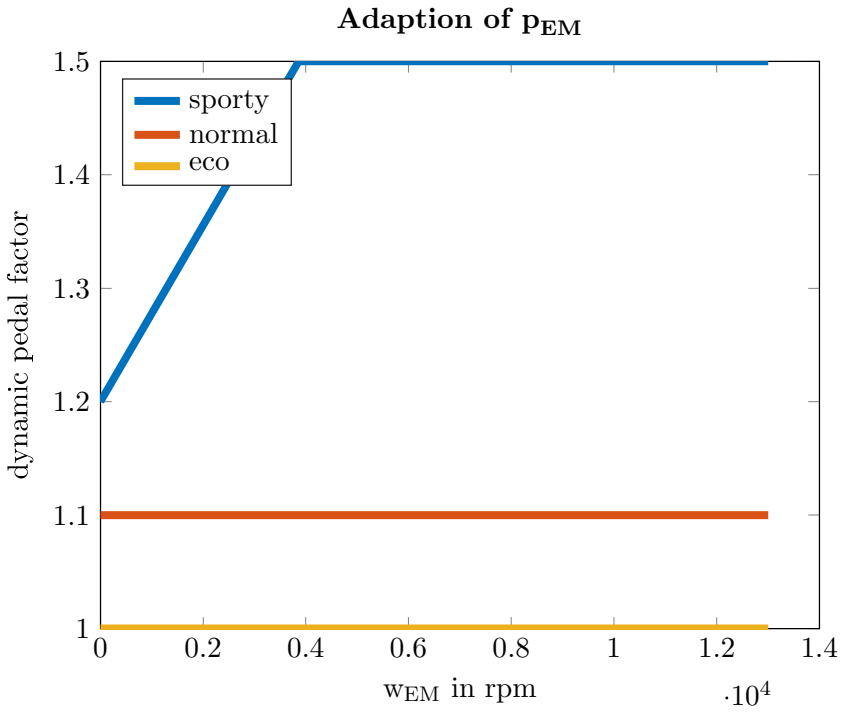

Figure 3.37: Pedal response adpation

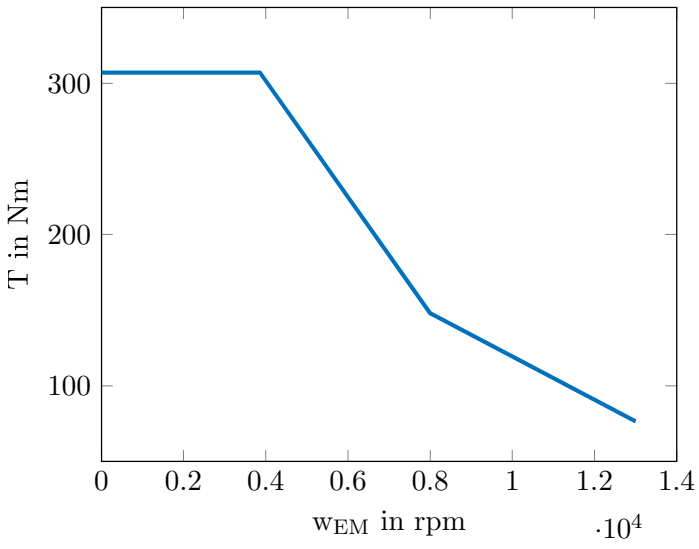

Figure 3.38: EM characteristics

Besides performing a pedal response adaption for p_{EM}, driveability can also be enhanced by including a feedforward control module in the calculation of p_{EM}. This allows to prevent unexpected hesitations in acceleration as depicted in Figure 3.39. It can be seen that the initial layout (blue line) shows a bend in the p_{EM} progression which occurs when triggering one of the battery constraints. The feedforward layout (green line) may result in a less steep p_{EM} progression, however no power drop occurs which results in a predictable acceleration behavior. The controller uses the requested torque T_{req} and the EM angular speed ω_{EM} to calculate the electrical power needed at the EM:

$$P_{EM,el} = \frac{T_{req} \cdot \omega_{EM}}{\eta_{EM}} \tag{3.73}$$

By dividing $P_{EM,el}$ and U_{Bat}, the required EM current I_{req} can be calculated:

$$I_{req} = \frac{P_{EM,el}}{U_{Bat}} \tag{3.74}$$

The available power at the EG $P_{EG,el}$ is calculated by multiplying the battery voltage U_{Bat} and the EG current I_{EG}:

$$P_{EG,el} = I_{EG} \cdot U_{Bat} \tag{3.75}$$

The resuling battery power and current are then calculated according to Equations (3.76) and (3.77).

$$P_{Bat} = P_{EM,el} + P_{EG,el} \tag{3.76}$$

$$I_{Bat} = I_{EG} + I_{req} \tag{3.77}$$

If the battery power or current do not trigger any of the battery's restrictions, no alternation of p_{EM} is necessary. If a restriction is triggered, the allowed torque T_c is calculated based on the triggered restriction. In the following Equation this procedure will be explained for discharging constraints. Charging constraints are handled similarly. Due to the sign change, the minimum in Equation (3.78) needs to be replaced by maximum.

$$\begin{aligned} P_c &= \min(P_{Bat}, P_{lim,dchg}) \\ I_c &= \min(I_{Bat}, I_{lim,dchg}) \\ T_1 &= \frac{P_c}{(\omega_{EM} + 1)} \cdot \eta_{EM} \\ T_2 &= \frac{U_{Bat} \cdot I_c}{(\omega_{EM} + 1)} \cdot \eta_{EM} \\ T_c &= \min(T_1, T_2) \end{aligned} \tag{3.78}$$

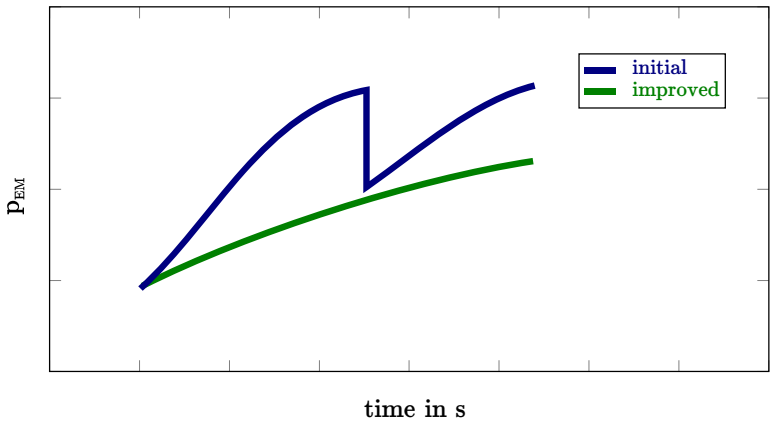

Figure 3.39: Feedforward p_{EM} control

As ω_{EM} is found in the denominator in Equation (3.78), 1 is added to its value in order to avoid a division by zero at standstill. The allowed torque T_c is then compared to the maximum EM torque $T_{EM,max}$ in order to obtain p_{EM}.

3.4 Predictive Charging Strategy (PCS) Development

3.4.1 Optimization - Optimal Control

Optimization is a way of expanding the frontiers of technical feasibility and has therefore penetrated many branches of natural, engineering and economic science. The number as well as the magnitude of problems solved by optimization is steadily increasing [47]. The design of a predictive charging strategy counts among the domain of optimal control, which will be described in the following.

For the optimal control problem, [58] suggests a problem formulation similar to Equation (3.79). The state $\zeta \in \mathcal{Z}$ and the control variable $\chi \in \mathcal{X}$ are optimized by minimizing the functional $f(\chi, \zeta)$ under consideration of the constraint $c(\chi, \zeta)$=0:

$$\begin{gathered} min\ f(\chi,\zeta) \text{ subject to } c(\chi,\zeta)=0,\ d(\chi)\in C_v, e(\zeta)\in C_w \\ \text{with the transformations} \\ f:\mathcal{X}\times\mathcal{Z}\to\mathbb{R},\ c:\mathcal{X}\times\mathcal{Z}\to\mathcal{O},\ d:\mathcal{X}\to\Pi,\ e:\mathcal{Z}\to\mathcal{P}, \\ \text{the spaces } \mathcal{O},\Pi,\mathcal{P},\mathcal{X},\mathcal{Z} \text{ and the closed sets } C_v\subset C, C_w\subset\mathcal{P} \end{gathered} \tag{3.79}$$

Where $d(\chi) \in C_v$ denotes, that the state $\mathcal{X}$ is bounded. $e(\zeta) \in C_w$ expresses the bounded control variable. The Equation $c(\chi, \zeta)$=0 denotes the answer of the system in the state $\chi \in \mathcal{X}$ to the control variable $\zeta \in \mathcal{Z}$. Discretization has to be applied in order to obtain a finite dimensional problem [58]. The dynamic programming approach is one possible solution and will be described Section 3.4.2. For the predictive charging strategy development, the general optimal control problem can be limited to an optimal control problem with specified final state and fixed end time, which will be presented in the following.

Optimal Control with specified (final) state and fixed end time

Having introduced the optimal control problem using general variables and statements in the previous section, the problem formulation for the charging strategy application will be shown.

Objective function: In this case, the objective function is defined by the minimal fuel consumption or maximum fuel efficiency. The two formulations do not compromise, as $minf(x) = max{-}f(x)$ holds [47]. Besides the assessment of the fuel saving potential, the objective function also denotes the CO_2 saving potential. If the assumption of carbon-neutral electricy generation holds, the objective function is a direct measure, otherwise weighting factors have to be introduced [27].

Control variable: The control variable allows to interfer with the system's behavior. In this thesis, the ICE state (on/off) was chosen, resulting in a boolean control variable

(see Equation (3.80)). The grid resolution N_ζ can therefore reduced to 2, which results in faster computation, see Section 3.4.3. If ζ=0 holds, the propulsion power has to be provided solely by the battery, otherwise the ICE generates power which is transferred to the battery by the EMG and then used for propulsion.

$$\zeta = \begin{cases} 0 & \text{ICE off} \\ 1 & \text{ICE on} \end{cases} \tag{3.80}$$

State variable: The state variable χ denotes the dynamic state of the system defined by $c(\chi, \zeta)$=0 [58]. There is no restriction to one state variable, but the number of state variables increases computation time exponentially [56]. Due to this reason, the battery's state of charge will be used as the only state variable, in compliance with [19], [54] and [56].

In the following, the restrictions of the optimal control problem according to [55] are explained.

Fixed end time: The end time is defined by the specified driving cycle and therefore known a-priori. If the cycle's velocity profile cannot be reproduced by the vehicle model, the problem formulation is declared as infeasible and the simulation is stopped.

Specification of the (final) state: As the SOC needs to comply with the battery's restrictions SOC_{min} and SOC_{max} it is limited for every time step. Conclusively, the final state is also limited. In particular, for the predictive charging strategy the final SOC is equal to SOC_{min}.

Disturbances: In order to apply the dynamic programming approach, all disturbances have to be known a-priori [19]. This requires the control variable to be perfectly realized, which is assumed in this case.

With this specifications, the optimal control problem can be reformulated as follows (see [55]):

$$\begin{aligned} \min_{\zeta(t)} \; & J(\zeta(t)) \text{ subject to} \\ \dot{\chi}(t) &= F(\chi(t), \zeta(t), t) \\ \chi(0) &= \chi_0 \\ \chi(t_f) &\in [\chi_{f,min} \; \chi_{f,max}] \\ \chi(t) &\in [SOC_{min} \; SOC_{max}] \\ \zeta(t) &\in [0 \; 1] \\ \text{with } J(\zeta(t)) &= G(\chi(t_f)) + \int_0^{t_f} H(\chi(t), \zeta(t), t) dt \end{aligned} \tag{3.81}$$

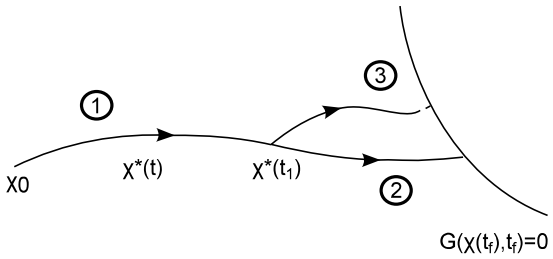

Figure 3.40: Bellmann's optimality principle: (1) optimal trajectory (2) remaining trajectory (3) non existing trajectory reaching the final state with reduced costs; an existence of (3) would corrupt the optimality of (1) [43]

The cost function $J(\zeta(t))$ consists of the infinitesimal cost functional $H(\chi(t), \zeta(t), t)$, which describes the fuel consumption for every time step, and the weighting term of the final state $G(\chi(t_f)$. This allows an assessment of the final state, as $G(\chi(t_f)$ penalizes the deviation from the specified final state $\chi(t_f) = SOC_{min}$. The dynamic system and its physical relations are described by $\dot{\chi}$. The functional $F(\chi(t), \zeta(t), t)$ describes the alternation of the SOC χ for a specified timestamp t under consideration of the control variable ζ. The initial SOC is denoted by χ_0 and the feasible area of the SOC during the driving cycle is restricted by $[SOC_{min}\ SOC_{max}]$. Theoretically, the SOC at the final state $\chi(t_f)$ underlies the same restrictions, but as mentioned before $\chi(t_f) = SOC_{min}$ applies. In this formulation, $\zeta(t)$ and $\chi(t)$ are continuous variables which are discretized when applying the dynamic programming approach described in the following.

3.4.2 Dynamic Programming (DP)

Dynamic programming was developed in the 1950's by Richard Bellmann [8] and has proven to be a highly capable tool for optimal control problems. The fundamental idea of the dynamic programming approach is expressed in Bellmann's optimality principle: *An optimal policy has the property that whatever the initial state and initial decision are, the remaining decisions must constitute an optimal policy with regard to the state resulting from the first decision* [8]. This means that the solution method is to divide the specified complex problem into smaller subproblems, see Figure 3.40.

Solution method

To solve the problem specified in Equation (3.81) using the DP approach, the continuous variables ζ and χ need to be discretized in the form $\zeta_k \in \mathcal{Z}_k$ and $\chi_k \in \mathcal{X}_k$. The index k denotes the corresponding time step. The number of elements contained in $\mathcal{Z}_k$ and $\mathcal{X}_k$ is determined by the grid resolutions N_ζ and N_χ. The solution method described in the follwing is based on [55].

The discretized model is defined as follows:

$$\chi_{k+1} = F_k(\chi_k, \zeta_k) \quad k = 0 \dots N-1 \tag{3.82}$$

This can be reformulated as:

$$\chi_{k+1} = \chi_k + \Delta\chi = \chi_k + f_k(\chi_k, \zeta_k) \quad k = 0 \dots N-1 \tag{3.83}$$

The cost J_N for the final state χ_N^i is defined according to Equation (3.84). The variable g_N denotes an assessment of the final state, whereas Φ_N imposes a penalty on infeasible regions of the final state in order to exclude them from the optimal solution. The discretized state variable for a specific time step k and state node i is given by χ_k^i.

$$J_N(\chi^i) = g_N(\chi^i) + \Phi_N(\chi^i) \tag{3.84}$$

The cost-to-go function J_k for the remaining time steps $k = N-1 \dots 0$ is defined as:

$$J_k^*(\chi^i) = \min_{\zeta_k \in \mathcal{Z}_k} \left\{ h_k(\chi^i, \zeta_k) + \Phi_k(\chi^i) + J_{k+1}^*(F_k(\chi^i, \zeta_k)) \right\} \tag{3.85}$$

The variable h_k performs an assessment of the state ζ and Φ_k penalizes infeasible combinations of χ^i and ζ_k. Optimal control is performed by minimizing the cost function J_k. $F_k(\chi^i, \zeta_k)$ represents a continuous variable, whereas J_{k+1} is only evaluated in the discretized state space. To have $F_k(\chi^i, \zeta_k)$ match one of the possible states $\mathcal{X}_k$, linear interpolation is performed [55]. Applying the nearest neighbour method would also be possible, but requires a fine grid [19] and is therefore discarded.

HEV time discrete optimal control

For the time discrete optimal control of a hybrid electric vehicle Equation (3.83) can be formulated as (compare [55])

$$\chi_{k+1} = \chi_k + f_k(\chi_k, \zeta_k, v_k, a_k) \quad k = 0 \dots N-1, \tag{3.86}$$

where the variable v_k denotes the vehicle speed and a_k the vehicle acceleration, respectively. Since the velocity profile is assumed to be known in advance, Equation (3.86) becomes

$$\chi_{k+1} = \chi_k + f_k(\chi_k, \zeta_k, k) \quad k = 0 \dots N-1, \tag{3.87}$$

where k denotes the actual time step which allows an assignment of the variables v_k and a_k. The time discrete optimal control problem with fixed end time for the determination of the minimal fuel consumption m_f reads

$$
\begin{aligned}
&\min_{\zeta_k \in \mathcal{Z}_k} \Delta m_f(\zeta_k, k) \\
&\text{in order that} \\
\chi_{k+1} &= \chi_k + f_k(\chi_k, \zeta_k, k) \\
x_0 &= SOC_0 \\
\chi_N &\in [SOC_{min}\ SOC_{max}] \\
\chi_k &\in [SOC_{min}\ SOC_{max}] \\
\zeta_k &\in [0\ 1] \\
N &= \frac{t_f}{\Delta t} + 1
\end{aligned}
\tag{3.88}
$$

3.4.3 Computation Time Reduction

Due to the complexity of the problem, efficient computation is inevitable for real time capability. The taken measures to reduce the calculative burden are described in the following.

Precalculations

Variables that are not a function of the control variable ζ are evaluated before the optimization algorithm is started. This reduces computation time within the vehicle model. As the evaluation of the vehicle model is the main contributor in terms of simulation effort, this helps to significantly diminish the total simulation time [55].

As the velocity profile of the driving cycle is known a priori, the angular speeds and the resulting overall demanded torque can be calculated for every time step independently from the control variable ζ. When calling the DP algorithm, only the effects of the control variable on the battery have to be considered, which consequently reduces computation time.

Dimension reduction of lookup tables

By using the precalculated values for the angular speed and torque, the two dimensional lookup tables of the ICE and EM can be reduced by one dimension. This procedure decreases simulation time within the vehicle model and is depicted in Figure 3.41. For details compare [27].

Grid Resolution

The continuous optimal control problem is solved by approximating it with a discrete problem, which is then forwarded to the dynamic programming algorithm. Discretization causes the obtained solution to differ from the continuous problem's optimum. As the continuous problem cannot be solved, its solution is estimated by increasing the grid size until no significant changes are notable in the resulting fuel consumption. As the control variable ζ is of boolean type in this application case (see Equation (3.80)), the

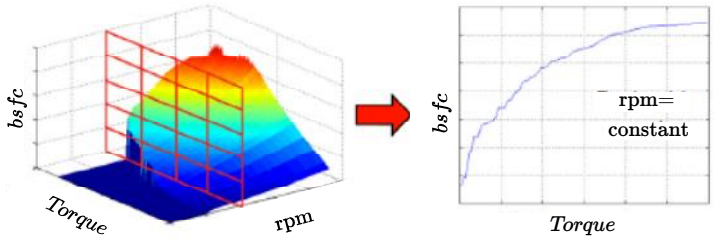

Figure 3.41: Dimension reduction of 2D lookup tables to 1D lookup tables [27]

control variable's grid resolution N_ζ=2. The resolution for the state variable is set to N_χ=64, as similar studies have shown, that a further increase of N_χ does only marginally increase accuracy (<1% deviation between N_χ=64 and N_χ=4096 [27]). The necessity of the optimal choice of N_χ is attributable to the fact that simulation time increases linearly with the grid resolution [27].

3.4.4 Quasistatic Vehicle Model

In order to perform optimization tasks, the optimization model (in this case the vehicle model) needs to be specified. Whereas for driveability investigations a dynamic model was implemented, the investigation of the fuel saving potential will rely on a quasistatic model (compare Section 3.1.1) presented in the following. By evaluating the driving resistance forces, the resulting torque at the wheels can be calculated using Equation (3.89). Under consideration of the efficiencies of the drivetrain components the power demand for the ICE and the EMG can be computed, which is then converted into the equivalent battery power delivery. As the drivetrain components have already been discussed when describing the dynamic vehicle model in Section 3.1, only the properties and Equations necessary for the predictive charging strategy will be presented.

3.4.4.1 Wheel and Drivetrain

The resulting wheel momentum caused by the resistance forces (compare Section 3.1.2) reads

$$T_{res} = (F_r + F_d + F_g + F_a) \cdot r_{dyn}. \tag{3.89}$$

The rotational speed can be calculated by using the velocity v_x and the dynamic tire radius r_{dyn}:

$$\omega_T = v_x / r_{dyn}. \tag{3.90}$$

Under consideration of the final drive and the summation gear ratio, the angular speed of the traction motor reads

$$\omega_{EM} = \omega_T \cdot i_{FD} \cdot i_{SGR}. \tag{3.91}$$

The torque at the EM can be calculated from the torque acting on the tires under consideration of the tires' acceleration resistance and the gear ratio of the final drive i_{FD} and summation gear i_{SGR}:

$$T_{EM,raw} = \frac{T_{res} + \Theta_T \cdot \dot{\omega}}{i_{FD} \cdot i_{SGR}} \tag{3.92}$$

A consideration of the powertrain losses is done by differentiating between traction mode and generator mode and including the efficiencies of the final drive η_{FD} and the summation gear η_{SGR}

$$T_{EM} = \begin{cases} T_{EM,raw} \cdot \frac{1}{\eta_{FD} \cdot \eta_{SGR}} & T_{EM,raw} \geq 0 \\ T_{EM,raw} \cdot \eta_{FD} \cdot \eta_{SGR} & T_{EM,raw} < 0 \end{cases} \tag{3.93}$$

3.4.4.2 Internal Combustion Engine (ICE)

Evaluation of the data gathered during test drives with the experimental HEV showed, that combined mode (compare Section 3.2.1) hardly ever occurs. Therefore, the angular velocity ω_{ICE} can be calculated by evaluating the engine speed lookup tables implemented in the operating strategy. Consequently, the rotational speed ω_{ICE} is a function of the velocity and the driving style as depicted in Figure 3.42.

The ICE's fuel consumption is a function of the engine speed ω_{ICE} and the engine torque T_{ICE} and is evaluated using the dynamic model's lookup table depicted in Figure 3.5.

Since the engine is operated along the eCVT target line specified in Figure 3.36, the drag torque does not have to be considered, as no towing of the ICE occurs. The inertia in contrast is considered in the acceleration torque denoted by

$$T_{acc,ICE} = \Theta_{ICE} \cdot \dot{\omega}_{ICE} \tag{3.94}$$

3.4.4.3 Electric Motor/Generator (EMG)

When acting as a motor, the EMG converts the electrical energy delivered by the battery into mechanical power P_{mech} used for propulsion. In generator mode, the kinetic energy of the vehicle's motion is converted into electrical power P_{el} and then forwarded to the battery. Under consideration of the power flow, the efficiency can be defined as

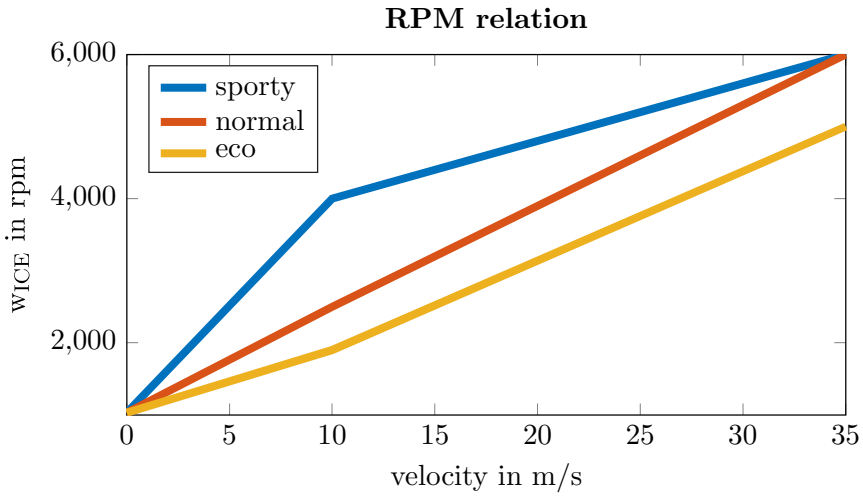

Figure 3.42: Relation between vehicle speed, driving style and engine speed

$$\eta_{EM} = \begin{cases} \frac{P_{mech}}{P_{el}} & T_{EM} \geq 0 \\ \frac{P_{el}}{P_{mech}} & T_{EM} < 0 \end{cases} \tag{3.95}$$

3.4.4.4 Resulting Battery Current and Power

The equation for the required torque T_{req} at the EM reads

$$T_{req} = T_{res,EM} + \zeta \cdot T_{res,ICE} + T_{EM}, \tag{3.96}$$

where $T_{res,EM}$ denotes the resistance torque of the EM, ζ the control variable which represents the ICE state (see Equation (3.80)), $T_{res,ICE}$ the resistance of the ICE and T_{EM} the torque calculated in Equation 3.93.

In case the ICE provides additional power, the generator converts it into electrical power:

$$P_{EG,el} = \frac{\omega_{ICE} \cdot T_{ICE}}{\eta_{EG}} \tag{3.97}$$

Consequently, the requested battery power reads

$$P_{Bat} = \begin{cases} T_{req} \cdot \omega_{EM} \frac{1}{\eta_{EM}} - \zeta \cdot P_{EG,el} & T_{req} \geq 0 \\ T_{recup} \cdot \omega_{EM} \cdot \eta_{EM} & T_{req} < 0 \end{cases} \tag{3.98}$$

It can be seen that for a negative torque request the battery power is a function of the recuperated torque T_{recup} and the EM speed ω_{EM} whereas for traction mode it is further

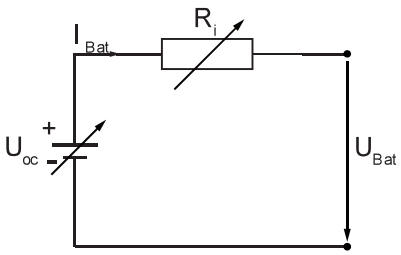

Figure 3.43: Quasistatic battery model

a function of the requested torque T_{req}, the control variable ζ and the electrical generator power $P_{EG,el}$.

3.4.4.5 Battery

The battery model used for the predictive charging strategy is based on [54] and models the battery as parallel and series circuit of elementary cells with serial inner resistance R_i. One cell is depicted in Figure 3.43 and relies on the following equations:

$$U_{Bat} = U_{OC} - R_i \cdot I_{Bat} \tag{3.99}$$

When applying the relation $P_{Bat} = U_{Bat} \cdot I_{Bat}$ to Equation (3.99), it reads

$$\frac{P_{Bat}}{I_{Bat}} = U_{OC} - R_i \cdot I_{Bat} \tag{3.100}$$

After multiplying Equation (3.100) with I_{Bat} and solving for I_{Bat}, the following relation is obtained:

$$I_{Bat} = \frac{U_{Bat} - \sqrt{U_{Bat}^2 - 4 \cdot R_i \cdot P_{Bat}}}{2 \cdot R_i} \tag{3.101}$$

For higher accuracy, U_{Bat} and R_i are a function of the current SOC, which is equal to the state variable χ in the dynamic programming approach. The maximum charging and discharging power as well as the current are limited according to the battery's capabilities $I_{lim,chg}$, $I_{lim,dchg}$, $P_{lim,chg}$ and $P_{lim,dchg}$, respectively. Infeasible values for either I_{Bat} or P_{Bat} are immediately discarded by the optimization algorithm.

The resulting SOC χ_{k+1} is a function of the battery current flow during the timestep Δt, the charging or discharging efficiency $\eta_{c,d}$, the previous SOC χ_k and the nominal cell

capacity Q_{nom}. From Equation (3.102) it can be seen that, a positive battery current (discharging) diminishes the SOC, whereas negative I_{Bat} (charging) increases the SOC.

$$\chi_{k+1} = \chi_k - \frac{I_{Bat} \cdot \eta_{c,d}(I_{Bat}) \cdot \Delta t}{Q_{nom}} \tag{3.102}$$

3.5 Coupling of the Developed Approaches

Having presented the designed strategies in the previous sections, this chapter aims to depict the linkings between them.
Whereas the driveability controller described in Section 3.3 and the developed OS from Section 3.2 are directly incorporated within the dynamic vehicle model described in Section 3.1, the predictive charging strategy can be regarded as an input to the dynamic vehicle model. These dependencies are shown in Figure 3.44.
The predictive charging strategy (PCS) evaluates the optimal progression of the control variable ζ for the given velocity profile $v(t)$. The resulting progression of the ICE state is then forwarded to the dynamic vehicle model consisting of ordinary differential equations (ODE) which also takes the driver model as an input.

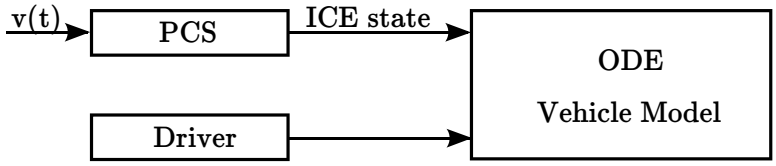

Figure 3.44: Coupling of the developed approaches

4
Results

4.1 Validation of HEV's Drivetrain and Vehicle Model

The vehicle and drivetrain model is validated with the help of single driving manoeuvres and a real-driving cycle, shown in Figure 4.1. The driving cycle in the area of Graz, Austria is used to prove that the simulation model described in Section 3.1 behaves similar to the real vehicle. In particular the identified operation strategy is verified with the help of the cycle: The operation mode for each time step is compared and analysed to ensure that the simulation model with its identified operation strategy is accurate enough and provides close to real vehicle behavior.
The accuracy of the model can be determined by comparing the distance of the driving cycle δ_c with the distance δ_m computed in the model as shown in Equation (4.1). The value of δ_m for each timestep is obtained by integrating the vehicle velocity v_x. As the distances at the end of the cycle are compared, an integral accuracy assessment is performed. The values used in Equation (4.1) are valid for the initial layout and show that the accuracy after completing the whole cycle is about 3.4 % when using a simulation time step Δt of 0.001 s.

$$\Delta\delta = \frac{|\delta_m - \delta_c|}{\delta_c} = \frac{|4.4709 \cdot 10^4 - 4.6269 \cdot 10^4|}{4.6269 \cdot 10^4} = 0.034 \tag{4.1}$$

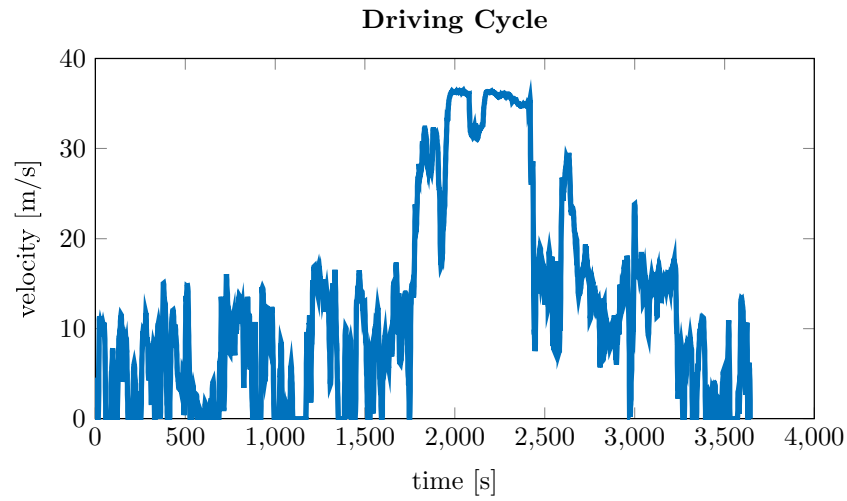

Figure 4.1: Real-world driving cycle speed profile

Further specific events, such as the starting of the ICE by the EG have been investigated and validated. In Figure 4.2 the generator torque of the real vehicle and the Simulink model are shown. It can be seen that a good correlation is achieved in the tow start manoeuvre. Nevertheless, the simulated torque curve is smoother than the measured curve which is a result of not modelling the combustion process and using a piecewise linear torque characteristic.

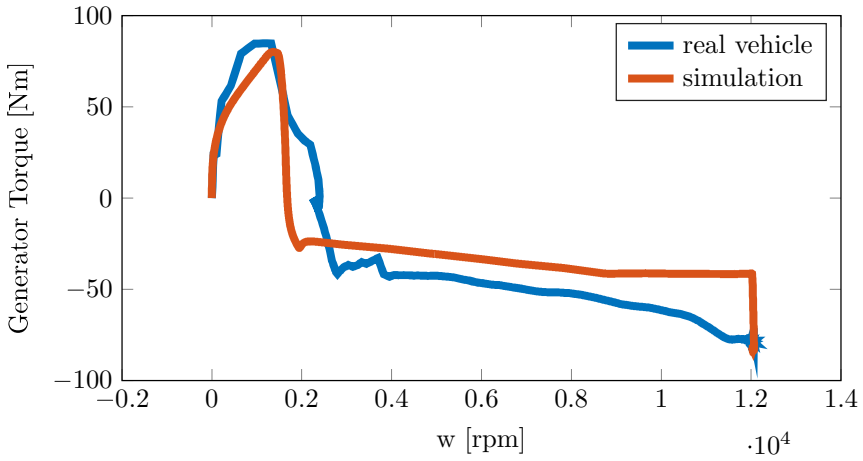

Figure 4.2: Generator torque at a tow start manoeuvre

Also the full load behavior shows a good correlation between simulation and reality. The dotted lines in Figure 4.3 show the behavior of the actual vehicle, whereas the full lines represent the results of the implemented Simulink model. The velocity progressions are almost identical until 5 s and also later only little deviation occurs. The EG torque rises a bit faster in the simulation but overall the torque and angular speed progressions show a good correlation. The generator power progressions are also nearly identical, only at 7 s a small difference is notable.

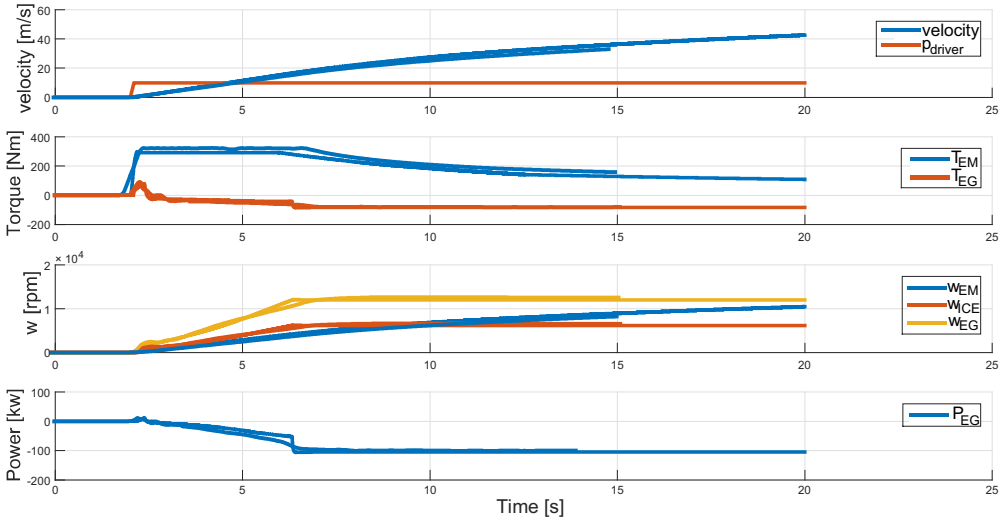

Figure 4.3: Validation of the simulation model with the help of full load manoeuvres

4.2 Comparison of the Developed Driveability Controller and Initial Layout

Having discussed the implemented strategies to enhance driveability in Section 3.3 the benefits shall now be presented by the evaluation of different driving manoeuvres.

Full load acceleration:

As the vehicle behavior should remain predictable in emergency situations the full load characteristic is not affected by the driveability algorithm. Figure 4.4 shows the vehicle speed and pedal position. It can be seen that the acceleration behavior equal for all driving styles, meaning that in case of overtaking the full system power is available for every driver type. In Figure 4.5 the EM rotational speed is depicted. An almost linear increase in the angular speed can be seen which is an expression of predictable vehicle behavior. Figure 4.6 displays the power at the EM over time. After reaching the first plateau between seconds 5 and 10, the power drops to a second plateau which is caused by the EM characteristic shown in Figure 3.38.

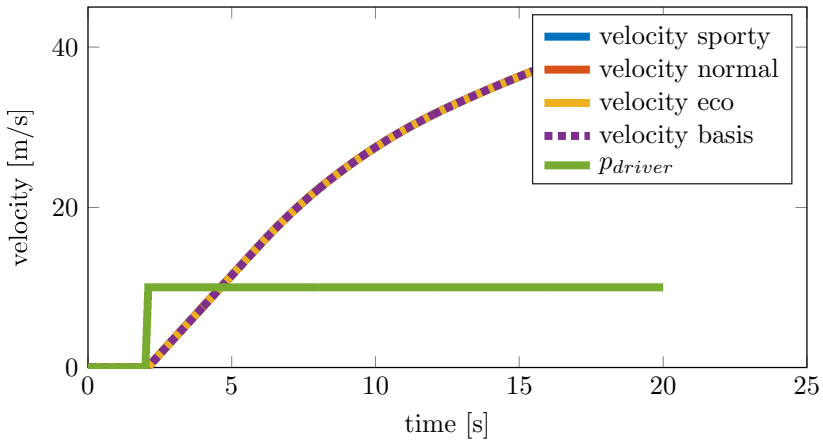

Figure 4.4: Velocity and pedal position of a full load manoeuvre

Figure 4.7 depicts the rotational speed of the ICE in correlation with the velocity. The maximum ICE speed is reached at about 17 m/s, meaning that from this time the ICE delivers maximum power to the generator (compare Figure 3.36).

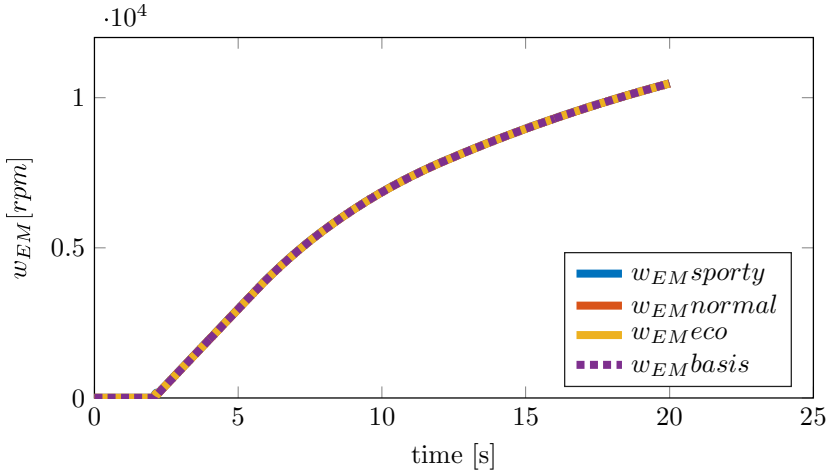

Figure 4.5: EM rotational speed of a full load manoeuvre

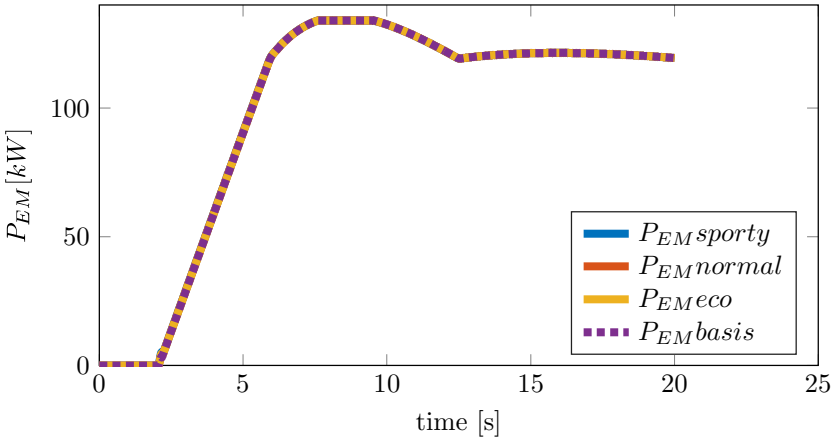

Figure 4.6: EM power of a full load manoeuvre

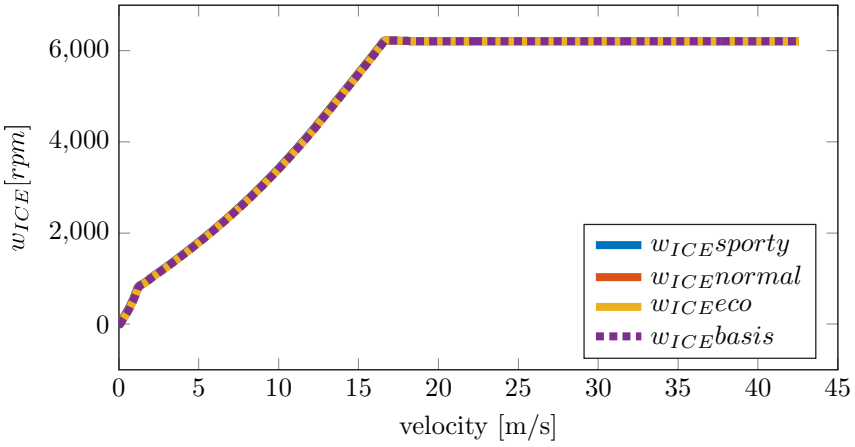

Figure 4.7: ICE rotational speed of a full load manoeuvre

80 % load acceleration:

This high load driving manoeuvre clearly shows the enhanced vehicle response due to the driveability controller. Figure 4.8 denotes that the fast rpm increase of the ICE could be eliminated with the driveability algorithm, therefore delivering a reconnection of the driver with the drivetrain. Sporty drivers benefit from an engine speed of 4000 rpm at about 10 m/s which results in good power delivery.

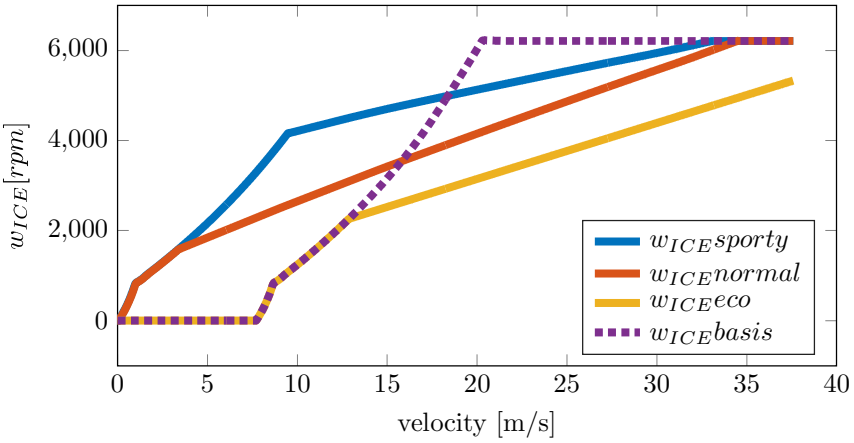

Figure 4.8: ICE rotational speed of a 80 % load acceleration

Not only the velocity but also the acceleration is improved compared with the basis layout as shown in Figure 4.9. The acceleration is smooth without containing any drop. The EM angular speed depicted in Figure 4.10 directly correlates with the vehicle velocity which underlines the improved vehicle performance for normal and sporty drivers.

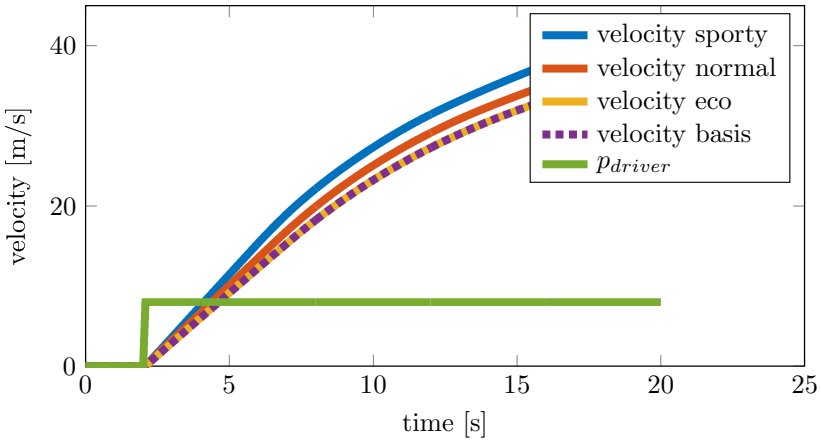

Figure 4.9: Velocity and pedal position of a 80 % load acceleration

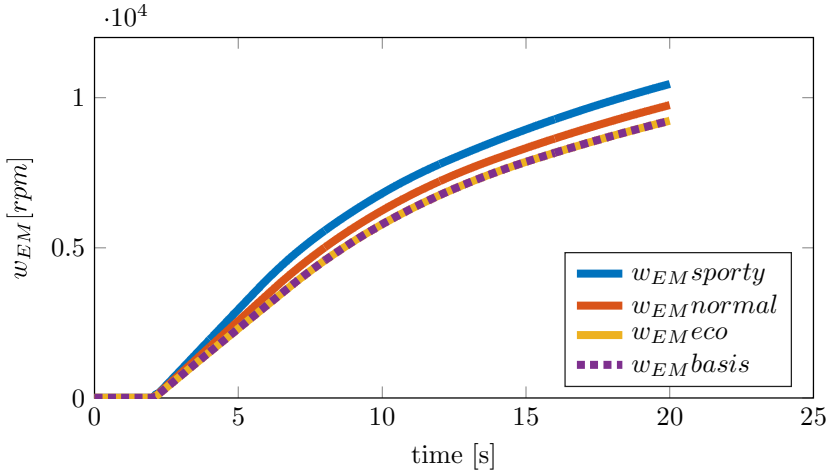

Figure 4.10: EM rotational speed of a 80 % load acceleration

The improved power delivery of the EM for normal and sporty drivers can be seen in Figure 4.11. Besides increasing the power gradient also the power output is increased. Whereas the initial layout only provided about 100 kW, sporty drivers benefit from approximately 120 kW.

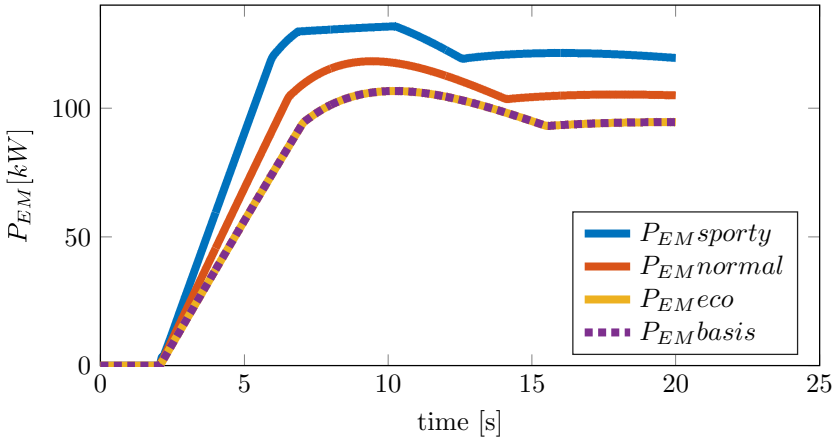

Figure 4.11: EM power of a 80 % load acceleration

50 % load acceleration:

The half load acceleration manoeuvre also proves the increased vehicle response for sporty drivers. Figure 4.12 shows that the driveability controller not only affects the rpm relation, but also the starting point of the ICE. Whereas for eco drivers the ICE is started at a speed of 13 m/s, sporty drivers have an ICE starting speed of about 7 m/s for this manoeuvre. The different starting speeds are a result of the EM power delivery which is shown in Figure 4.15. In order to comply with the battery limitations, the ICE has to be started up earlier when demanding more power from the EM.

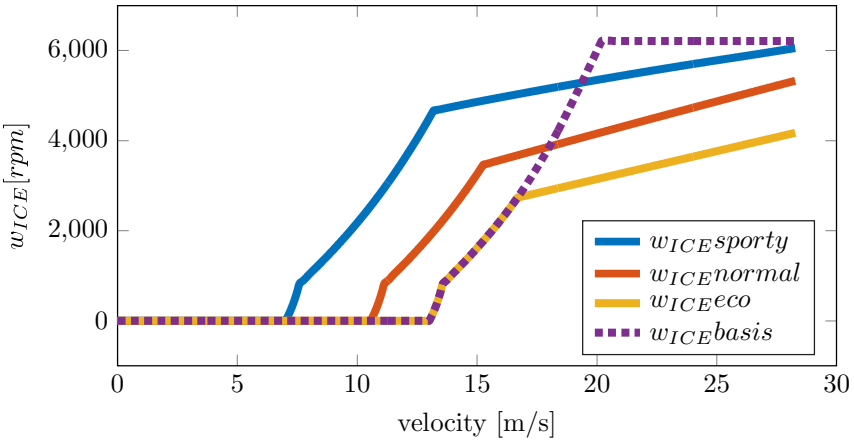

Figure 4.12: ICE rotational speed of a 50 % load acceleration

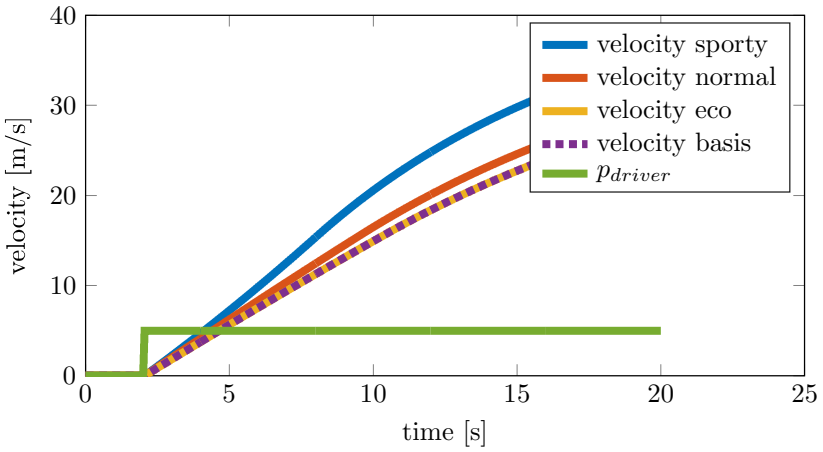

Figure 4.13: Velocity and pedal position of a 50 % load acceleration

Further it can be seen that eco and normal drivers after 10 s benefit from almost constant power delivery whereas sporty drivers have to cope with decreasing EM power between seconds 12 and 17. As normal and sporty drivers reach higher velocities than the initial

layout (compare Figure 4.13), the EM angular velocity displayed in Figure 4.14 also needs to be greater for these driving styles.

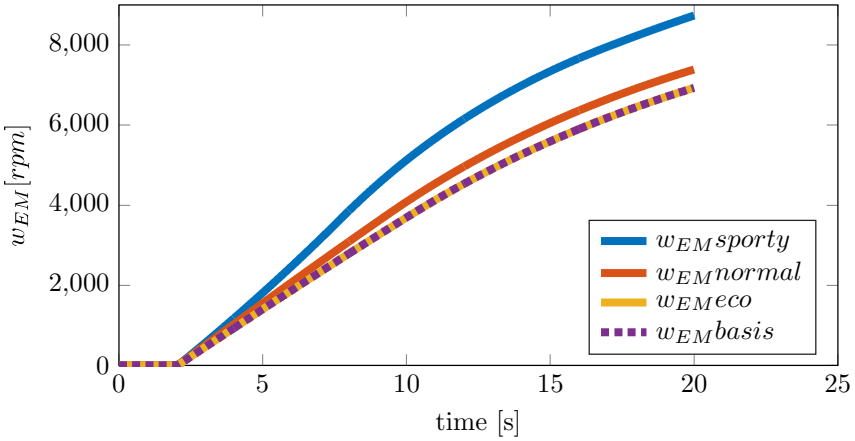

Figure 4.14: EM rotational speed of a 50 % load acceleration

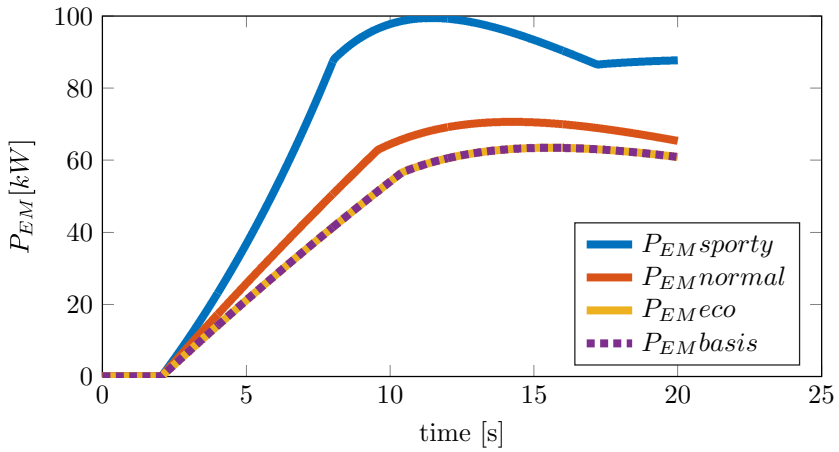

Figure 4.15: EM power of a 50 % load acceleration

Short pedal kick:

This manoeuvre allows to evaluate the short-time responsiveness of the vehicle. While sporty and normal drivers provoke an immediate start-up of the engine, the ICE remains switched off for eco drivers (see Figure 4.16) resulting in better fuel consumption and driving comfort. Furthermore, it can be seen that the engine rpm is not only a function of the vehicle speed for acceleration phases, but also for deceleration phases. For sporty drivers the fast engine start-up and high rpm leads to a benefit in case of a following acceleration manoeuvre, but triggers the battery constraints in the deceleration phase leading to a shut down of the ICE, see Figure 4.16. For normal drivers the engine rpm is also for the deceleration phase a function of the vehicle speed (seconds 6 to 20) which can be seen by the overlapping red lines in Figure 4.16 in the velocity domain of 7 to 10 m/s.

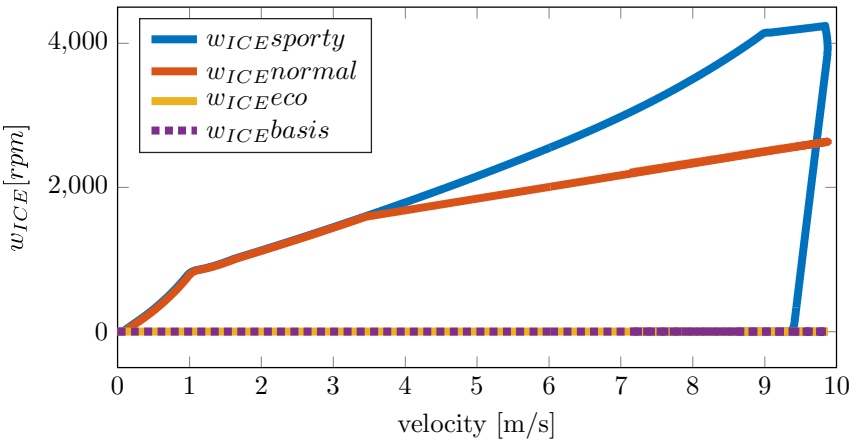

Figure 4.16: ICE rotational speed of a short pedal kick manoeuvre

In Figure 4.17 the velocity and driver pedal position can be seen. Whereas the accelerator pedal is fully pressed at 2 seconds, the pedal position is reduced to about 80 % at about 5 seconds and 6 seconds after the start of the manoeuvre the pedal is released. The increased velocity for normal and sporty drivers can also be witnessed in the angular speed of the EM shown in Figure 4.18. Even though the accelerator pedal is only actuated for a short amount of time, sporty drivers cause the EM to rev up to about 3100 rpm whereas the initial layout produces an EM speed of about 2200 rpm.

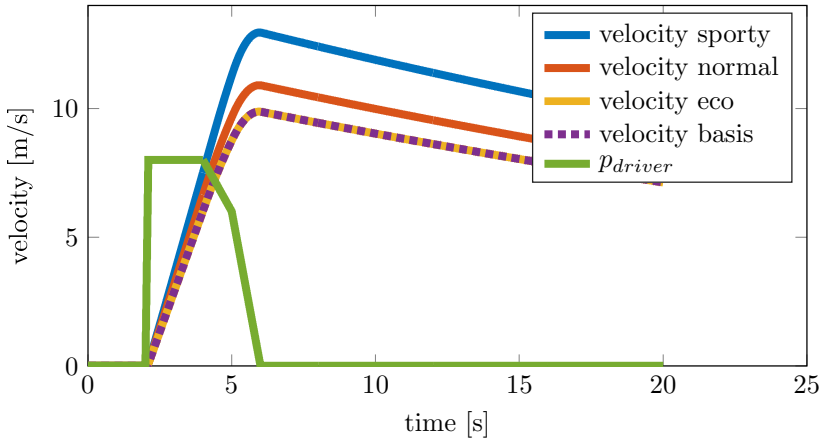

Figure 4.17: Velocity and pedal position of a short pedal kick manoeuvre

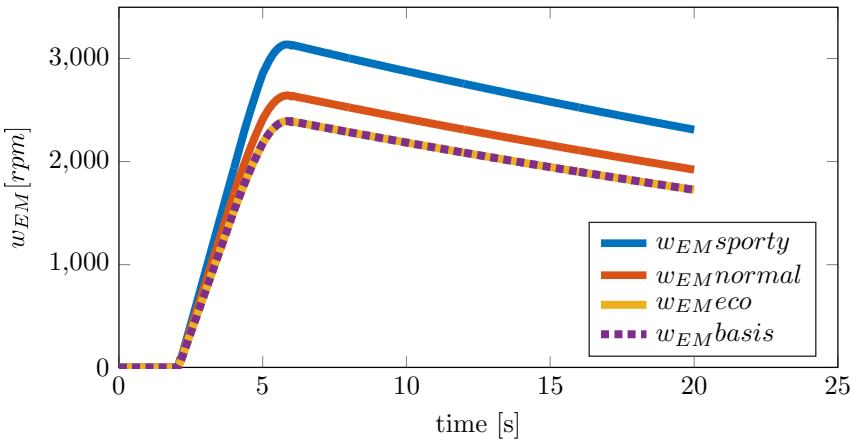

Figure 4.18: EM rotational speed of a short pedal kick manoeuvre

Due to the starting of the ICE for normal and sporty drivers, the EM power can be increased as the battery is charged by the EG. The resulting EM power progression is depicted in Figure 4.19. For sporty drivers the EM delivers about 80 kW, whereas the initial layout only produces close to 40 kW.

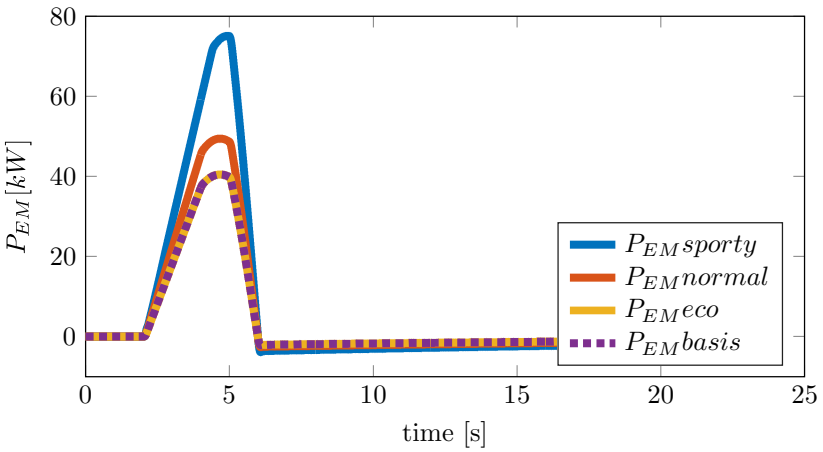

Figure 4.19: EM power of a short pedal kick manoeuvre

4.3 Predictive Charging Strategy and Fuel Saving Potential

In this section, the fuel consumption of the vehicle is evaluated. As the focus of this thesis lies on real-driving fuel saving potential, a real world driving cycle is used. In specific, it is the same cycle used for the model validation in Section 4.1. The velocity profile is shown in Figure 4.1. The less desirable operation strategy with the accelerator pedal input being disconnected from the engine speed is used as an outline to address the fuel saving potential. Figure 4.20 shows the fuel consumption, ICE state and SOC progression of the initial layout. It can be seen that a total amount of 5.8 litres is used during the cycle. The ICE state progression shows that frequent mode shifts occur. This is a result of the rule-based operation strategy allowing the ICE state to change every second. In order to allow a comparison of the different operating strategies the ICE state and the SOC progression are shown for the entire driving cycle. To assure a fair comparison the initial SOC SOC_0 is set to 0.9 for all of the following investigations.

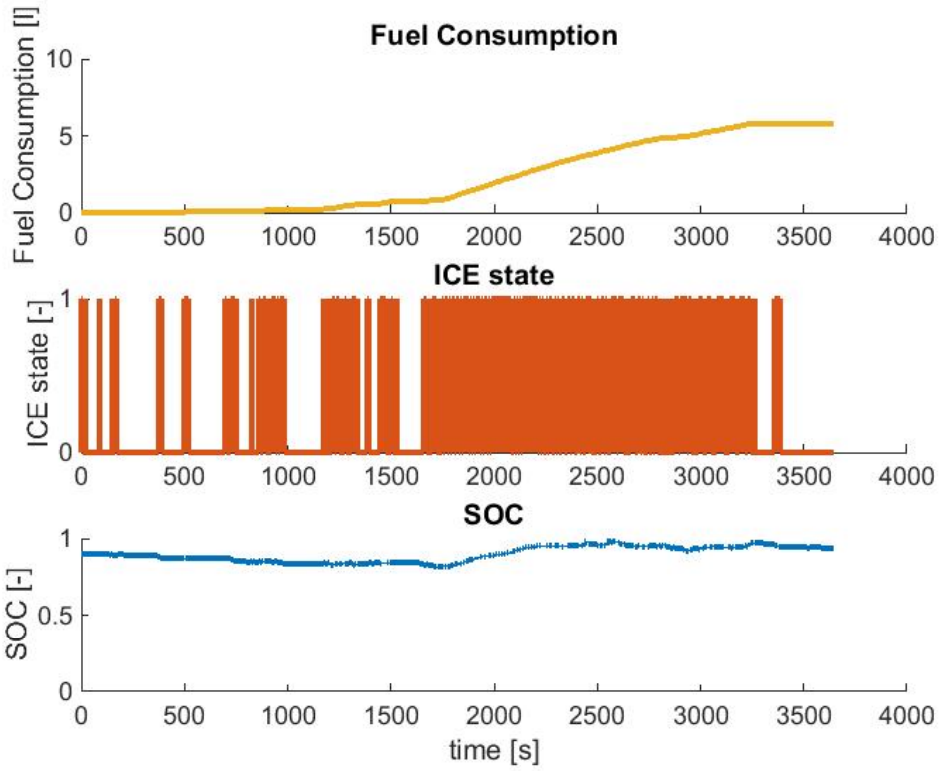

Figure 4.20: Fuel consumption, ICE state and SOC of the initial layout

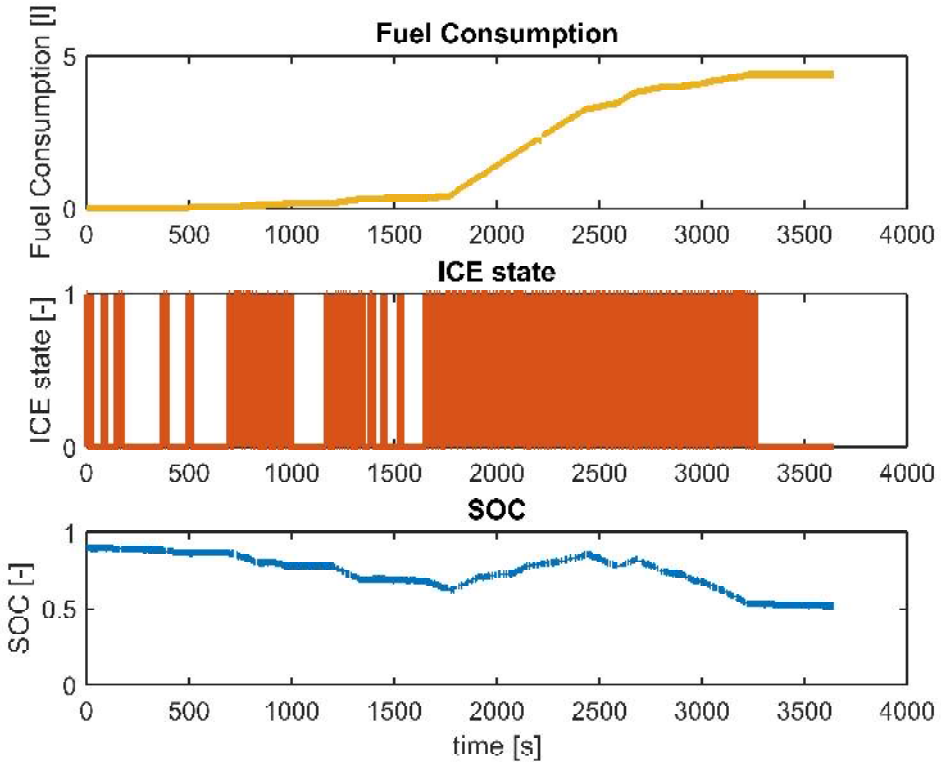

Figure 4.21: Fuel consumption, ICE state and SOC with driveability controller (normal driver)

Next, the fuel consumption, ICE state and SOC progression for the implemented driveability controller under estimation of a normal driver are discussed. Figure 4.21 shows that 4.4 litres of fuel were consumed during the cycle. Comparing the ICE state of the initial layout with the normal driver's ICE state it can be seen that the two are almost identical. This is due to the fact that the OS in general has been left unchanged whereas the rpm range of the ICE has been modified in order to enhance driveability which in this case also reduces fuel consumption.

For eco drivers, the ICE state also resembles the progression obtained when assuming a normal driver. Due to the low engine speed range, the fuel consumption is further reduced. The eco layout of the driveability controller produces a total fuel consumption of 4 litres (compare Figure 4.22) which is equal to a saving of 31%[1] in comparison to the initial layout. These results clearly state that driveability enhancements also have an influence on the fuel consumption of a vehicle: By tailoring the vehicle characteristics according to the driver's needs fuel efficiency can be significantly increased.

When comparing the SOC progression for the initial layout and the implemented drive-

[1]Without considering the difference in the final SOC and the model accuracy

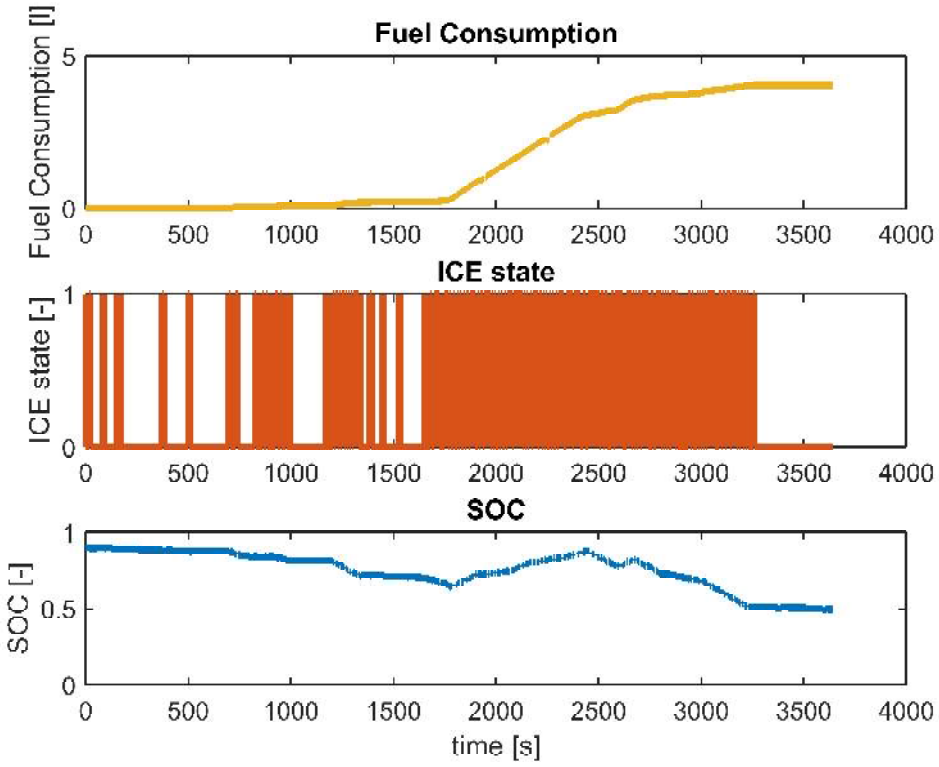

Figure 4.22: Fuel consumption, ICE state and SOC with driveability controller (eco driver)

ability controller, it can be seen that the high revolution range of the ICE causes the SOC to be 0.92 at the end of the cycle whereas the driveability controller causes the SOC to fall to about 0.5 at 3646 s for the normal driver (Figure 4.21) as well as for the eco driver (Figure 4.22). This energy difference also needs to be considered when assessing the fuel saving potential between the different strategies. Depending on the energy mix used for electricity generation, the final SOC has to be weighted and converted to a fuel equivalent to perform a proper depiction of the fuel saving potential.
Nevertheless, the comparison showed that the SOC progression has an impact on the fuel economy of a vehicle and therefore represents a measure for reducing fuel consumption. This is the point where the predictive charging strategy comes to play: It calculates the optimal ICE state under consideration of the final SOC (which is set to be $SOC_{final} = SOC_{min} = 0.3$ for the following investigations) to further increase fuel economy. With these constraints the time discrete optimal control problem with fixed end time given in Equation (3.88) can be reformulated according to Equation (4.2). The boundaries for the state variable χ listed in Equation (4.2) were chosen to ensure maximum longevity of the battery.

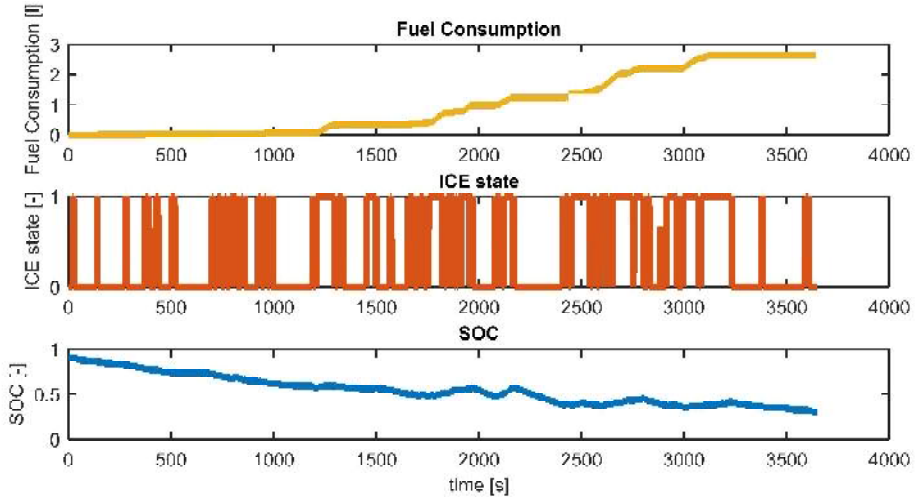

Figure 4.23: Fuel consumption, ICE state and SOC with predictive charging strategy (eco driver)

$$
\begin{aligned}
&\min_{\zeta_k \in \mathcal{Z}_k} \ \Delta m_f(\zeta_k, k) \\
&\text{in order that} \\
\chi_{k+1} &= \chi_k + f_k(\chi_k, \zeta_k, k) \\
\chi_0 &= 0.9 \\
\chi_N &\in [0.3 \ 0.95] \\
\chi_k &\in [0.3 \ 0.95] \\
\zeta_k &\in [0 \ 1] \\
N &= 3646
\end{aligned}
\tag{4.2}
$$

The time step is set to Δt=1s which results in the control variable only being changed every second and sets N=3646. This is done to ensure that the assumptions made in the quasistatic vehicle model hold and has also been performed likewise in other investigations [19], [54], [55], [56]. Figure 4.23 shows the fuel consumption, ICE state and SOC progression for eco drivers under application of the predictive charging strategy. The fuel consumption is reduced to 2.6 litres by reducing the on-time of the ICE and fully exhausting the battery potential which results in a final SOC of 0.3. Furthermore, the predictive charging strategy reduces the frequency of the mode shifts between ICE on and ICE off which enhances driveability (compare Figures 4.23 and 4.24).

When applying the predictive charging strategy also to the normal driver, an exact assessment of the fuel saving potential caused by the driveability controller can be made. The initial SOC and the final SOC are identical in both cases (compare Figures 4.23 and

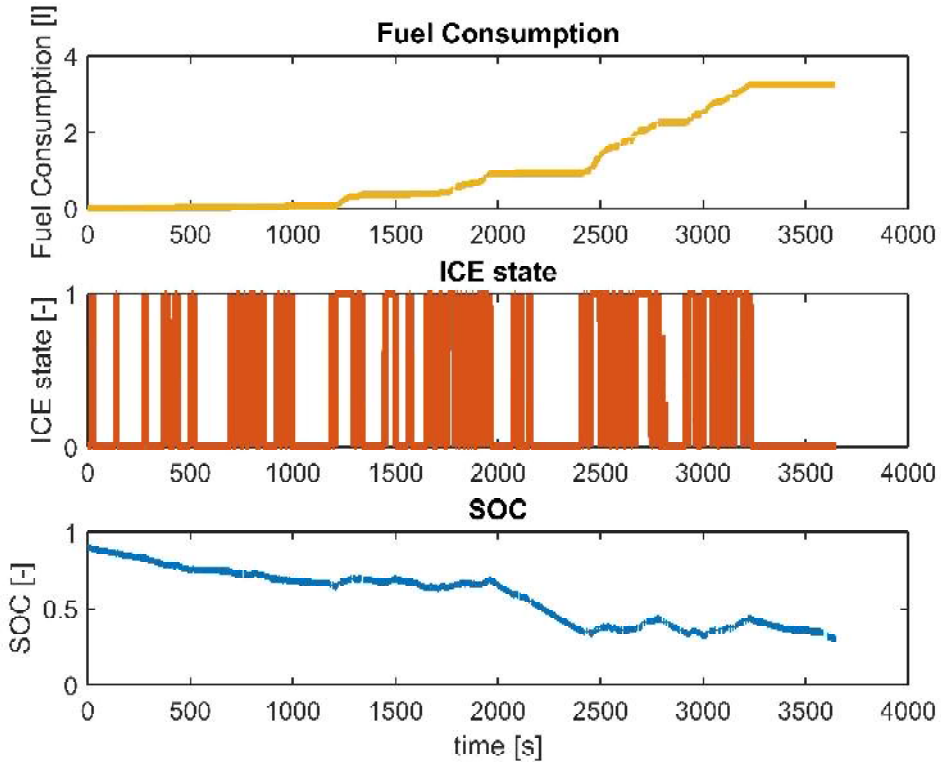

Figure 4.24: Fuel consumption, ICE state and SOC with predictive charging strategy (normal driver)

4.24). Therefore the amount of fuel is a direct measure for the efficiency and no final SOC deviation has to be considered. It can be seen that when applying the predictive charging strategy normal drivers consume a total amount of 3.2 litres during the cycle whereas eco drivers consume 2.6 litres. For eco drivers this is equal to a fuel saving potential of 19%[2] which is only attributable to the driveability controller. When comparing the fuel consumption for the initial rule based layout and the predictive charging strategy under assumption of an eco driver, the savings attributable to the driveability controller and the ones caused by the predictive OS are combined and thus the potential is even greater.

Even though a real world driving cycle has found application and the fuel saving potential has been assessed under consideration of the final SOC, a possible point of criticism lies in the assumption of a known velocity profile for the whole driving cycle. Even when predefining the route in the car's navigation system, considering the driving style with the implemented driveability controller and accounting for the traffic flow, the exact velocity profile is never known.

[2]Without considering the model accuracy

Nevertheless, [27] proves that when performing global optimization fuel consumption does not significantly increase when reducing the prediction horizon (=the zone in which the velocity profile is exactly known). For further information the reader is referred to [27] and [32].

4.4 Conclusion

In order to facilitate a driveability assessment at an early stage of development a full longitudinal vehicle model has been implemented in Matlab Simulink. To reach near to real vehicle behaviour, parameter identification algorithms have been carried out. The identified parameters have been implemented into the vehicle model which was later on validated. After proving good correlation between the simulation and the real vehicle behaviour an initial driveability assessment has been performed. To improve driveability, major emphasis was put on the reconnection of the driver with the drivetrain and the prediction of the driving style using an adaptive algorithm. The advanced algorithm gathers information of the past driving in order to make a short-time prediction for the possible driving style. This predicted driving style is then used to adapt the characteristics of the vehicle.

The presented driving manoeuvres clearly show that an enhancement of driveability could be performed without corrupting fuel economy. Whereas the eCVT target line has been retained in the operating strategy, a reconnection of the driver with the drivetrain could be performed. Now, it is possible that the engine speed is a function of the vehicle speed. Moreover, the driveability controller also allows to tailor the vehicle responsiveness according to the driver's needs. This results in different starting points of the ICE which is demonstrated with the aforementioned driving manoeuvres. Eco drivers have the benefit of operating the ICE at lower rpm which further increases the fuel efficiency of the investigated HEV, proving that the conflicting goals of low fuel consumption and driving pleasure have been overcome. Sporty drivers in contrast benefit of optimised vehicle responsiveness without the driver input being disconnected from the drivetrain. The implemented driveability algorithm not only performs an adaption to the driver, it further allows a prediction of the driving style given the past information. By weighting the past information, the accuracy of the prediction is improved. As the vehicle behavior should be predictable for emergency situations, the full load characteristic is not affected by the driving style.
By replacing the rule based OS with a predictive charging strategy, the fuel economy of the HEV is further improved. By performing global optimization and fully exhausting the battery potential by the end of the trip, the on time of the ICE can be reduced in comparison to the initial OS. By specifying SOC constraints at the beginning and at the end of the trip also a comparison of the fuel saving potential between the different driving styles becomes possible. It is shown that the driveability algorithm not only deletes the ICE's loose rpm behavior but also contributes to the fuel consumption reduction.

Moreover, during the work with the real vehicle and the simulation model it turned out that the lack of driving pleasure and the loose rpm behaviour are not only a result of the implemented operating strategy. The drivetrain components and their interaction also have a high impact on the driveability issue of this specific HEV layout: The battery used in the vehicle and the resulting power or battery current restriction also influence the ICE behaviour. Incorporating a more capable battery into the drivetrain for example

Table 4.1: Component proposal

Maximum EM Power	124 kW
Battery current discharge limitation	80 kW
Proposed Battery current discharge limitation	90 kW

would lead to less frequent ICE starts and wider power and battery current restrictions which help operating the ICE at lower rpm. This specific change is now to be illustrated with the following calculation: The demanded power at the ICE in case of a full power request yields

$$P_{ICE,current} = 124 - 80 = 44\,\text{kW} \tag{4.3}$$

$$P_{ICE,proposed} = 124 - 90 = 34\,\text{kW} \tag{4.4}$$

Given the power demand in Equation (4.4) it can be determined from the eCVT target line chart, that the ICE has to be operated at about 3800 rpm to deliver the requested power whereas the ICE only needs to be operated at approximately 3000 rpm for the proposed layout. Further fuel economy could be increased as 3000 rpm correspond to a BSFC of 220 g/kWh (best operating point) whereas 3800 rpm deteriorate the BSFC. Given the reduced power demand for the ICE also the needed generator power diminishes, leading to a smaller generator.

5 Summary

The focus of this thesis was to improve the driveability and fuel consumption of an existing HEV drivetrain layout. In the following the work is summarised chapter-wise.

Introduction: In this chapter the main features of the project are introduced. After discussing the motivation for hybrid drivetrains, the control problem is presented. By implementing a detailed vehicle model into Matlab Simulink with close to real vehicle behavior, driveability issues can be investigated at an early stage of development. This project aims to use the input of adaptive and predictive strategies to simultaneously enhance fuel efficiency, driveability and vehicle performance. In order to maximize fuel efficiency, an intelligent operation strategy using past and future driving information was developed as a replacement for the rulebased OS implemented in the investigated HEV. Driveability issues are accounted for by incorporating a driveability controller into the HCU. As the proposed modifications only require software modifications, the costs are held at a minimum and the application potential is increased.

State of the Art: This chapter describes the highest level of development regarding hybrid drivetrain structures, operating strategies and driveability assessment. Different topologies of HEV powertrains have been developed throughout the last years. Whereas the complexity constantly increases, these newly developed layouts can all be as refined versions of the three basic architectures presented in this section. Operation strategies form the crucial part of HEVs. Whereas initially rule-based approaches found application, current research is being done towards optimization methods in combination with adaptive and predictive strategies. Driveability assessments are as old as the automobile itself, yet the term driveability is often used with different meanings. This thesis defines driveability as the driver's subjective perception of the interactions between vehicle and driver which can be assessed subjectively or by using objective evaluation criteria based

on correlation methods. For evaluation of driveability vibrations acting on the human body are used. In the VDI 2057 standards for example, the accelerations acting on the human body are assessed in the frequency domain in order perform an objective evaluation of driving comfort. Different measures such as the vibration exposure over time, the running root-mean-square of the instantaneous frequency-weighted acceleration, the vibration dose value, peak-to-peak values and many more are introduced. Finally, the driveability evaluation method implemented in AVL-Drive is presented.

Methodology: This chapter consists of four main parts, namely the vehicle modelling, the identification and modelling of the OS, the development of the driveability controller and the design of the predictive charging strategy. Accurate modelling of the hybrid powertrain is essential when examining driveability issues. The modelling of the different powertrain components such as the internal combustion engine, battery, electric motor/generator, gearbox, final drive, clutch, tire and hub-pitching model are presented in this section. By performing various load variation manoeuvres, the rule-based OS implemented in the investigated HEV was determined. Under consideration of the component restrictions, the rule-based approach was modified to comply with the dynamic vehicle behavior. By performing a driving style classification and incorporating a functional dependency between driving style, vehicle speed and engine speed into the OS the disconnected rpm behavior could be deleted. Further the driving style classifier allows to tailor the vehicle characteristics according to the driver's needs. Eventually, the optimal control problem solved by using a dynamic programming method is presented. After reformulating the general problem in suitable form for the given HEV control problem, measures for computation time reduction are presented and the quasistatic vehicle model is discussed. Finally, the relations between the developed methods are explained.

Results: This chapter shows the outcome of this work. Firstly it is proved that the simulation model behaves similar compared to the real vehicle even in real-world driving cycles, recorded in the area around Graz, Austria. By performing specific driving manoeuvres such as full load accelerations, 80% load accelerations, 50% load accelerations and a short pedal kick manoeuvre, the influence of the developed driveability controller on the vehicle behavior is investigated. Whereas the full load characteristic is not affected by the implemented algorithm due to safety reasons, significant changes regarding the vehicle response and rpm behavior can be observed in the other manoeuvres. The developed controller performs a reconnection of the driver with the drivetrain by having the engine rpm be a function of the vehicle speed. Depending on the driving style, the ICE's starting point varies and for the short pedal kick manoeuvre it remains shut off for eco drivers whereas sporty drivers benefit from the immediate response. In contrast, the implemented charging strategy allows to adapt the SOC progression according to the driving cycle and therefore allows to fully exhaust the battery's energy until the end of the trip leading to great fuel saving potential. Additionally it is shown that the tailoring of the ICE's rpm range by the driveability controller also results in better fuel economy. Consequently, the implemented algorithm allows to enhance driving comfort and pleasure while simultaneously reducing the vehicle's fuel consumption. A discussion

of the influence of the velocity profile's accuracy and the resulting fuel saving potential forms the end of this section.

Discussion: Within this section the future application potential in mass production vehicles is discussed. Hybrid electric vehicles play an important part in every OEMs product portfolio and are gaining rapidly in market shares. Yet, the possible fuel saving potential and driving characteristics are highly influenced by the OS. The work shows that the behavior of the vehicle can be modified with advanced vehicle controllers without changing its hardware. Moreover, it is shown how innovative prediction and adaption algorithms positively contribute to driving pleasure, driving safety and driving comfort. By holding the implementation costs at a minimum and designing the controllers to be used at an early stage of development, the product development process can be shortened and the effort of adaption to prototypes and later-mass production vehicles is reduced.

Final statement and Outlook: This work provides an in-depth analysis of a combined PHEV drivetrain layout. Major emphasis is put on the operation strategy and driveability controller. The introduced driving style classification algorithm is able to predict the driver's future power demand short-term and thus allows an adaption to different driving styles. In combination with a predictive charging strategy the fuel economy of the HEV powertrain layout is further improved. Future expansions could comprise an anti-jerk term in the cost function and a limiting of the minimal ICE on time to prevent frequent mode changes.

List of Figures

List of Tables

Bibliography

[1] M. Ackerl. Innovative Fahrzeugantriebe: Simulation von Fahrzeugen mit alternativen Antrieben. *Lecture Notes, Institute of Automotive Engineering, Graz University of Technology*, 2016.

[2] International Energy Agency. Hybrid and electric vehicles: The electric drive advances. *Annual report of the Executive Committee and Annex I*, 2009.

[3] J. Aigner. Zur zuverlässigen Beurteilung von Fahrzeugen. *ATZ Automobiltechnische Zeitschrift*, Volume 84(9), 1982.

[4] M. Albrecht. *Modellierung der Komfortbeurteilung aus Kundensicht am Beispiel des automatisierten Anfahrens*. PhD thesis, Faculty of Mechanical Engineering, University of Karlsruhe, 2005.

[5] A. Aljaafreh, N. Alshabatat, and M. S. Najim Al-Din. Driving style recognition using fuzzy logic. *IEEE International Conference on Vehicular Electronics and Safety*, Istanbul, Turkey, 2012.

[6] M. Back. *Prädiktive Antriebsregelung zum energieoptimalen Betrieb von Hybridfahrzeugen*. PhD thesis, Faculty of Mechanical Engineering, University of Karlsruhe, 2006.

[7] K. Becker. *Subjektive Fahreindrücke sichtbar machen*. Expert Verlag, 2000. ISBN 978-3-8169-2936-9.

[8] R.E. Bellmann. Dynamic Programming. *Princeton University Press*, 1957. ISBN 978-0-6911-4668-3.

[9] H-H. Braess and U. Seiffert. *Vieweg Handbuch Kraftfahrzeugtechnik*. Springer Vieweg, 2013. ISBN 978-3-658-01691-3.

[10] H. Bubb, K. Bengler, R.E. Grünen, and M. Vollrath. *Automobilergonomie*. Springer Vieweg, 2015. ISBN 978-3-8348-2297-0.

[11] N. Cui, J. Fan, C. Zhang, and J. Wu. Management strategy for hybrid electric vehicle. *3rd IEEE International Symposium on Power Electronics for Distributed Generation Systems (PEDG)*, Aalborg, Denmark, 2012.

[12] M. Debert, G. Colin, Y. Chamaillard, L. Guzzella, A. Ketfi-Cherif, and B. Bellicaud. Predictive energy management for hybrid electric vehicles - prediction horizon and

battery capacity sensitivity. *6th IFAC Symposium Advances in Automotive Control*, Schwabing, Germany, 2010.

[13] D. Dörr, D. Grabengiesser, and F. Gauterin. Online driving style recognition using fuzzy logic. *17th IEEE International Conference on Intelligent Transportation Systems (ITSC)*, Qingdao, China, 2014.

[14] A. Eichberger, J. Fabian, and C. Lex. Fahrzeugmesstechnik. *Lecture Notes, Institute of Automotive Engineering, Graz University of Technology*, 2013.

[15] H. Eichlseder. Verbrennungskraftmaschinen - Vertiefte Ausbildung. *Lecture Notes, Institute of Internal Combustion Engines and Thermodynamics, Graz University of Technology*, 2005.

[16] E. Ericsson. Independent driving pattern factors and their influence on fuel-use and exhaust emission factors. *Transportation Research Part D: Transport and Environment*, Volume 6(5), 2001.

[17] R. Fischer, G. Jürgens, F. Kücükay, R. Najork, and B. Pollak. *Das Getriebebuch.* Springer, 2012. ISBN 978-3-7091-0876-5.

[18] M. J. Griffin. *Handbook of Human Vibration.* Academic Press, 1990. ISBN 978-0-12-303040-5.

[19] L. Guzzella and A. Sciarretta. *Vehicle Propulsion Systems - Introduction to Modeling and Optimization.* Springer, 2013. ISBN 978-3-642-35913-2.

[20] M. T. Hagan, H. B. Demuth, M. H. Beale, and O. De Jesús. *Neural Network Design.* Oklahoma State University, 2 edition, 2014. ISBN: 978-0-971-73211-7.

[21] S. Hausberger. Schadstoffbildung und Emissionsminimierung. *Lecture Notes, Institute of Internal Combustion Engines and Thermodynamics, Graz University of Technology*, 2014.

[22] W. Hirschberg. TMsimple: A simple to use tyre model. Technical report, Institute of Automotive Engineering, Graz University of Technology, 2009.

[23] W. Hirschberg, F. Palcak, G. Rill, and J. Sotnik. Reliable Vehicle Dynamics Simulation in Spite of Uncertain Input Data. In *12th EAEC European Automotive Congress.* Slovak Society of Automotive Engineers (SAITS), 2009.

[24] W. Hirschberg and H. Waser. Fahrzeugdynamik. *Lecture Notes, Institute of Automotive Engineering, Graz University of Technology*, 2010.

[25] W. Hirschberg and H. Waser. Kraftfahrzeugtechnik. *Lecture Notes, Institute of Automotive Engineering, Graz University of Technology*, 2012.

[26] P. Hofmann. *Hybridfahrzeuge: Ein alternatives Antriebssystem für die Zukunft.* Springer, 2 edition, 2014. ISBN 978-3-7091-1780-4.

[27] M. Hofstetter. Kraftstoffeinsparpotential von Plug-In-Hybridfahrzeugen mit prädik-

tiver Betriebsstrategie. Master's thesis, Leopold-Franzens-University Innsbruck, 2014.

[28] A. Hülsmann. *Methodenentwicklung zur virtuellen Auslegung von Lastwechselphänomenen in Pkw*. PhD thesis, Faculty of Mechanical Engineering, University of Karlsruhe, 2007.

[29] P. Keil and A. Jossen. Aufbau und Parametrierung von Batteriemodellen. *19. DESIGN&ELEKTRONIK-Entwicklerforum Batterien & Ladekonzepte*, 2012.

[30] U. Kiencke and L. Nielsen. *Automotive Control Systems*. Springer, 2 edition, 2005. ISBN 978-3-540-26484-2.

[31] R. Korthauer. *Handbuch Lithium-Ionen-Batterie*. Springer, 2013. ISBN 978-3-642-30652-5.

[32] H. Kraus. *Development of an Operation Strategy for Plug-in Hybrid Electric Vehicles - Long-term Prediction and Adaptation based on Past Vehicle and Driver Data*. PhD thesis, Faculty of Mechanical Engineering, Graz University of Technology, 2016.

[33] F. Kücükay and J. Gebert. Schaltkomfort als neue Regelgröße bei Pkw-Automatikgetrieben. *1. Symposium: Steuerungssysteme für den Antriebsstrang von Kraftfahrzeugen*, 1997.

[34] J. Liebl, M. Lederer, K. Rohde-Brandenburger, J.-W. Biermann, M. Roth, and H. Schäfer. *Energiemanagement im Kraftfahrzeug: Optimierung von CO2-Emissionen und Verbrauch konventioneller und elektrifizierter Automobile*. Springer Vieweg, 2014. ISBN 978-3-658-04451-0.

[35] H. List and P. Schöggl. Objective Evaluation of Vehicle Driveability. *SAE International Congress and Exposition*, 1998.

[36] O. Martens. Regelung einer permanenterregten Synchronmaschine. *Institute of Control Science, Braunschweig University of Technology*, 2015.

[37] G. Mather. Measuring human sensory responses. *Total Vehicle Technology Conference*, 2002.

[38] F. Matthies. *Beitrag zur Modellbildung von Antriebssträngen für Fahrbarkeitsuntersuchungen*. PhD thesis, Faculty IV, Electrical Engineering and Computer Science, Berlin University of Technology, 2013.

[39] G. P. Merker and P. Eckert. *Handbuch Verbrennungsmotor*. Springer, 7 edition, ISBN 978-3-658-04678-1 2015.

[40] Y. L. Murphey, R. Milton, and L. Kiliaris. Driver's style classification using jerk analysis. *IEEE Workshop on Computational Intelligence in Vehicles and Vehicular Systems*, Nashville, TN, USA, 2009.

[41] N.N. AVL-DRIVE The objective tool for driveability assessment & development. Functional description, 2008.

[42] G. Paganelli, S. Delprat, T.M. Guerra, J. Rimaux, and J.J. Santin. Equivalent consumption minimization strategy for parallel hybrid powertrains. *55th IEEE Vehicular Technology Conference*, 2002.

[43] M. Papageorgiou, M. Leibold, and M. Buss. *Optimierung: Statische, dynamische, stochastische Verfahren für die Anwendung*. Springer, 2012. ISBN 978-3-662-46936-1.

[44] D. Peters, M. Reith, and M. Weller. Nachhaltige Mobilität mit Erdgas und Biomethan: Marktentwicklung 2014/2015. *Deutsche Energie Agentur*, 2015.

[45] V. Van Reeven, R. Huisman, M. Pesgens, and R. Koffrie. Energy management control concepts with preview for hybrid commercial vehicles. *6th International Conference on Continuously Variable and Hybrid Transmissions*, Maastricht, The Netherlands, 2010.

[46] K. Reif, K. E. Noreikat, and K. Borgeest. *Kraftfahrzeug Hybridantriebe: Grundlagen, Komponenten, Systeme, Anwendungen*. Springer Vieweg, 2012. ISBN 978-3-8348-2050-1.

[47] R. Reinhardt, A. Hoffmann, and T. Gerlach. *Nichtlineare Optimierung: Theorie, Numerik und Experimente*. Springer, 2013. ISBN 978-3-8274-2949-0.

[48] G. Rill. Vergleich von Integrationsverfahren an einem Beispiel aus der Fahrzeugdynamik. 2008.

[49] G. Rill. *Road Vehicle Dynamics: Fundamentals and Modeling*. CRC Press, 2012. ISBN 978-1-4398-3898-3.

[50] F. Schober. Parameter identification for a drivetrain-simulation. Master's thesis, Institute of Automotive Engineering, Graz University of Technology, 2016.

[51] P. Schöggl and E. Ramschak. Vehicle driveability assessment using neural networks for development, calibration and quality tests. *SAE 2000 World Congress*, Detroit, Michigan, 2000.

[52] C. Schröder. McKinsey: Marktanteil von Hybrid- und Elektrofahrzeugen liegt 2020 bei bis zu 33%. *URL: https://www.springerprofessional.de/automobil—motoren/hybridtechnik/mckinsey-marktanteil-von-hybrid-und-elektrofahrzeugen-liegt-2020/6564132*. last access: 16.8.2016.

[53] T. Schumacher. *Optimierung des Lastwechselverhaltens bei einem Pkw mit Frontantrieb*. PhD thesis, Faculty of Mechanical Engineering, RWTH Aachen University, 2002.

[54] O. Sundström. *Optimal control and design of hybrid-electric vehicles*. PhD thesis, ETH-Zürich, 2009.

[55] O. Sundström, D. Ambühl, and L. Guzzella. On implementation of dynamic programming for optimal control problems with final state constraints. *Oil & Gas Science and Technology*, Volume 65(1), 2009.

[56] O. Sundström and L. Guzzella. A generic dynamic programming matlab function. *18th IEEE International Conference on Control Applications*, Saint Petersburg, Russia, 2012.

[57] H. Takagi. Introduction to fuzzy systems, neural networks, and genetic algorithms. *Kyushu Institute of Design*, 1997.

[58] M. Ulbrich and S. Ulbrich. *Nichtlineare Optimierung*. Springer, 2012. ISBN 978-3-0346-0142-9.

[59] VDI. Human exposure to mechanical vibrations Whole-body vibration, 2002.

[60] X. Wei and G. Rizzoni. Objective Metrics of Fuel Economy, Performance and Driveability – A Review. *SAE Technical Paper Series*, 2004.

[61] A. Wilde, J. Schneider, and H-G. Herzog. Driving situation and driving style dependent charging strategy in hybrid electric vehicles. *ATZ worldwide*, Voulme 110(5), 2008.

[62] Gao Xiangyang, Zhang Jun, and Ning Ning. Transient behavior modeling and physical meaning analysis for Battery. *International Conference on Computer Application and Sytems Modelling (ICCASM)*, 2010.

[63] R. Zanasi, G. Sandoni, and R. Morselli. Simulation of variable dynamic dimension systems: The clutch example. *Proceeding of the European Control Conference*, 2001.

[64] C. Zhang and A. Vahidi. Real-time optimal control of plug-in hybrid vehicles with trip preview. *American Control Conference*, Baltimore, USA, 2010.